Politecnico di Milano

FACOLTÀ DI INGEGNERIA DEI SISTEMI
Corso di Laurea Magistrale in Ingegneria Fisica

Tesi di II Livello
Appello di Laurea del 20 Dicembre 2010

Single Monte Carlo Forward Solver for the Analysis of Diffuse Reflectance in Turbid Media

Candidato:
Michele Martinelli
Matricola 724527

Relatore:
Dr. Andrea Bassi

Correlatore:
Prof. Vasan Venugopalan

Anno Accademico 2009-2010

Abstract

This work is the result of nine months of research carried out at the University of California, Irvine, where I have worked for the Virtual Photonics Technology Initiative. This was established by the Laser Microbeam and Medical Program (LAMMP), an NCRR National Biomedical Technology Center at the Beckman Laser Institute and Medical Clinic in April 2008, to develop improved computational models to simulate and design optical diagnostic, imaging, and therapeutic modalities for research and educational purposes.

One of the richest fields of research in biomedical optics relies on the fact that light can be used for the diagnosis of illness or to study and monitor specific features of a biological tissue. When a light signal is shine on a biological tissue its characteristics are modified by the optical properties of the medium. Although biological tissues are extremely complex structures and microscopically very heterogeneous, for a large variety of applications homogenous models allow to evaluate within good accuracy their interaction with light.

During the last years a multitude of techniques and systems have been developed to collect the signal emitted by the probed tissue and to analyze it in order to extract the optical properties of a medium. This is generally done comparing experimental measurements to the results of a mathematical model that provides the trend of the output signal relying on the features of the input signal, on the optical properties of the probed tissue and on the characteristics of the measurement system. Once that the optical properties are determined they can be related to the tissue morphology, biochemical composition and physiological state.

In this context, my work focuses on the further development and characterization of the single Monte Carlo (sMC) method, which is a mathematical model that describes the relationship between the measured light signal and the optical properties of the tissue under investigation. The project I have carried out consists in the theoretical investigation, design and development of the single Monte Carlo model, based on advanced discretization techniques and on Non-Uniform-Rational-Bsplines (NURBS) interpolation. The sMC model was presented by Kienle and Patterson [1] who showed how a reference reflectance, $R_r(r, t)$, measured from a Monte Carlo simulation for a non-absorbing medium with a specific value of the scattering coefficient, could be used to derive $R(r, t)$ for any arbitrary value of the optical properties.

The potential of the sMC model relies in the fact that its analytical nature allows to overcome the computational burden associated to standard Monte Carlo simulations without the need of any approximations that are required for other approaches, such as the standard diffusion approximation.

To evaluate the reference signal from a MC simulation it is necessary to discretize the measurement domain, thus the reference is obtained only for a finite set of nominal values. As a result the sMC approach requires the interpolation of the reference values in order to evaluate $R(r, t)$ for an arbitrary value of the optical properties. Both the discretization and the interpolation processes lead to errors that affect the accuracy of the sMC model.

While sMC has been widely used by the biomedical community, a clear theoretical framework has never been presented to support the origin of the scaling relations. Once these are established one is in a better position to evaluate the effects of binning and interpolation on the subsequent errors. The objective of this work is to (i) establish a full analytical justification of the sMC method based on the Radiative Transport Equation; (ii) investigate the intrinsic limitations of the sMC method; (iii) evaluate the effect of binning and of interpolation on the accuracy of the derived results; (iv) investigate the accuracy of the implemented sMC model for a wide range of optical properties and (v) test its capability of solving inverse problem for the determination of optical properties of biological tissues.

This thesis is structured in three main chapters.

Chapter 1 contains a brief introduction to Photon Migration, i.e. the problem of light propagation in a highly diffusive medium. The main physical quantities of interest are introduced. Monte Carlo (MC) modeling of light transport in homogeneous media is explained and the MC code and graphical user interface that I have developed are presented. The aim of this short description is to make the reader familiar with the basic concepts of interest for radiative problems in biological tissue and to establish the nomenclature used later in this work.

Chapter 2 presents the single Monte Carlo model from an historical perspective and introduces the literature from which this work stems. Afterwards, the theoretical foundation for its validity is provided for the first time. According to the theoretical justification, the sMC method is validated through a statistical analysis that permits the investigation of its intrinsic limitations with respect to traditional Monte Carlo simulations. The chapter ends with an accurate description of the procedures and the algorithms that have been used for the actual implementation of the forward solver. To improve the accuracy of the sMC model the limits induced by the discretization are reduced through the development of a novel adaptive binning technique that allows to obtain an accurate reference signal over a wide physical domain.

Chapter 3 shows the systematic study performed on the implemented model. First of all we analyze the performance of the implemented sMC model as a forward solver. We provide a definition of a gold standard and we establish an error metric used to assert the accuracy of the model output for the evaluation of the time-resolved reflectance and of the steady state reflectance for semi-infinite homogeneous media. Afterwards we focus on the use of the sMC solver for the recovery of optical properties from simulated data. For the temporally-resolved case we use the sMC model to recover optical properties for multiple source-detector separations that fall within the non-diffusive and the diffusive regime. For each case under investigation we analyze the effects that the temporal resolution and the fitting range have on the inversion results and we test the performance of the sMC model in the presence of additional noise. For the steady state domain we investigate the possibility of using the sMC model for the recovery of optical properties changing the number of detectors used to obtain the reflectance signal and we test the performance of the model in presence of additional noise.

The software implemented for this work is coded in C# and has been integrated into the Virtual Tissue Simulator (VTS), an open source software platform for the analysis of relevant forward and inverse radiative transport problems in Biomedical Optics. A detailed description of the VTS is reported in appendix A.

A relevant part of this work is the implementation of a general-purpose Matlab toolbox for approximating and interpolating large data sets using non-uniform rational B-splines (NURBS). A detailed description of the NURBS toolbox is reported in appendix B.

The focus given to biomedical applications in this thesis should not shadow the importance of Photon Migration in many other research fields. Atmospheric Optics, Underwater Optics, and Astrophysical Optics share the same basic idea of transfer of radiation in a turbid, diffusive or generally random medium. Furthermore, the assessment of Food Quality and Remote Sensing can find valuable interpreting tools within the Photon Migration framework.

Sommario

Questo lavoro di tesi è il risultato di nove mesi di ricerca condotti presso la University of California, Irvine, dove ho lavorato per la Virtual Photonics Technology Initiative. Questa è stata fondata presso il Beckman Laser Institute con lo scopo di sviluppare modelli computazionali per lo studio e il design di tecniche per la diagnosi ottica o per lo sviluppo di applicazioni terapeutiche della luce.

Uno dei campi di ricerca più sviluppati nel contesto dell'ottica biomedica riguarda l'utilizzo di segnali luminosi per diagnosi di patologie e per il monitoraggio dello stato fisiologico di tessuti biologici. Quando un tessuto biologico viene illuminato da un segnale ottico, le caratteristiche del segnale vengono modificate in base alle proprietà ottiche del mezzo che possono essere misurate analizzando questa variazione. Anche se i tessuti biologici sono strutture estremamente complesse e altamente eterogenee, per molte applicazioni è possibile utilizzare modelli omogenei per studiare l'interazione con segnali luminosi caratterizzati da una lunghezza d'onde nel vicino infrarosso.

Negli ultimi anni sono state sviluppate innumerevoli tecniche e sistemi che permettono di misurare e analizzare segnali ottici riflessi da tessuti biologici. Tali sistemi consentono la misura delle proprietà ottiche che vengono determinate comparando misure sperimentali con i risultati provvisti da un modello matematico che calcola il segnale di riflettanza sulla base del segnale di sonda, delle proprietà ottiche del mezzo analizzato e del sistema di misura. Una volta quantificate le proprietà ottiche è possibile risalire allo stato morfologico, alla composizione chimica e allo stato fisiologico del tessuto.

In questo contesto, il mio lavoro è focalizzato sullo sviluppo e sulla caratterizzazione del metodo 'single Monte Carlo' (sMC). Questo è un modello matematico che descrive la relazione tra il segnale luminoso riflesso da un mezzo torbido e le sue proprietà ottiche. Il progetto di cui mi sono occupato consiste nell'indagine teorica, nel design e nello sviluppo del modello sMC, basato sull'utilizzo di avanzate tecniche di analisi e discretizzazione di dati stocastici e su interpolazione tramite Non-Uniform-Rational-Bsplines (NURBS). Il metodo sMC, presentato da A. Kienle e M.S. Patterson nel 1996, si basa sulla rielaborazione del segnale di riflettanza ottenuto tramite una singola simulazione Monte Carlo, in un mezzo non-assorbente con uno specifico valore del coefficiente di scattering, per ottenere la riflettanza per un valore arbitrario delle proprietà ottiche.

Il potenziale del metodo sMC si basa sul fatto che la sua natura analitica permette di evitare il carico computazionale associato a tradizionali simulazioni Monte Carlo, senza la necessità di alcuna approssimazione che ne limiti l'applicabilità.

Per calcolare il segnale di referenza tramite una simulazione MC è necessario discretizzare il dominio fisico dove il segnale viene misurato solo per un set finito di valori nominali. Di conseguenza il metodo sMC richiede l'interpolazione di questi valori discreti per effettuare il calcolo del segnale di riflettanza per un valore arbitrario delle proprietà ottiche. Entrambi i processi di discretizzazione e di interpolazione sono causa di errori che condizionano la precisione dei risultati ottenuti tramite il modello single Monte Carlo.

Il metodo sMC è stato largamente utilizzato dalla comunità biomedica, tuttavia una giustificazione teorica della sua validità non è mai stata pubblicata. La necessità di fornire una dimostrazione rigorosa di questo metodo risiede nel fatto che essa permette la comprensione dei suoi limiti intrinsechi e permette un'analisi accurata degli errori di discretizzazione e di interpolazione. L'obbiettivo di questo lavoro consiste (i) nel fornire una giustificazione teorica esaustiva del metodo sMC basata sulla Equazione del Trasporto Radiativo, (ii) nel presentare uno studio delle sue limitazioni intrinseche sulla base di un indagine statistica, (iii) nel valutare l'effetto che diverse tecniche di discretizzazione e di interpolazione hanno sulla precisione dei risultati forniti dal modello, (iv) nell'analizzare in maniera dettagliata l'accuratezza del modello sMC implementato per il calcolo di segnali di riflettanza per un ampio range di proprietà ottiche e (v) nel valutare le potenzialità del modello implementato per la misura di proprietà ottiche di tessuti biologici tramite l'analisi di misure di riflettanza risolte in spazio e in tempo.

Questa tesi è suddivisa in tre capitoli.

Il **Capitolo1** contiene una breve introduzione relativa alla Photon Migration, cioè la descrizione della propagazione della luce in mezzi torbidi. Le principali grandezze fisiche considerate per la ricerca svolta sono introdotte e definite. Nella seconda parte di questo capitolo viene descritta la modellizzazione Monte Carlo (MC) per la simulazione del trasporto di fotoni in tessuti biologici. Gli aspetti salienti necessari per la comprensione del metodo Monte Carlo vengono presentati brevemente. Il capitolo termina con una descrizione del codice MC e dell'interfaccia grafica che ho implementato per la fase iniziale di questo lavoro, con lo scopo di comprendere la struttura e la logica di questo metodo stocastico.

Nel **Capitolo 2** la tecnica single Monte Carlo viene introdotta con una prospettiva storica, illustrando la letteratura da cui questo lavoro prende spunto. La giustificazione teorica di questo metodo viene presentata per la prima volta e il metodo viene convalidato sulla base di un indagine statistica che permette l'analisi delle limitazione intrinseche del modello sMC rispetto a tradizionali simulazioni Monte Carlo. In questo capitolo gli algoritmi e le tecniche utilizzate per l'implementazione del modello sMC sono descritte dettagliatamente. Per migliorare l'accuratezza del risolutore implementato per questo lavoro, è stata sviluppata una tecnica di 'discretizzazione adattativa' che permette di ottenere il segnale di referenza con alta precisione su un vasto dominio fisico.

Nel **Capitolo 3** viene mostrata l'analisi sistematica del modello implementato. In primo luogo viene analizzata la precisione del metodo per la valutazione di segnali di riflettanza risolta in spazio e/o in tempo. Dopo aver definito il 'gold standard' per i differenti domini, l'output del modello sMC viene confrontato in termini di errore relativo e assoluto. In seguito viene analizzata la possibilità di utilizzare il metodo sMC per la misura di proprietà ottiche tramite l'analisi di misure di riflettanza nei differenti domini di misura. Per misure di riflettanza risolte in tempo il modello sMC viene utilizzato per la misura di proprietà ottiche sia per il regime non-diffusivo che per il regime diffusivo. Per ogni caso studiato viene analizzata l'influenza che diverse risoluzioni temporali e diversi 'fitting range'

hanno sui risultati ottenuti. Per misure di riflettanza risolte in spazio viene studiata la possibilità di misurare i coefficienti di scattering e di assorbimento variando il numero di rilevatori utilizzati per la determinazione del segnale.

Il modello sMC descritto in questo lavoro è stato implementato in C# ed è stato integrato nel Virtual Tissue Simulator (VTS), una piattaforma software open source per l'analisi di problemi relativi all'ambito del trasporto di fotoni nell'ambito dell'ottica biomedica. Una descrizione dettagliata del VTS è riportata nell'appendice A.

Una parte rilevante di questo lavoro di tesi consiste nell'implementazione di un Matlab toolbox per l'approssimazione e l'interpolazione di dati discreti utilizzando non-uniform rational B-splines (NURBS). Una descrizione dettagliata di questo toolbox è riportata nell'appendice B.

Tecniche basate sulla Photon Migration sono state sviluppate in molti altri campi di ricerca, quali l'ottica atmosferica, l'ottica subacquea e l'ottica astrofisica. La focalizzazione di questo lavoro di ricerca sull'ambito dell'ottica biomedica non intende sminuire l'importanza di altre applicazioni riguardanti la propagazione di segnali luminosi in mezzi torbidi.

x

Contents

Chapter 1

Photon Migration in Diffusive Media

1.1 Introduction: the Biomedical Optics framework

Indian medical literature dating to 1500 BC describes a treatment combining herbs with natural sunlight to treat non-pigmented skin areas. Buddhist literature from about 200 AD and 10th century Chinese documents made similar references. Since then a large array of treatments and techniques have been developed from the use of controlled light for both therapeutic and diagnostic medical applications.
The main types of interaction between light and biological tissues used for therapeutical applications may be gathered as:

- photochemical effects
- photothermal effects
- photoablation effects
- photodistruption effects

The detailed knowledge of these phenomenons led to the development of many light therapy techniques such as the Photodynamic therapy (PDT) for treatment of cancer and macular degeneration, psoralen + UVA treatment (PUVA) for the treatment of psoriasis or the application of low level laser, red light, near-infra-red and ultraviolet light for pain management, hair removal, skin treatments, accelerated wound healing and many other applications.

In the last decades, the field of Biomedical Optics has flourished on the diagnostic side as well. The continuous demand for noninvasive imaging and spectroscopic techniques, coupled with an increasing attention to healthcare costs, has in fact fostered the rapid development of light-based technologies for medical diagnostics.
Medical imaging is the technique and process used to create images of the human body (or parts and function thereof) for clinical purposes (medical procedures seeking to reveal, diagnose or examine

disease) or medical science (including the study of normal anatomy and physiology). Spectroscopy was originally defined as the study of the interaction between radiation and matter as a function of wavelength. Nowaday it has developed into multiple applications, often coupled with imaging approaches, used to non-invasively monitor either time-, space-, temporal frequency-, or spatial frequency-dependent variations of the physiological state of biological tissues using visible or near infrared light.
Optical imaging and spectroscopy offer, at least in principle, the potentiality to non-invasively probe tissue structures, reconstruct tissue optical properties (absorption and scattering), and relate them to functional and physiological parameters (blood volume, water content, tissue oxygenation) and the eventual pathological state (presence of malignancies). Such measurement and recording techniques are not primarily designed to produce images, but produce data susceptible to be represented as maps (i.e. containing positional information), and can be seen as forms of medical imaging.

What is essential for a good efficacy of light based diagnostic techniques and therapeutic protocols, is a complete optical characterization of tissues. The key points for such diagnostic techniques are the sensitivity to optical contrasts in tissue, the discrimination between scattering and absorbing contributions and the spatial resolution. Normal and diseased tissue may differ in fact both in the scattering coefficient (calcification, fibrous or fatty tissue) and in the absorption coefficient (vascularization, exogenous contrast agents). Moreover, a correct light dosimetry has been denoted as a primary factor for the positive outcome of photodynamic therapy of tumors, and for other therapeutic applications such as laser surgery, and ablation.

Biological tissue falls within the category of turbid or diffusive media. In a diffusive medium in the visible and near infrared (NIR) spectral region (600-1300 nm) light scattering is naturally stronger than light absorption, even if the latter can be non negligible. This implies that light can be scattered many times before being either absorbed or remitted from the medium. This phenomenon, called multiple scattering of light, introduces an uncertainty in the pathlength travelled by photons in the medium, therefore light propagation in turbid medium is commonly addressed with the term Photon Migration.

Considering a particular application the accuracy in the determination of tissue optical properties by spectroscopy measurements depends both on the performance of the experimental system set-up and on the interpretation of experimental data with a proper theoretical model. The theoretical model used to analyze measurements and experimental results plays a crucial role for the understanding of light propagation and for the determination of the physiological status of biological tissues since it is a mathematical representation of some photometric quantities that are affected by the optical properties of the tissue.

1.2 Physics of Photon Migration

The phenomenon of light propagation in turbid medium is addressed with the term Photon Migration. The term turbid or diffusive medium refers to many substances which naturally possess the characteristic of being opaque to visible light (paints, powders, clouds, foams, biological tissues). Light absorption and light scattering are the natural phenomena responsible for opacity. Absorption depends on the presence of endogenous or exogenous chromophores within the medium, while

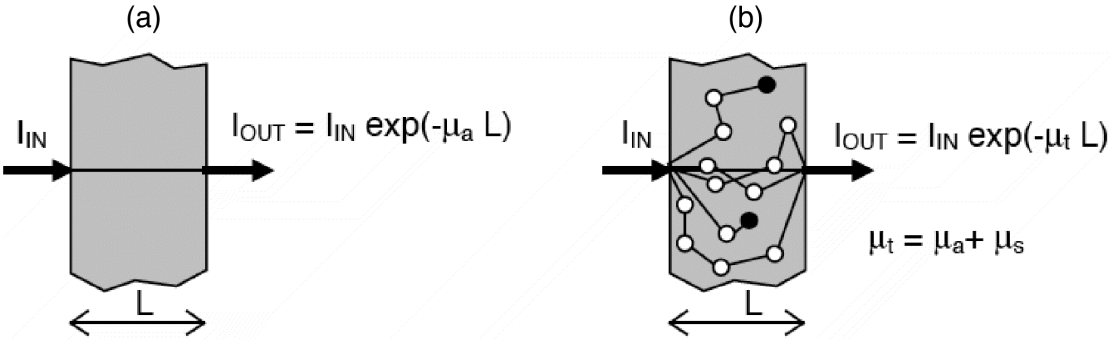

Figure 1.1: Photon propagation in a clear (a) and in a turbid (b) medium.

(elastic) scattering depends on microscopic discontinuities in the dielectric properties of the medium. By using a simplified description we can consider the medium as made of scattering centers and absorbing centers, and the light pulse as a stream of particles, called photons, moving ballistically within the medium. Whenever a photon strikes a scattering center it changes its trajectory and keeps on propagating in the medium, until it is eventually remitted across the boundary, or it is definitely captured by an absorbing center.

The characteristic parameters of light propagation within the diffusive medium are the scattering length, l_s, and the absorption length, l_a, representing the photon mean free path between successive scattering events and absorption events, respectively. Equivalently, and more frequently, the scattering coefficient $\mu_s = 1/l_s$ and the absorption coefficient $\mu_a = 1/l_a$ can be introduced to indicate the scattering probability per unit length and the absorption probability per unit length, respectively. Hence, when considering conventional absorption spectroscopy measurements in a collimated geometry (1.2), the transmitted intensity through a clear medium can be related by the Lambert Law to the absorption coefficient since the distance travelled by light in the medium equals the source-detector distance L. Conversely, in a turbid medium, an intensity measurement yields the attenuation coefficient, $\mu_t = \mu_a + \mu_s$, representing the photon loss due to absorption and to photons scattered into different directions than the one of observation. The attenuation coefficient is equivalently referred to as interaction coefficient.

Light propagation in diffusive media has been usually interpreted within the framework of the Radiative Transfer Theory, rather than within the more rigorous set of Electromagnetic Theory. In the multiple scattering regime, Electromagnetic Theory approach is in fact characterized by complexity of the formalism and by the lack of workable tools. In contrast with modeling light as the propagation of electromagnetic fields, the Radiative Transfer Theory considers the transport of energy in terms of propagation of single particles within the medium.
The development of Radiative Transport Theory is heuristic and lacks the rigor of Electromagnetic Theory, however the formulation is flexible and capable of treating many physical phenomena. It has been successfully employed for the problems of atmospheric and underwater visibility, and more recently it has been applied to biomedical optics.

The basic assumption in Radiative Transport Theory is that it is possible to ignore the wave nature of light and simply consider the flow of energy associated with the propagation of photons within the medium. Therefor by performing a balance for the radiance $L(r, \hat{\Omega}, t)$ which represents the rate

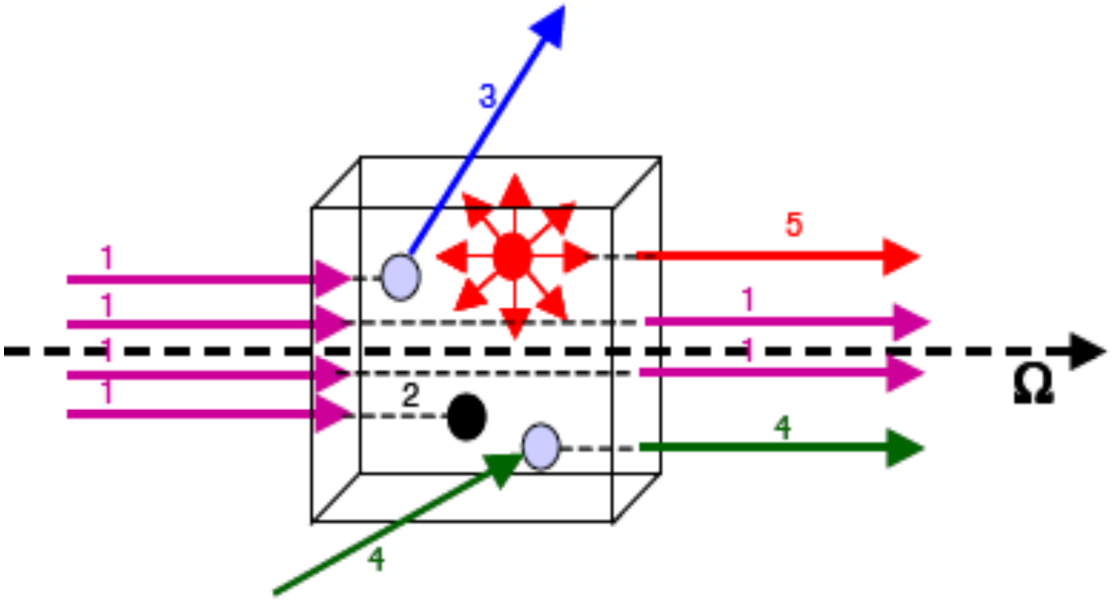

Figure 1.2: Schematic representation of the balance terms that lead to the RTE: 1) flux of photons along the direction $\hat{\Omega}$, 2) absorption losses, 3) scattering losses, 4) contribution from different directions, 5) source emission.

at which energy arrives at a fixed location r at a given time t in a given direction $\hat{\Omega}$ it is possible to obtain the equation that describes the propagation of light within the medium. This Equation is denoted as the Radiative Transport Equation (RTE)

$$\frac{1}{v}\frac{\partial L(r,\hat{\Omega},t)}{\partial t} = -\nabla L(r,\hat{\Omega},t)\cdot\hat{\Omega} - \mu_s L(r,\hat{\Omega},t) + \mu_s \int_{4\pi} p(\hat{\Omega}'\rightarrow\hat{\Omega}) L(r,\hat{\Omega}',t)\ \mathrm{d}\Omega' + Q(r,\hat{\Omega},t) \tag{1.1}$$

which is characterized by the optical properties of the propagating medium. The phase function, $p(\hat{\Omega}'\rightarrow\hat{\Omega})$, expresses the probability function for scattering from direction $\hat{\Omega}'$ to $\hat{\Omega}$, which is assumed to depend only on the angle Θ between $\hat{\Omega}'$ and $\hat{\Omega}$, so $p(\hat{\Omega}'\rightarrow\hat{\Omega}) = p(\cos\Theta)$. The mean cosine of the scattering angle Θ is often called single-scattering anisotropy, g. The source term $Q(r,\hat{\Omega},t)$ represents the power emitted through a unit solid angle centered on $\hat{\Omega}$ into a unit volume at r at time t. Equation (1.1) treats photons as billiard balls undergoing elastic collisions and traveling through the medium at speed $v = c/n$, where n is the refractive index of the medium.

Figure 1.2 shows a schematic representation of the balance terms that are used to build up the RTE: the temporal variation of the radiance is equal to the flux of photons exiting the volume element, reduced by the absorption and the scattering losses, increased by the energy carried by photon scattered from any other direction, $\hat{\Omega}'$, to the direction $\hat{\Omega}$ plus the contribution given by the source term.

Although the RTE is intuitive to understand it is difficult to solve analytically and much effort has been devoted to develop approximate analytical expressions that provide accurate descriptions of

light transport inside tissues [2, 3]. For most biological tissues in the red and NIR, optical scattering is dominant over optical absorption and the radiance can be approximated by the sum of an isotropic fluence and a small directional flux. This diffusion approximation to the RTE can be solved in a closed solution form for an infinite homogeneous turbid media.

However, the range of applicability of the diffusion approximation has to be carefully examined because its accuracy can break down in cases where the absorption coefficient is large relative to the reduced scattering, $\mu_s' = (1-g)\mu_s$ [4], in the presence of physical boundaries, or when the source - detector separation is not much larger then transport mean free path, $l^* = (\mu_a + \mu_s')^{-1}$ [5].

To overcome these limitations, Monte Carlo (MC) simulations have been introduced in the field of biomedical optics [6]. Monte Carlo simulations represent a stochastic method to provide exact solutions to the RTE within the known variance of the simulation output. Standard MC models trace a large ($10^5 - 10^{10}$) number of photon trajectories from the source to one or several detectors to estimate the distribution of light inside and/or on the boundaries of a tissue. Unlike analytic approaches, MC simulations are versatile in that they can easily incorporate heterogeneous media, anisotropic sources and detectors, and irregularly shaped boundaries. Due to its potential to offer exact solutions of the RTE, the Monte Carlo method has become a de-facto gold standard for modeling photon migration in tissue optics.

1.3 Spectroscopy Measurements

When light is used for the diagnosis of illness or to study and monitor other features of a biological tissue the treatment should not be invasive and it should be as simple as possible. For this reason the measurement is not performed inside the tissue, while the photons are collected at a boundary of the propagating media.

When a light signal is shine on a biological tissue its characteristics are modified by the optical properties of the medium. Although biological tissues are extremely complex structures and microscopically very heterogeneous, for a large variety of applications homogenous models allow to evaluate within good accuracy their interaction with light. Although the strong approximation, this approach has been successfully used to study the physiological state of biological tissues where the goal is to study the 'bulk properties' of the medium rather then its microstructure.

During the last years a multitude of techniques and systems have been developed to collect the signal emitted by the probed tissue and to analyze it in order to extract the optical properties (typically μ_a and μ_s') of a medium. This is generally done comparing experimental measurements to the results of a mathematical model that provides the trend of the output signal relying on the features of the input signal, on the optical properties of the probed tissue and on the characteristics of the measurement system.

Figure 1.3 illustrates a schematic representation of possible approaches used to perform spectroscopy measurements using a light probe. Regardless of the features of the probing approach, it is possible to define two types of measurements. When the remitted photons are collected on the same surface of the injected light the measurement is referred to as **reflectance**, while when the measuring system is placed on the opposite of the medium the measurement is referred to as **transmittance**.

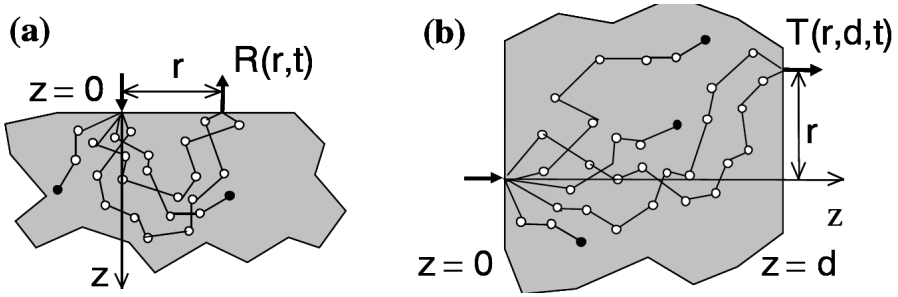

Figure 1.3: Schematic representation of a reflectance measurement in a semi-infinite medium (a) and of a transmittance measurement for a semi-infinite slab.

The modeling of a reflectance geometry is usually developed considering only the top surface and representing the medium as a semi-infinite space. This approximation is possible when the distance of the other boundaries is large enough to neglect their influence on the propagation of the larger part of the emitted photons. The same idea is applied when one deals with transmittance geometries, where only the probing and collecting surfaces are considered. For many applications these approximations allow to simplify the mathematical models without affecting the accuracy of the results.

For this work the focus is on reflectance measurements. Many applications used for diagnostical measurements on the human body are performed using this geometry because the thickness of the human body often becomes to large to allow feasible transmittance measurements. The simplest and most immediate reflectance measurement consists in shining a light source, such as a laser light, onto the tissue and by comparing the re-emitted light intensity with the injected intensity it is possible to evaluate the attenuation coefficient. When considering conventional continuous-wave (CW) absorption spectroscopy measurements in a diffusive medium, the spread of photon paths in the medium may confound the results by the impossibility to discriminate absorption and scattering contributions. Equivalently, CW imaging through a scattering medium suffers decreased contrast and spatial resolution, because of the blurring introduced by the spread of photon paths in the medium.

To overcome this limitation, different spectroscopy approaches have been investigated. The values of μ_a and μ_s can be derived analyzing the spatial or the temporal distribution of the photons reflected at the top surface. Photon Migration in the temporal frequency-domain is the natural alternative to the time-domain approach. More recently, even the spatial-frequency domain approach has been successfully used. Each of these different techniques has specific characteristic and features in terms of complexity of the experimental set-up, theoretical model, spatial resolution, cost, speed and so on. In the following sections a brief description of these approach is given, without asserting with regard to which one is the best solution because the choice is strongly problem-dependent.

1.3.1 Spatially-Resolved Reflectance

The spatially-resolved reflectance (SRR) is a measurement of the spatial distribution of the photons reflected by the tissue as a function of the distance from the injection point. Figure 1.4 shows its schematic representation. For a homogeneous media it is possible to exploit the cylindrical

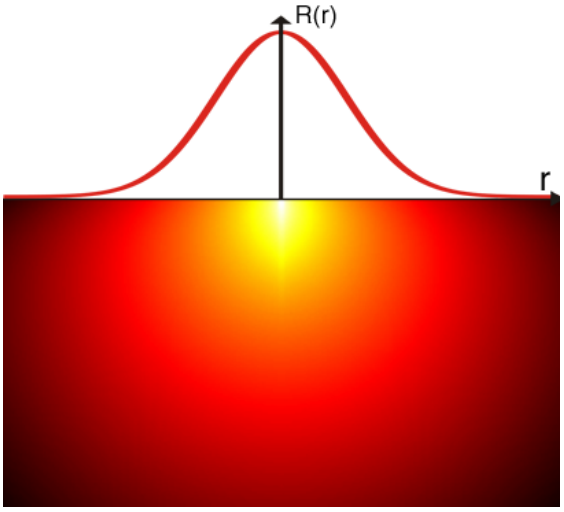

Figure 1.4: Schematic representation of the spatially-resolved reflectance.

symmetry and to represent the intensity of the collected signal as a function of the radial coordinate, r, only. Thus the spatially-resolved reflectance is indicated as $R(r)$ and for this work it is expressed in [mm^{-2}].

In principle it is possible to discriminate the values of μ_s and μ_a from the trend of the curve R(r). Increasing the absorption coefficient results in a reduction of the signal over the entire radial range (more accentuated for larger distances). When the scattering coefficient becomes larger $R(r)$ increases for shorter distances and it decreases for larger values of r. This is due to the fact that if the scattering mean free path becomes smaller the signal in 'focused' over a smaller region and the probability of a photon to be emitted nearby the source becomes larger.

When photons are injected into the tissue using a fiber optic probe. It is possible to measure the spatially-resolved reflectance using camera-based systems ([7]) or fiber-based systems [8, 9].

1.3.2 Spatially- and Temporally-Resolved Reflectance

Since photon pathlength is directly related to the time-of-flight in the medium, the natural alternative to the simplest spatially-resolved approach is to perform spatially- and temporally- resolved measurements. The time-resolved techniques offer, in principle, the possibility to improve the discrimination of light absorption and light scattering contributions in a diffusive medium.

Typically, an ultrashort light pulse is injected into the medium using an optical fiber, and the emitted photons are collected using another optical fiber placed on the surface of the medium at a distance r from the injection point, as shown in Fig. 1.5. The temporal distribution of the photon remittance probability is obtained measuring the time lapse between the injection moment and the collection moment. This is typically done using a time-correlated-single-photon-counting system (TCSPC) that is based on the conversion of the optical signal to an electrical signal with amplitude proportional to the time of flight of the photon within the tissue [10].

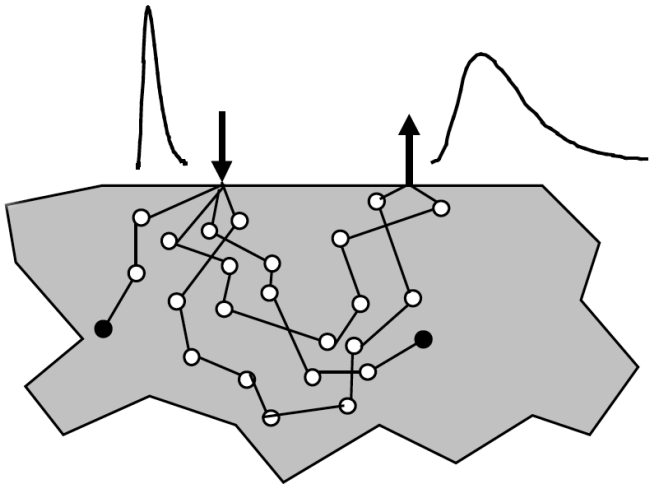

Figure 1.5: Schematic representation of the temporally-resolved reflectance.

Quantitative and accurate determination of turbid media optical coefficients has been achieved even measuring the time and space resolved measurements of diffuse backscattered light using streak camera systems [11]. A crucial aspect for time domain system is the necessity of distinguishing the broadening of the pulse due to the propagation inside the tissue from the contribution given by the measurement system.

The detected curve, denoted as $R(r, t)$, contains the information on the scattering contribution (the spread of photons determines the broadening of the injected pulse) and on the absorption contribution (absorption reduces the probability of detecting a photon moving within the medium and attenuates the injected pulse). Following the injection of the light pulse within a turbid medium, the temporal distribution of the remitted photons at a distance r from the injection point will be delayed, broadened, and attenuated.

To a first approximation, the delay is a consequence of the finite time light takes to travel the distance between source and detector. Broadening is mainly due to the many different paths that photons undergo because of multiple scattering. Finally, attenuation appears since absorption reduces the probability of detecting a photon, and diffusion into other directions within the medium decreases the number of detected photons in the considered direction.

Figure 1.6 depicts the effects of changes in source-detector distance (Fig. 1.6 a, b), scattering (Fig. 1.6 c, d) and absorption (Fig. 1.6 e, f) on time-resolved reflectance curves. Increasing the source-detector distance yields an increasing delay in the temporal distribution of detected photons and a decrease of their number. A similar behavior is observed when the scattering increases. Finally, absorption affects both the signal intensity and the slope of the tail of the curves, while leaving the temporal position of the curves substantially unchanged.

Whenever the geometrical parameters are known, a rough estimate of the scattering and absorbing characteristics of the medium can thus be obtained from the evaluation of the peak position and of the slope of the tail, respectively. More quantitative and accurate estimates can be obtained by interpreting the curves with a proper theoretical model. As shown here above, time-resolved

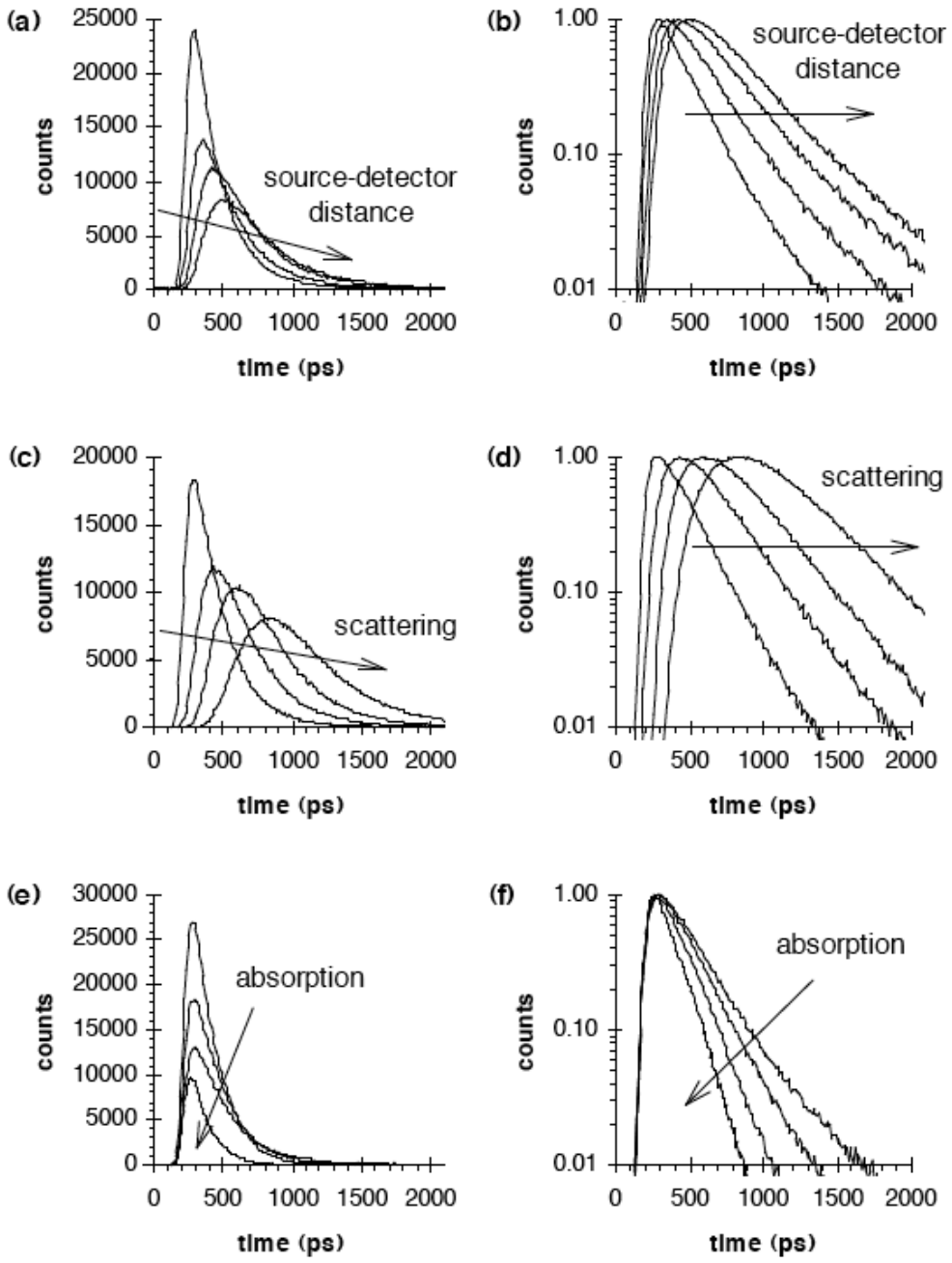

Figure 1.6: Effects of changes due to an increase in source-detector distance (a, b), scattering (c, d) and absorption (e, f) on absolute (a, c, e) and on normalized (b, d, f) temporally-resolved reflectance curves.

measurements enable the noninvasive optical characterization of diffusive media by assessing the absorbing and the scattering contributions.

1.4 Monte Carlo Modeling of Light Transport

1.4.1 Introduction

Monte Carlo (MC) simulation has been used to solve a variety of physical problems. In all applications of the MC method, a stochastic model is constructed in which the expected value of a certain random variable (or of a combination of several variables) is equivalent to the value of a physical quantity to be determined. This expected value is then estimated by the average of multiple independent samples representing the random variable introduced above, For the construction of the series of independent samples, random numbers following the distribution of the variable to be estimated are used.

Monte Carlo simulations of photon propagation offer a flexible yet rigorous approach toward photon transport in turbid tissues. The method describes local rules of photon propagation that are expressed, in the simplest case, as probability distributions that describe the step size of the photon movement between sides of interaction and the angles of of deflection in a photon's trajectory when a scattering event occurs. the simulation can score multiple physical quantities simultaneously.

However, the method is statistical in nature and and relies on calculating the propagation of a large number of photons by the computer. As a result, this method requires a large amount of computation time. The computing effort depends on the number of photons that needs to be traced which depends largely on the question being asked, on the precision needed and on the spatial resolution desired.

The simulations described in this section do not treat the photon as a wave phenomenon and ignore such features as phase and polarization. This idea matches the principle of the Radiative Transport Theory that represents light with its particle nature. Because they offer a way to evaluate photometric quantities relative to light transport in any medium, Monte Carlo (MC) simulations have been introduced in the field of biomedical optics [6]. Monte Carlo simulations rely on a stochastic model to provide exact solutions to the RTE consistent with the variance of the simulation output.

Standard MC models trace a large ($N = 10^5 - 10^{10}$) number of photon trajectories from the source to one or more detectors to estimate the distribution of light inside and/or on the boundaries of a tissue. Unlike analytic approaches, MC simulations are versatile in that they can easily incorporate heterogeneous media, anisotropic sources and detectors, and irregularly shaped boundaries. Due to its potential to offer exact solutions of the RTE, the Monte Carlo method has become a de-facto gold standard for modeling photon migration in tissue optics.

To achieve a better understanding of MC simulations my first approach towards this field was the development of a simple version of the MC code. Getting inspiration from the Monte-Carlo-Multi-Layered (MCML) code developed by Jacques and Wang [12] in standard C I have implemented a C# version modified for temporal applications. I have implemented a basic GUI to work with

this software which can be used to evaluate the spatially- and temporally-resolved reflectance and transmittance for homogeneous media. The code has been validated comparing its output with the output of the original MCML implementation.

1.4.2 The Problem

The MC simulations used for this work deal with the transport of an infinitely narrow photon beam perpendicularly incident on a homogeneous semi-infinite medium. Photons traveling through the medium move along straight lines and undergo scattering events, which modify their direction of propagation, they suffer absorption and they collide on the top surface of the tissue, where they can be internally reflected or escape.

The propagating medium is described by the following parameters: the thickness, the refractive index, the absorption coefficient, the scattering coefficient and the anisotropy factor. Although the real tissue can never be infinitely wide and deep, it can be so treated if it is much larger and deeper than the spatial extension of the photon distribution.

The physical quantities that can be simulated are photon absorption, fluence, reflectance and transmittance. These photometric quantities can be measured as a function of space, time and/or angle. The simulation propagates photons in three dimensions and a cartesian coordinate system is used to trace photons. The origin of the coordinate system is the photon incident point an the tissue surface, the z-axis is always the normal of the surface pointing toward the inside of the tissue, and the xy-plane is therefore on the tissue surface. The temporal dimension is obtained relating the photon paths to the time of flight through the speed of light within a medium with refractive index n.

Dealing with homogeneous tissues it is possible to consider cylindrically symmetric tissue model, thus the r coordinate of the cylindrical coordinate system is also used. A moving spherical coordinate system, whose z-axis is aligned with the photon propagation direction dynamically , is used for sampling of the propagation direction change of a photon. In this system, the deflection angle, Θ, and the azimuthal angle, Ψ, due to scattering are first sampled. Then, the photon direction is updated in terms of the directional cosines in the Cartesian coordinate system.

1.4.3 Sampling Random Variables

The Monte Carlo method, as its name implies ("throwing a dice"), relies on the sampling of variables from well defined probability distributions. Several books (Cashew et al., 1959, Kalos et al., 1986, Lux et al., 1991) provide good references for the mathematical and practical principles of MC modeling. Here the method for sampling random variables in a Monte Carlo simulation is briefly reviewed.

Consider a random variable, χ, which is needed by the MC simulation of photon propagation in tissue. This variable may be the step size a photon will take between photon-tissue interaction sites or the angle of deflection a scattered photon may experience due to a scattering event. There is a

normalized probability density function that defined the distribution of χ over the general interval (a, b) of the values it can assume.

To simulate propagation a value for χ is repeatedly chosen based on a pseudo-random number generator. The computer provides a random variable, ξ, which is uniformly distributed in the interval (0,1). To sample a generally non-uniform distributed function, $p(\chi)$, it is assumed that there exists a nondecreasing function $\chi = f(\xi)$ which maps $\xi \in (0, 1)$ to $\chi \in (a, b)$. The two variables then have a one to one mapping that allows to use the random generator of the computer combined with an algorithm to generate a sequence of numbers that approximates the properties of the distribution of the variable needed by the simulation.

Random number generation is a very complex and subtle field of study. As John von Neumann joked, "Anyone who considers arithmetical methods of producing random digits is, of course, in a state of sin." The sequence is not truly random in that it is completely determined by a relatively small set of initial values, often called the seed of the generator. During the last decades the randomness of the generators has been improved and multiple instances of pseudorandom algorithms have been presented. For this work the Mersenne Twister [13] algorithm have been adopted.

1.4.4 Rules for Photon Propagation

Figure 1.7 indicates the basic flowchart for the photon tracing part of a Monte Carlo simulation for homogeneous tissue. Basically each photon is injected into simulating medium and it is propagated according to the results of a set of action and decision functions. A simple variance reduction technique, implicit photon capture, is used to improve the efficiency of the MC simulation. This technique allows one to equivalently propagate many photons as a packet along a particular pathway simultaneously instead of tracing one photon at a time. Each photon packet is initially assigned a weight, w, equal to unity and, during the propagation, this value is reduced in order to account for the optical absorption of the medium. Later on the photon packet will be simply referred to as photon, but one should bear in mind that the concept of the photon weight is associated with the packet and not with a single photon that can be partially absorbed.

Launching a Photon Packet

Each photon packet is orthogonally injected into the tissue at the origin, which corresponds to an infinitely narrow collimated beam of photons. The current position of the photon is specified by the Cartesian coordinates (x,y,z). The current photon direction is specified by a unit vector, $\mathbf{r}$, which can be described by the directional cosines (μ_x, μ_y, μ_z):

$$\mu_x = \mathbf{r} \cdot \mathbf{x} \tag{1.2}$$

$$\mu_y = \mathbf{r} \cdot \mathbf{y} \tag{1.3}$$

$$\mu_z = \mathbf{r} \cdot \mathbf{z} \tag{1.4}$$

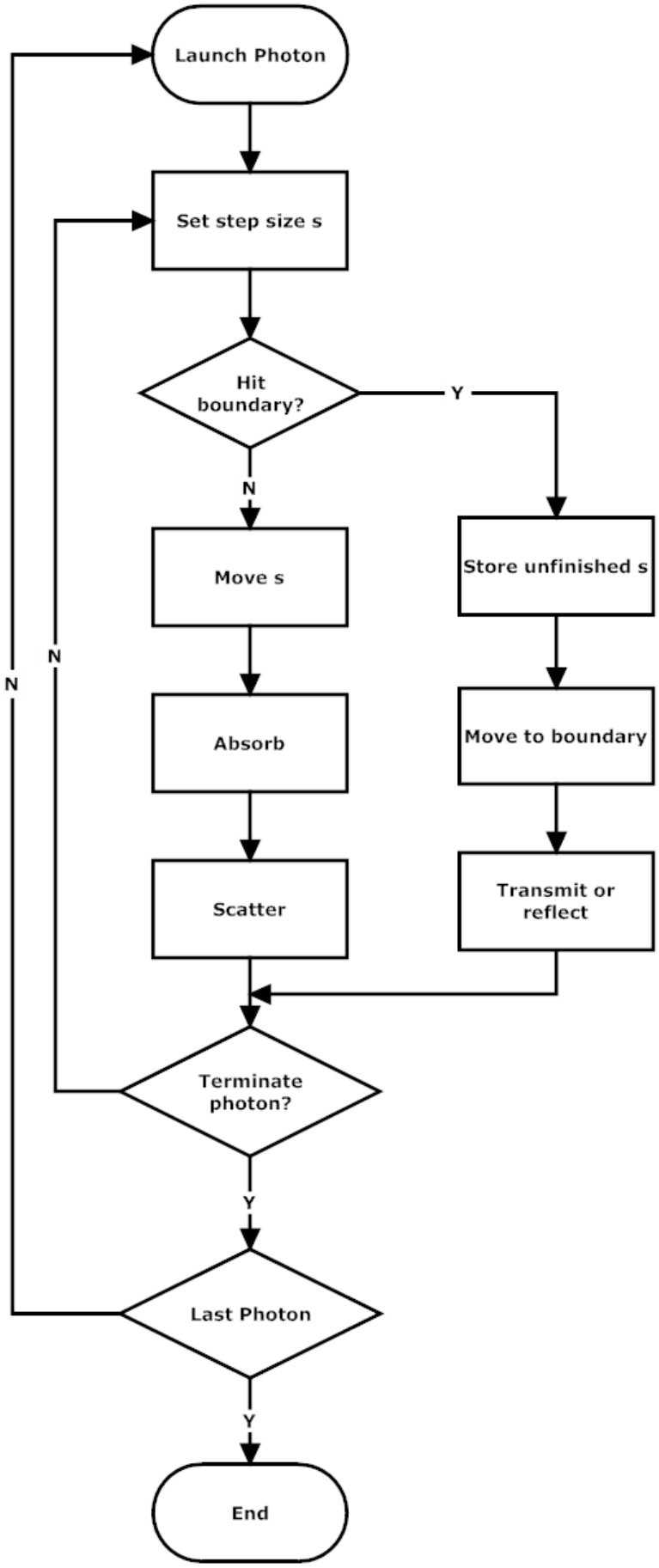

Figure 1.7: Flowchart for Monte Carlo simulation of homogeneous tissue.

where **x,y** and **z** are the unit vectors along each axis. The photon position is initialized to (0,0,0) and the directional cosines are set to (0,0,1). When a photon is launched if there is a mismatched boundary at the tissue surface then a specular reflectance will occur. If the refractive index of the outside medium and tissue are n_1 and n_2, respectively, then the specular reflectance, R_{sp}, is specified as

$$R_{sp} = \frac{(n_1 - n_2)^2}{(n_1 + n_2)^2} \tag{1.5}$$

The effect of the specular reflectance is modeled decrementing the initial weight of each injected photon to $w_0 = 1 - R_{sp}$.

Photon's Step Size

The step of the photon packet is calculated based on a sampling of the probability distribution for photon's free path $s \in [0, \infty)$. There are two ways that may be used to evaluate the step size: the first one is based on the definition of the interaction coefficient, μ_t, the second one is based on the definition of the scattering coefficient, μ_s. According to this choice the way that absorption is modeled will be different as described later.

For the first case the equation that provides a means of choosing step size is

$$s = \frac{-\ln(\xi)}{\mu_t} \tag{1.6}$$

For the second case the equation that is used to sample s is

$$s = \frac{-\ln(\xi)}{\mu_s} \tag{1.7}$$

Both Eqs. (1.6) and (1.7) give a mean free path between photon-tissue interaction sites. The first one considers both scattering and absorption to estimate this path, while the second ones considers only scattering for the punctual interaction.

Moving the Photon Packet

Once the step size s is specified, the photon is ready to be moved in the tissue. The position of the photon packet is updated by

$$x = x' + \mu_x s \tag{1.8}$$
$$y = y' + \mu_y s \tag{1.9}$$
$$z = z' + \mu_z s \tag{1.10}$$
$$\tag{1.11}$$

where the prime index represents the previous coordinates.

Photon Absorption

When a photon propagates it is absorbed only when it meets an absorption centre, and its entire energy is deposited inside the tissue. The most rigorous way to model this situation in the Monte Carlo code is using analog absorption weighting (AAW): for every interaction with the tissue a random number is compared with the probability of absorption defined by μ_a, and if the generated value is smaller then the absorption coefficient the photon is killed.

Two alternative approaches toward modeling the absorption events can be used when the photons are considered as photon packets. These approaches require the introduction of the concept of the photon packet weight w and they are intuitively equivalents to the application of AAW when a large number of photons is traced during the simulation.

The first alternative is to use discrete absorption weighting (DAW). For each step that the photon takes inside the simulating media, a fraction of the photon weight, is deposited inside the simulating media. The amount of deposited photon weight, ΔW, is calculated as

$$\Delta w = w \frac{\mu_a}{\mu_a + \mu_s} \tag{1.12}$$

so when the photon exits the tissue after interacting j times with the tissue, its weight has become

$$w = w_o \left(\frac{\mu_s}{\mu_a + \mu_s} \right)^j \tag{1.13}$$

When this approach is used it is necessary to sample the step size according to the interaction coefficient, thus using Eq. (1.6).

The second method, referred to as continuous absorption weighting (CAW), is based on the application of Beer's law to de-weight exponentially the collected photon proportionally to the total path, l, it has travelled inside the tissue

$$w = w_o \exp(-\mu_a v t) = w_o \exp(-\mu_a l) \tag{1.14}$$

When this method is used it is necessary to use Eq. (1.7) to sample the photon step between interaction sites.

The AAW method is faster and it is a more physical representation of the absorption phenomenon, but the other two approaches should be able to reduce the variance of the measured reflectance and transmittance. It is uninvestigated how much variance can be reduced using DAW or CAW respectively.

Photon Scattering

Once the photon packet has been moved and its weight decremented the photon packet is ready to be scattered.There will be a deflection angle, $\Theta \in [0, \pi)$ and an azimuthal angle $\Psi \in [0, 2\pi)$ to be sampled statistically. The probability distribution function for the cosine of the deflection angle, $\cos\Theta$, is described by the Henyey-Greenstein phase function [14]

$$p(\cos\Theta) = \frac{1 - g^2}{2(1 + g^2 - 2g\cos\Theta)^{3/2}} \tag{1.15}$$

The mapping between $\cos\Theta$ and the random number ξ is

$$\cos\Theta := \begin{cases} \frac{1}{2g}\left\{1 + g^2 - \left[\frac{1-g^2}{1-g+2g\xi}\right]^2\right\}, & \text{if } g \neq 0, \\ 2\xi - 1 & \text{if } g = 0. \end{cases} \tag{1.16}$$

Next the azimuthal angle, which is uniformly distributed in the interval 0 to 2π, is sampled

$$\Psi = 2\pi\xi \tag{1.17}$$

Reflection or Transmission at Boundary

During a step the photon may hit a boundary of the tissue and it may either escape as observed reflectance (or transmittance) or be internally reflected by the boundary. When the step size is large enough to hit the boundary the distance between the current photon location and the boundary in the direction of the photon propagation is evaluated. The photon is moved to the interface free of interaction with the tissue. The remaining step size is updated and it will be travelled only if the photon is internally reflected.

The probability of a photon being internally reflected depends on the angle of incidence, $\alpha_i = \cos^{-1}(|\mu_z|)$. Snell's law indicates the relationship between the angle of incidence, α_i, the angle of transmission, α_t and the refractive indexes of the outside medium and tissue, n_1 and n_2.

$$n_2 \sin\alpha_i = n_1 \sin\alpha_t \tag{1.18}$$

The internal reflectance, $R_F(\alpha_i)$ is calculated by the Fresnel's formula for unpolarized light (Born et al. 1986, Hecht 1987)

$$\mathcal{R}_F\left(\cos(\alpha_i)\right) = \frac{1}{2}\left[\frac{\sin^2(\alpha_i - \alpha_t)}{\sin^2(\alpha_i + \alpha_t)} + \frac{\tan^2(\alpha_i - \alpha_t)}{\tan^2(\alpha_i + \alpha_t)}\right] \tag{1.19}$$

Whenever a photon impinges the upper boundary, it is internally reflected or allowed to escape by comparing a random number with the value computed using Eq. (1.19) [12].

Photon Termination

After a photon packet is launched and traced inside the simulating medium, it can be terminated naturally by reflection or transmission outside the tissue. To reduce the computational burden associated with the simulation additional terminating conditions can be imposed. This is done to avoid the tracing of photons that have travelled inside the tissue for a very long time resulting in very low weight that can be neglected for the measurement of quantities such as the reflectance or the transmittance.

A common termination condition consists in the use of a technique called Roulette on a photon whose weight is below a certain threshold. The Roulette technique gives a photon packet a survival probability. Then a random number is generated and compared with this chance and only if the random number is smaller than the surviving probability the photon packet weight is increased by the inverse of the surviving probability and it keeps on propagate. Another possible termination condition consists in setting a maximum number of interactions that a photon may undergo, or a maximum travelled path inside the tissue.

1.4.5 Scored Physical Quantities

The physical quantities that can be directly simulated are photon absorption, fluence, reflectance and transmittance. These photometric quantities can be measured as a function of space, time and/or angle.

In this work we focus on the measurement of the spatially- and temporally-resolved reflectance, $R(r, t)$, which will be even referred to as temporally-resolved reflectance (TRR) and on the measurement of the spatially-resolved reflectance, $R(r)$, referred to as steady state reflectance (SSR).

TRR data represent the probability that a photon injected inside the tissue at the physical source of the system escapes from the simulating medium at a location r after a time of flight t. The symmetry of the system allowed us to collect photons in annular rings on the surface of the tissue to build up the reflectance signal. This value is computed as

$$R(r_k, t_l) = \frac{1}{\Delta A_k} \frac{1}{\Delta t_l} \frac{1}{N} \sum_{i=1}^{N} w_i \tag{1.20}$$

The photon weight w_i is equal to zero for photons reflected outside the annular bin with area $\Delta A_k = 2\pi r_k \Delta r$ represented by its nominal point, r_k and outside the time gate Δt represented by its nominal point , t_l. ΔA and Δt can be interpreted as the spatial and temporal resolution of the measurement, respectively.

The measured reflectance value would converge to the exact integral value if the number of simulated photons grows without bound. From a practical point of view it is necessary to use a finite number of photons, thus the variance associated with a reflectance value, $R(r_k, t_l)$, measured in the specific can be calculated as [15]

$$\sigma(r_k, t_l) = \sqrt{\frac{1}{N_{inj} - 1}\left(\frac{1}{N_{inj}}\frac{1}{\Delta A_k^2}\frac{1}{\Delta t_l^2}\sum_{i=1}^{M} w_i^2 - R(r_k, t_l)\right)} \tag{1.21}$$

It is possible to measure the spatial distribution of the reflected photons neglecting their time of flight, i.e. the steady state reflectance, as

$$R(r_k) = \frac{1}{\Delta A_k}\frac{1}{N}\sum_{i=1}^{N} w_i \tag{1.22}$$

where r_k is the nominal position of the k-th radial bin of area ΔA_k. Note that $w_i = 0$ for the photons collected outside the bin boundaries. The standard deviation of each steady state reflectance point, $R(r_k)$, is calculated as

$$\sigma(r_k) = \sqrt{\frac{1}{N - 1}\left(\frac{1}{\Delta A_k^2}\frac{1}{N}\sum_{i=1}^{N} w_i^2 - R^2(r_k)\right)} \tag{1.23}$$

To evaluate these quantities through an MC simulation one needs to set a temporal and spatial grid where the photons can be tallied when they escape the propagating medium. Another approach consists in storing all the photon biographies (x_i, y_i, t_i, w_i) of those packets that are not terminated prematurely and post process them to evaluate the desired quantities. Although this approach requires the storage of a large database, it can be a good option when one does not want to fix the detection resolution *a priori*.

1.4.6 My Monte Carlo

To master my understanding of the Monte Carlo technique I have implemented a C# version of the MCML code modifying it for temporal applications and neglecting the layer structure. This process let me become familiar with the C# developing language and environment, it allowed me to focus on every specific step of MC simulations of photon transfer inside tissues and it made me understand the logical flow of the simulation and the way the code can be built.

To gain familiarity with the graphical users interface (GUI) tools and controls I implemented a simple GUI, shown in Fig. 1.8, that can be used to set input and parameters of the MC simulation code.

The step size is calculated according to the interaction coefficient using Eq. (1.6), thus DAW (Eq. (1.13)) is used to model the signal losses due to absorption. The Henyey-Greenstein phase function (Eq. 1.15) is sampled to evaluate the scattering direction after each tissue-photon interaction. The Roulette method with threshold weight $w_{th} = 10^{-4}$ and with surviving probability $p = 0.1$ is used. Each simulated photon packet is directly tallied into a spatial and temporal grid to evaluate the spatially- and temporally-resolved reflectance and transmittance. The user inputs the number of photons, the source location, the thickness of the infinite slab, the limits of the physical domain of

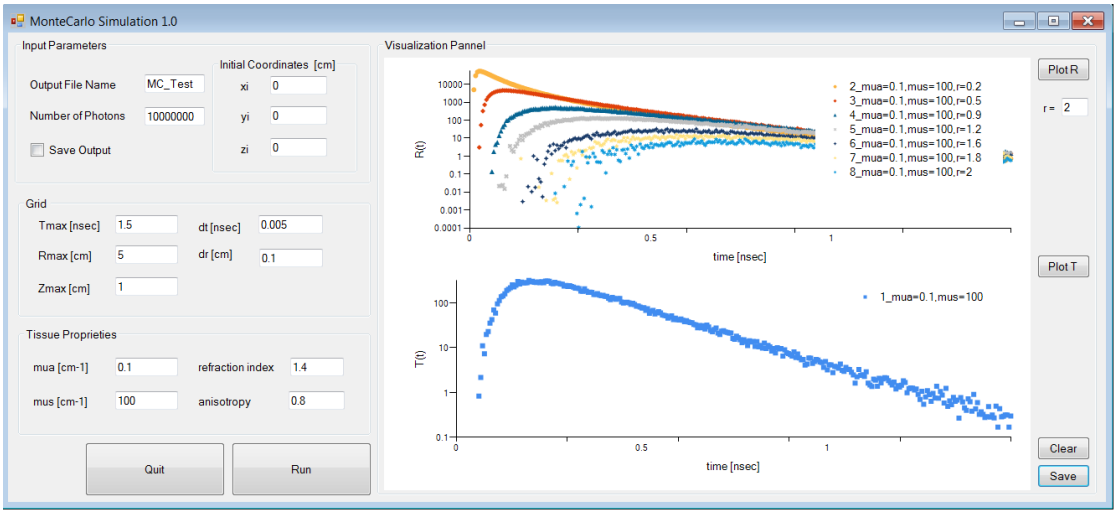

Figure 1.8: GUI implemented with the Chart Control tools for Visual C# 2008.

measurement, the spatial and the temporal resolution of the detection and the optical properties of the tissue.

The same GUI can be used to visualize $R(r, t)$ and $T(r = 0, t)$ after the simulation is completed. This code has been validated comparing its output with the results of the original MCML code. This code has not been used for the work that is presented in the following chapters of this work.

Chapter 2

Single Monte Carlo Model

2.1 Introduction

The study of light transport within biological tissues for the development of therapeutic and diagnostic applications is attracting great attention in the scientific community. Much effort has been made to develop techniques that characterize the physiological state of biological tissues through the analysis of spectroscopy signals using visible or near infrared light. The propagation of light in turbid media, commonly referred to as photon migration, is a phenomenon that can be described by the RTE (Eq. (1.1)).

In contrast with modeling light as the propagation of electromagnetic fields, this theoretical model rather considers the transport of energy in terms of propagation of single particles within the medium. The RTE can be obtained by performing a balance for the radiance $L(r, \hat{\Omega}, t)$ which represents the rate at which energy arrives at a fixed location r at a given time t in a given direction $\hat{\Omega}$.

The RTE is physically intuitive but very difficult to solve analytically and much effort has been devoted to develop approximate analytical expressions that can be used to determine the reflectance of biological tissues. However, the range of applicability of these analytical model has to be carefully examined because its accuracy can break down in cases where the absorption coefficient is large relative to the reduced scattering, $\mu_s' = (1 - g)\mu_s$ [4], in the presence of physical boundaries, or when the source - detector separation is not much larger then transport mean free path, $l^* = (\mu_a + \mu_s')^{-1}$ [5].

To overcome these limitations, Monte Carlo (MC) simulations have been introduced in the field of biomedical optics [6] and they have become a de-facto gold standard for modeling photon migration in tissue optics.

MC itself is a meshless computation; however a mesh is needed to extract information from the simulation output. For example to obtain the spatially- and/or temporally-resolved reflectance, $R(r, t)|_{z=0}$, at a given location (r_0, t_0) it is necessary to integrate the radiance over the whole upper pointing hemisphere, S^{2-} and over the spatial and temporal interval covered by the bin in which the photons are collected

$$R(r_0, t_0) = \frac{1}{\Delta A \Delta t} \int_{t_0}^{t_0+\Delta t} \int_{r_0}^{r_0+\Delta r} \int_{S^{2-}} L(r, \hat{\Omega}, t)\ \mathrm{d}\hat{\Omega}\ 2\pi r\ \mathrm{d}r\ \mathrm{d}t \tag{2.1}$$

where

$$\Delta A = \pi(r_0 + \Delta r)^2 - \pi {r_0}^2 \tag{2.2}$$

Many different photons will, in general, exit the same cylindrical ring within the same time interval, so when all these events are gathered to obtain the value of $R(r_0, t_0)$, a discretization error occurs because the quadrature interval has been represented by the nominal values (r_0, t_0). The magnitude of this error goes to zero as the number of simulated random walks increases without bound and as the integration interval becomes infinitesimal.

For this reason the propagation of a large number of photons must be simulated to achieve good statistics for the measured reflectance in all the bins of interest. As a result the computational burden associated with the simulation is often very large and conventional MC methods are not suitable for use in iterative algorithms where the optical properties are estimated by comparison of simulated results with actual experimental measurements. This problem led us to examine the potential use of a single MC (sMC) simulation to provide results for a broad range of optical properties.

Several investigations have been proposed to overcome the computational cost associated with the application of MC to homogeneous tissues.

Graaf and co-workers [16] first investigated the possibility of using a single MC simulation to obtain results for different sets of optical properties. Their work showed that the simulated trajectories of the unabsorbed photons in a single Monte Carlo simulation can be used to estimate the total reflectance and absorption of turbid slabs for various values of the albedo, $a = \mu_s/(\mu_a + \mu_s)$, if the number of interactions within the simulated medium is stored. Moreover the remitted photon densities for a semi-infinite medium as a function of the source-detector separation can be derived for different values of a if the total interaction coefficient, $\mu_t = \mu_a + \mu_s$, is held constant.

Kienle and Patterson [1] extended the idea of sMC to the time-resolved reflectance domain, $R(r, t)$, and developed a technique that allows the determination of the spatially- and/or temporally-resolved reflectance of turbid semi-infinite media from the results of a single MC simulation. This method is based on the concept of scaling and de-weighting the reflectance estimates provided by a reference MC simulation for a non-absorbing medium. Such an absorption free simulation is commonly referred to as white Monte Carlo (wMC). Each bin of the discrete representation of the reference reflectance is represented by a single specific value of time and position. Therefore when the scaling is applied, it becomes necessary to interpolate the points along both space and time coordinates to evaluate continuously the diffuse reflectance for different values of optical properties. The process of binning and interpolating introduces errors which are amplified further when the scaling is applied.

Pifferi et al. [17] used the sMC method to generate a library of time-resolved reflectance curves which can be interpolated for real-time fitting of experimental data. Following a slightly different approach they extended the method to include even time resolved transmittance curves. For both cases they tested the proposed method both on simulation results and on experimental results. The

proposed method was proved to be efficient for the quick and accurate fit of both μ_s and μ_a for a small distance between the injection and the collection fibers and for low scattering values.

Alerstam et al. [18] developed a scheme for fully scalable wMC based on the application of Kienle's method on a photon-by-photon basis. This means that spatial and temporal binning are turned into post-simulation activities so that no averaging is performed until the final output is provided and the interpolation problems are avoided. This approach requires the storage of all the radial exit positions and the total path length of each detected photon, which are individually reprocessed to evaluate the photon parameters for a variation of the optical scattering and/or absorption.

To overcame the homogeneous media limitation the concept of a perturbation Monte Carlo (pMC) method has been introduced [19, 20] and used to solve inverse photon migration problems in heterogeneous tissues. The pMC method is based on post-processing the output of a single simulation performed in a reference system. Again, the data is stored on a per-photon basis and the output for a perturbed system can be derived by re-weighting the recorded photon biographies based on the detail of their trajectory through the modified medium. The pMC approach also extracts derivative informations from a random walk database to permit the rapid determination of rates of change in the detected photon signal with respect to perturbations in background tissue optical properties. The re-weighting process produces the theoretically correct integral estimates as the number of simulated random walks increases without bound. However, the perturbative nature of the model requires to carefully evaluate the impact of the finiteness of the set of random walk on the magnitude of the optical perturbations which can be accurately modeled.

While sMC has been widely used by the biomedical community a clear theoretical framework has never been presented to support the origin of the scaling relations. Once these are established one is in a better position to evaluate the effects of binning and interpolation on the subsequent errors.

The objective of this part of my thesis work is to establish a full analytical justification of the sMC method based on the RTE, validate the sMC approach by testing its equivalence with traditional MC techniques using a statistical analysis and describe the binning and interpolating techniques used to implement the forward solver.

2.2 Theory of the Single Monte Carlo Method

The sMC approach has been adopted as a forward solver to simulate reflectance data in the time domain and in the temporal and spatial frequency domains [3, 21, 22, 23]. It has also been used to recover the optical coefficients from experimental data [24, 17]. To our knowledge no rigorous theoretical justification has been published for this method. In this section the scaling equations on which the sMC method relies are derived from the RTE.

Two basic ideas are involved in the application of the sMC method to derive the spatial and temporal resolved reflectance in a semi-infinite homogeneous medium. The first one is that the reflectance, $R(r,t)$, for an arbitrary value of the scattering coefficient is related to a reference reflectance $R_r(r,t)$ that is obtained through the simulation for a medium with $\mu_a = \mu_{a,r}$ and $\mu_s = \mu_{s,r}$. This mapping is done through the first scaling relationship presented by Kienle [1]

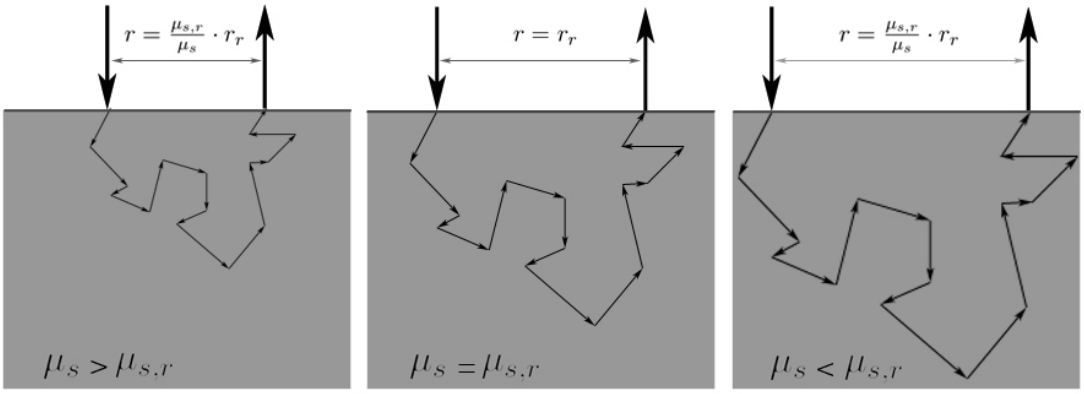

Figure 2.1: Example of the linear scaling of the path length induced by a variation of the scattering coefficient.

$$R(r,t)\Big|_{\mu_s \neq \mu_{s,r};\, \mu_a = \mu_{a,r}} = \frac{\mu_s^3}{\mu_{s,r}^3} R_r\left(\frac{\mu_s}{\mu_{s,r}} r, \frac{\mu_s}{\mu_{s,r}} t\right) \tag{2.3}$$

Figure 2.1 shows the effect of the linear scaling due to a scattering variation on the photon path inside the tissue. A larger value of μ_s results in the shrinking of the distance between the photon-tissue interaction sites, while a smaller value of μ_s results in the stretching of the photon paths.

The second relationship presented in the same work to derive $R(r,t)$ for an arbitrary value of the absorption coefficient from the reference reflectance obtained from a simulation with $\mu_{a,\,r} = 0$ and $\mu_s = \mu_{s,\,r}$ is

$$R(r,t)\Big|_{\mu_s = \mu_{s,r};\, \mu_a \neq 0} = R_r(r,t) \exp\Big(-\mu_a v t\Big) \tag{2.4}$$

where $v = c/n$ is the speed of light inside the simulating medium. In this work we consider a geometry with cylindrical symmetry to study the reflectance as a function of the source detector separation, r, but the ideas involved in the sMC method do not require this restriction.

Scattering Scaling

To fully justify the first scaling relation (Eq. (2.3)), we start from the Radiative Transport Equation for a non-absorbing medium without internal sources

$$\frac{1}{v}\frac{\partial L(r,\hat{\Omega},t)}{\partial t} + \nabla L(r,\hat{\Omega},t)\cdot\hat{\Omega} = -\mu_s L(r,\hat{\Omega},t) + \mu_s \int_{4\pi} p(\hat{\Omega}' \to \hat{\Omega}) L(r,\hat{\Omega}',t)\, \mathrm{d}\Omega' \tag{2.5}$$

and we introduce the dimensionless variables

$$\begin{cases} \tau = \mu_s v t \\ \rho = \mu_s r \\ \widetilde{\Lambda}(\rho, \hat{\Omega}, \tau) = L(r, \hat{\Omega}, t)/L_0 \end{cases} \tag{2.6}$$

where τ is a dimensionless time, ρ is a dimensionless position and $\widetilde{\Lambda}(\rho, \hat{\Omega}, \tau)$ is a dimensionless radiance defined as the ratio between the radiance, $L(r, \hat{\Omega}, t)$, and a characteristic radiance L_0. Nondimensionalizing the RTE using these variables we obtain

$$\frac{\partial \widetilde{\Lambda}(\rho, \hat{\Omega}, \tau)}{\partial \tau} + \nabla \widetilde{\Lambda}(\rho, \hat{\Omega}, \tau) \cdot \hat{\Omega} = -\widetilde{\Lambda}(\rho, \hat{\Omega}, \tau) + \int_{4\pi} p(\hat{\Omega}' \to \hat{\Omega}) \widetilde{\Lambda}(\rho, \hat{\Omega}', \tau) \, \mathrm{d}\Omega' \tag{2.7}$$

We also need to non-dimensionalize the boundary conditions. For the problem of interest we require that the radiance vanishes as $r \to \infty$, so

$$L(r \to \infty, \hat{\Omega}, t) \to 0 \tag{2.8}$$

For a semi-infinite geometry with a refractive index mismatch, we have [25]

$$L(r, -\hat{\Omega}, t) = \mathcal{R}_F(\hat{n} \cdot \hat{\Omega}) L(r, \hat{\Omega}_r, t), \qquad r \in S, \qquad \hat{n} \cdot \hat{\Omega} > 0 \tag{2.9}$$

where $\mathcal{R}_F$ is the angular distribution of the Fresnel reflectance for unpolarized light, $\hat{n}$ is the outward pointing unit normal vector and $-\hat{\Omega}_r$ is the unit vector in the direction of the reflected ray for incident direction $\hat{\Omega} = \hat{\Omega}_i$. Thus $\mathcal{R}_F(\hat{n} \cdot \hat{\Omega})$ represents the internal reflectance probability for a photon hitting the surface with a refractive index discontinuity. Replacing the dimensional variables by the non-dimensional ones, Eq. (2.8) becomes

$$\widetilde{\Lambda}(\rho \to \infty, \hat{\Omega}, \tau) \to 0 \tag{2.10}$$

while the Fresnel condition becomes

$$\widetilde{\Lambda}(\rho, -\hat{\Omega}, \tau) = \mathcal{R}_F(\hat{n} \cdot \hat{\Omega}) \widetilde{\Lambda}(\rho, \hat{\Omega}_r, \tau), \qquad \rho \in S, \qquad \hat{n} \cdot \hat{\Omega} > 0 \tag{2.11}$$

Thus the form of the boundary conditions is not altered as a result of the non-dimensionalization. From this we conclude that the rigorous application of the sMC method is limited to infinite and semi-infinite geometries.

Having defined the boundary conditions, the diffuse reflectance emitted from the top surface, $R(r, t)\Big|_{z=0}$, over the whole upper pointing hemisphere, S^{2-}, can be defined as

$$R(r, t) = \int_{S^{2-}} \mathcal{R}_F(\hat{n} \cdot \hat{\Omega}) L(r, \hat{\Omega}, t) \, \mathrm{d}\hat{\Omega} \tag{2.12}$$

By analogy a dimensionless reflectance can be defined as

$$\widetilde{R}(\rho,\tau) = \int_{S^{2-}} \mathcal{R}_F(\hat{n}\cdot\hat{\Omega})\widetilde{\Lambda}(\rho,\hat{\Omega},\tau)\ \mathrm{d}\hat{\Omega} \tag{2.13}$$

To derive Eq. (2.3) we consider the dimensionless analog of Eq. (2.1)

$$\widetilde{R}(\rho_0,\tau_0) = \frac{1}{\Delta\hat{A}\Delta\tau}\int_{\tau_0}^{\tau_0+\Delta\tau}\int_{\rho_0}^{\rho_0+\Delta\rho}\int_{S^{2-}} \widetilde{\Lambda}(\rho,\hat{\Omega},\tau)\ \mathrm{d}\hat{\Omega}\ 2\pi\rho\ \mathrm{d}\rho\ \mathrm{d}\tau \tag{2.14}$$

where

$$\Delta\hat{A} = \pi(\rho_0+\Delta\rho)^2 - \pi{\rho_0}^2 \tag{2.15}$$

Since the ratio between the radiance, $L(r,\hat{\Omega},t)$, and the dimensionless radiance, $\widetilde{\Lambda}(\rho,\hat{\Omega},\tau)$, is defined as L_0, one can easily verify that the ratio between $R(r,t)$ and $\widetilde{R}(\rho,\tau)$ is also equal to L_0.

The triple integral in Eq. (2.1) corresponds to a characteristic reflected energy $E_0 = Nh\nu$ which is equal to the product of the total number, N, of photons emitted in the bin represented by r_0 and t_0, and of the energy of each photon, $h\nu$. The equivalent integral in Eq. (2.14) represents the total number of dimensionless particles reflected at the top surface. Because we integrate $L(r,\hat{\Omega},t)$ and $\widetilde{\Lambda}(\rho,\hat{\Omega},\tau)$ ove equivalent spatial and temporal ranges, we can write

$$\int_{t_0}^{t_0+\Delta t}\int_{r_0}^{r_0+\Delta r}\int_{S^{2-}} L(r,\hat{\Omega},t)\ \mathrm{d}\hat{\Omega}\ 2\pi r\ \mathrm{d}r\ \mathrm{d}t = E_0\int_{\tau_0}^{\tau_0+\Delta\tau}\int_{\rho_0}^{\rho_0+\Delta\rho}\int_{S^{2-}} \widetilde{\Lambda}(\rho,\hat{\Omega},\tau)\ \mathrm{d}\hat{\Omega}\ 2\pi\rho\ \mathrm{d}\rho\ \mathrm{d}\tau \tag{2.16}$$

Using this identity, we find that L_0 is the ratio between the reflectance and the dimensionless reflectance

$$L_0 = \frac{R(r_0,t_0)}{\widetilde{R}(\rho_0,\tau_0)} = h\nu\frac{\Delta\hat{A}\Delta\tau}{\Delta A\Delta t} = h\nu\mu_s^3 v \tag{2.17}$$

With this definition for L_0, the diffuse reflectance can be written in terms of the dimensionless reflectance as

$$R(r,t) = v\mu_s^3 E_0\int_{S^{2-}} \widetilde{\Lambda}(\rho,\hat{\Omega},\tau)\ \mathrm{d}\hat{\Omega} = v\mu_s^3 E_0\widetilde{R}(\rho,\tau) \tag{2.18}$$

This equation shows that the diffuse reflectance for a specific value of the scattering coefficient is uniquely related to the dimensionless reflectance multiplied by a reference radiance L_0.
To justify Eq. (2.3) we consider a reference value for the scattering coefficient $\mu_s = \mu_{s,r}$. According to the last equation, the reference signal used in Kienle's method can be expressed as

$$R_r(r,t) = v\mu_{s,r}^3 E_0\widetilde{R}_r(\rho,\tau) = v\mu_{s,r}^3 E_0\widetilde{R}_r(\mu_{s,r}r, v\mu_{s,r}t) \tag{2.19}$$

while the diffuse reflectance for an arbitrary value of μ_s becomes

$$\begin{aligned} R(r,t) &= v\mu_s^3 E_0 \widetilde{R}(\rho,\tau) = v\mu_s^3 E_0 \widetilde{R}\left(\frac{\mu_s}{\mu_{s,\,r}}\mu_{s,\,r} r,\, \frac{\mu_s}{\mu_{s,\,r}} v\mu_{s,\,r} t\right) \\ &= v\mu_s^3 E_0 \widetilde{R}\left(\frac{\mu_s}{\mu_{s,\,r}}\rho_r,\, \frac{\mu_s}{\mu_{s,\,r}}\tau_r\right) \end{aligned} \tag{2.20}$$

Rewriting the dimensionless reflectance in the last equation as

$$\widetilde{R}\left(\frac{\mu_s}{\mu_{s,\,r}}\rho_r,\, \frac{\mu_s}{\mu_{s,\,r}}\tau_r\right) = R_r\left(\frac{\mu_s}{\mu_{s,\,r}} r,\, \frac{\mu_s}{\mu_{s,\,r}} t\right) \frac{1}{v\mu_{s,\,r}^3 E_0} \tag{2.21}$$

and substituting it into Eq. (2.20), we obtain Eq. (2.3)

$$R(r,t) = \frac{\mu_s^3}{\mu_{s,\,r}^3} R_r\left(\frac{\mu_s}{\mu_{s,\,r}} r,\, \frac{\mu_s}{\mu_{s,\,r}} t\right) \tag{2.22}$$

We have already noted that the inherent nature of the MC simulation requires no mesh, but one needs to discretize the measurement domain to obtain interpretable results. Because of the consequent discretization error the application of Eq. (2.3) on a reference reflectance generated from a MC simulation constitutes an approximation to the exact reflectance.

Absorption Scaling

Now to derive the second scaling relation (Eq. (2.4)) we rewrite Eq. (2.1) as

$$R(r_0,t_0) = \frac{1}{\Delta A \Delta t}\int_{t_0}^{t_0+\Delta t}\int_{r_0}^{r_0+\Delta r}\int_{S^{2-}} h\nu v N(r,\hat{\Omega},t)\; \mathrm{d}\hat{\Omega}\; 2\pi r\; \mathrm{d}r\; \mathrm{d}t \tag{2.23}$$

where $N(r,\hat{\Omega},t)$ is the number of photons collected within the time interval $[t_0,\ t_0+\Delta t]$ and within the radial bin $[r_0, r_0+\Delta r]$.

The result of the tracing of a photon during a MC simulation consists in the photon exit radial position, r_i, its time of flight within the medium, t_i, and its weight, w_i. The concept of a photon weight has been introduced to model the absorption of light in MC simulations, to reduce the variance of the results. Absorption itself is an analog phenomenon, when a photon is absorbed its entire energy is lost and eventually reemitted as fluorescence. Thus each photon that is emitted counts as a unit energy.

Anyway it has been shown [26] that it is possible to model the loss due to absorption reducing continuously the photon weight according to its pathlength inside the medium without biasing the results using CAW (Eq. (1.14)).

If we consider a wMC simulation as our reference simulation and we integrate over all the possible directions we can calculate N_r as the sum of all the weights of the photons emitted from the top surface within the specific bin

$$N_r(r_0, t_0) = \sum w_i = \sum w_0 \tag{2.24}$$

where $w_0 = 1 - R_{sp} = 1 - (\Delta n)^2/(1 + \Delta n)^2$ is the initial weight of the photon reduced by the specular reflection given by the refractive index mismatch between air and tissue. Thus we can express the reference reflectance for the bin represented by r_0 and t_0 as

$$R_r(r_0, t_0) = \frac{1}{\Delta A \Delta t} \int_{t_0}^{t_0+\Delta t} \int_{r_0}^{r_0+\Delta r} \int_{S^{2-}} h\nu v N_r(r_0, t_0)\, \mathrm{d}\hat{\Omega}\, 2\pi r\, \mathrm{d}r\, \mathrm{d}t \tag{2.25}$$

For a MC simulation with $\mu_a \neq 0$ the weight of each photon would be decreased exponentially according to Beer's law, so in the same bin we would tally

$$N(r_0, t_0) = \sum w_i = \sum w_0 \exp(-\mu_a v t_i) \approx \exp(-\mu_a v t_0) \sum w_0 = \exp(-\mu_a v t_0) N_r \tag{2.26}$$

and we can write

$$\begin{aligned} R(r_0, t_0) &\approx \frac{1}{\Delta A \Delta t} \int_{t_0}^{t_0+\Delta t} \int_{r_0}^{r_0+\Delta r} \int_{S^{2-}} h\nu v N_r(r_0, t_0) \exp(-\mu_a v t_0)\, \mathrm{d}\hat{\Omega}\, 2\pi r\, \mathrm{d}r\, \mathrm{d}t \\ &= R_r(r_0, t_0) \exp(-\mu_a v t_0) \end{aligned} \tag{2.27}$$

If we consider continuous spatial and temporal variables we obtain the expression

$$R(r, t) = R_r(r, t) \exp(-\mu_a v t) \tag{2.28}$$

Note that Eq. (2.28) is rigorous only if applied on a photon-by-photon basis, i.e. t must be calculated for each individual photon. However it is only an approximation when it is applied to ensemble averages of reflected photons collected in discrete bins. The difference between the real value of $R(r_0, t_0)$ and the right hand side of Eq. (2.28) can be bounded by the product of the largest value of the integrand multiplied by the interval of integration. This implies that it is possible to analyze this error as a function of the size of the bins and of the variation of the integrand over the domain of integration.

The sMC method can be used to evaluate the spatially-resolved reflectance, $R(r)$. After scaling and de-weighting the spatially- and temporally- resolved reference it is necessary to integrate the $R(r, t)$ surface along the temporal dimension to obtain the spatially-resolved curve.

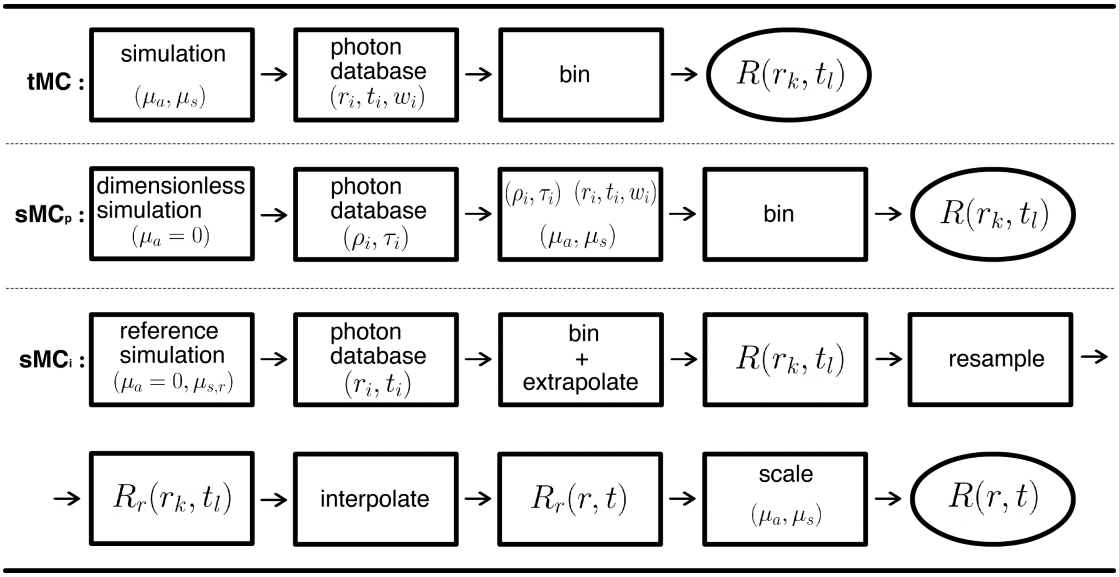

Figure 2.2: Flowchart of the steps that have been followed to obtain the spatially and temporally resolved reflectance using the different approaches examined in this work.

2.3 Single Monte Carlo Validation

The flowchart in Fig. 2.2 illustrates the three approaches examined in this study to obtain a measurement of the time and space resolved reflectance on the boundary of a semi-infinite homogeneous medium from MC simulations.

In the first approach, a traditional Monte Carlo (tMC) simulation is used to provide a gold standard. The second method is based on the single Monte Carlo approach applied on a photon-by-photon basis (sMC$_p$). The last approach is equivalent to the one proposed by Kienle and Patterson: the reflectance for any value of the optical scattering and absorption $R(r, t)$ is obtained by scaling a reference signal $R_r(r, t)$ obtained from a wMC simulation with $\mu_s = \mu_{s,r}$. As this method is based on the interpolation of the reference reflectance we denote it as sMC$_i$.

The MC code used for this work is a version of MCML developed by Jacques and Wang [12] modified for temporal applications. All the simulations run for this study injected photons in a semi-infinite homogeneous medium with $n = 1.4$ using a pencil beam with normal incidence placed on the top surface. For the anisotropy factor a value of $g = 0.8$ was chosen because most of the biological tissues have an anisotropy factor greater the 0.8 [27]. As reported by different authors [1, 17], the reflectance emitted from media with high anisotropy factor, $g > 0.8$, is relatively insensitive to the presumed value of g. In any event, in this work we did not analyze the possibility of representing the reflectance for values of $g \neq 0.8$.

A Roulette method is used to determine whether a photon hitting the $z = 0$ surface is internally reflected or if it escapes the boundary as observed reflectance. The Henyey-Greenstein phase function [14] was sampled after every collision event to evaluate the direction of the photon propagating within the simulating media. The simulated photons were terminated before exiting the

semi-infinite medium if they reach a maximum number of collisions, set to $3 \cdot 10^5$ for this study. This limitation was necessary to control the computational time that would be used to trace photons that travel a very large path, carrying a very small weight, nearly ineffective on the result.

To achieve good statistics, 10^8 photons have been injected for each simulation. The time required to simulate these photon trajectories is almost one week. For this reason the Broadcom Distributed United Cluster (BDUC) at University of California Irvine has been used.

Traditional Monte Carlo (tMC)

By a traditional MC simulation we mean a simulation executed with the specific value of the scattering coefficient, where the step size is sampled using the probability density function $s = -\ln(\xi)/\mu_s$, where ξ is a random number uniformly distributed in the interval [0-1]. For each injected photon the exact exit position, r_i, and the total time of flight, t_i, are recorded. The weight of each photon, w_i is then calculated according to the photon path inside an absorbing medium with a specific value of μ_a using Eq. (1.14).

To reduce the computational burden associated with the simulation an additional termination condition has been imposed: when a photon reaches a depth larger then 1 m it is terminated because its final weight would be very small. Once the photon database (r_i, t_i, w_i) is obtained, the recorded weights of the photons are averaged over a set of spatial and temporal bins in order to obtain the reflectance signal.

Single Monte Carlo Photon by Photon (sMC$_p$)

The application of the sMC principle on a photon-by-photon basis requires to simulate the photon trajectories and store the photon database only for a single simulation. As the theoretical demonstration developed is based on the non-dimensionalization of the RTE we used a dimensionless wMC simulation. This means that no value of the scattering coefficient is defined and the step size is sampled as $s = -\ln(\xi)$. A dimensionless maximal depth was imposed to match the termination condition of the tMC simulations. For all the photons that exit the media their dimensionless position and time (ρ_i, τ_i) was recorded.

It is important to note that the presence of the boundary is treated in the same way whether we use a dimensionless or a traditional simulation. From the Monte Carlo simulation point of view the refractive index mismatch at the top surface is accounted using the Fresnel's formula for unpolarized light (Eq. (1.19)). Whenever a photon impinges the upper boundary, it is internally reflected or allowed to escape by comparing a random number with the value computed using Eq. (1.19) [12]. For the same sequence of random numbers this result will always be the same, independently from the introduction of a spatial metric. The weight of all the emitted photons, $w_i = 1 - R_{sp}$, is constant along all the collected particles.

To obtain the temporally and spatially resolved reflectance for any value of μ_a and μ_s it is first necessary to use Eq. (2.6) which relates the actual exit position and time,r_i and t_i, to their dimensionless counterpart. Once the total time of flight is known Beer's law is applied to derive the

weight w_i of each photon. Once the dimensionless database is processed to obtain the required data the reflectance values can be calculated using the same procedure used for the tMC dataset.

Interpolated Single Monte Carlo (sMC$_i$)

The MC simulation used to build up the reference reflectance $R_r(r, t)$ has the same characteristics of a tMC simulation and it was run with $\mu'_{s,r} = 1$ mm^{-1} and $\mu_a = 0$. The photon database generated has been processed in order to obtain the reference reflectance in a set of nominal positions, $R_r(r_k, t_l)$. These values are then interpolated and the reflectance for any combination of optical properties has been obtained using Eqs. (2.3) - (2.4).

Statistical Analysis

One of the goals of this work was to understand if the single Monte Carlo technique can be used to estimate the diffuse reflectance and its spatial and temporal distribution for a wide range of optical properties relevant for biological optics applications in semi-infinite media. As we have previously established the equations upon which the sMC$_i$ method relies is an approximation due to the necessity of discretizing the measurement domain in order to obtain the reference reflectance.

However, as we have demonstrated in § 2.2, the sMC$_p$ and the tMC methods should be fully equivalent. Here we perform a statistical analysis to prove the equivalence between the two approaches. This investigation is required even because the actual simulation is not ideal due to specific characteristics of the MC simulations, i.e., premature termination of photons and finiteness of geometry elements. Thus it is useful to explore the range of optical properties where the two methods are equivalent in practice to understand if the sMC model should exhibits a breakdown with the optical properties.

For all the pairs tested (μ_s,μ_a) we compared sMC$_p$ and tMC data in terms of some global values which can be evaluated without limiting the spatial or temporal range of the measurement and without having to introduce any inaccuracy caused by binning or interpolation. The global values chosen are the total reflectance, R_{tot}, the first moment, $\langle t \rangle$, of the time resolved reflectance, $R(t)$, and the first moment ,$\langle r \rangle$, of the radial resolved reflectance, $R(r)$, of all the collected photons [28].

These values are characteristic for the output of a MC simulation and can be compared to understand if the parent population, from which the random events are sampled, are equivalent using the tMC approach or the sMC$_p$ technique.

We define the total reflectance, $R_{tot} = R_{tot}(\mu_a, \mu_s)$, as the probability that a photon which enters a semi-infinite tissue with the specific optical properties, escapes anywhere from the top surface of the medium. From the RTE we write R_{tot} as

$$R_{tot} = \int_{t=0}^{\infty} \int_{r=0}^{\infty} \int_{S^{2-}} (1 - R_{sp}) L(r, \hat{\Omega}, t) \, \mathrm{d}\hat{\Omega} \, 2\pi r \, \mathrm{d}r \, \mathrm{d}t \tag{2.29}$$

where $(1 - R_F)$ is an efficiency factor which takes into account the effect of the specular reflection of the photons injected into the sample with a pencil beam at the origin. R_{tot} can be estimated from a MC simulation as the sum of the photon weights divided by the number of photons launched, N,

$$R_{tot} \approx \bar{R}_{tot} = \frac{1}{N} \sum_{i=1}^{N} w_i \tag{2.30}$$

$\bar{R}_{tot}$ is an estimate of the true mean, R, of the weight of the reflected photons, whose accuracy is related to the variance σ^2 of the parent population. The termination process, introduces a systematic error in the determination of $\bar{R}_{tot}$ from the results of a MC simulation because the weight of the terminated photons is set to zero. In all the investigated cases the percentage of terminated photons was smaller then 1.2%. It is important to note that the systematic error given by the termination process decreases exponentially with μ_a. The sample variance associated with the estimated reflectance is

$$var[\bar{R}_{tot}] = \frac{1}{N^2} \sum_{i=1}^{N} var(w_i) = \frac{1}{N} \left(\frac{1}{N} \sum_{i=1}^{N} w_i^2 - \bar{R}_{tot}^2 \right) = \frac{1}{N} s_R^2 \approx \frac{1}{N} \sigma_R^2 \tag{2.31}$$

where s_R^2 is the variance of the weights of the photons collected during the simulation.

The first moment of the radial distribution of the photons escaping the top surface, $\langle r \rangle$ is the expectation value of the variable r relative to the probability density function (pdf) $\mathcal{P}[R(r)]$

$$\langle r \rangle = \int_0^{\infty} r \mathcal{P}[R(r)] \, \mathrm{d}r \tag{2.32}$$

From the RTE we can write the pdf as

$$\mathcal{P}[R(r)] = \frac{\int_{t=0}^{\infty} \int_{r-dr}^{r+dr} \int_{S^{2-}} (1 - R_F) L(r, \hat{\Omega}, t) \, \mathrm{d}\hat{\Omega} \, 2\pi r \, \mathrm{d}r \, \mathrm{d}t}{R} \tag{2.33}$$

where the denominator is introduced to normalize the probability density function. For a discrete radial location r_k representative of the radial bin Δr_k it is possible to estimate $\mathcal{P}[R(r)]$ from the database generated through a MC simulation

$$\mathcal{P}[R(r_k)] \approx \frac{\frac{1}{N} \sum_{i=1}^{N} a_i w_i}{\bar{R}_{tot}} \qquad \text{where } a_i = \begin{cases} 1, & \text{if } r_i \in \Delta r_k, \\ 0, & \text{otherwise.} \end{cases} \tag{2.34}$$

The mean radial exit position can be estimated as

$$\langle r \rangle \approx \bar{r} = \frac{\frac{1}{N} \sum_{i=1}^{N} r_i w_i}{\bar{R}_{tot}} = \frac{\sum_{i=0}^{N} r_i w_i}{\sum_{i=0}^{N} w_i} \tag{2.35}$$

The sample variance associated with the calculated value of $\bar{r}$ is

$$var[\bar{r}] = \frac{1}{N}\left(\frac{1}{N}\frac{\sum_{i=1}^{N} r_i^2 w_i}{\sum_{i=1}^{N} w_i} - [\bar{r}]^2\right) = \frac{1}{N}s_r^2 \approx \frac{1}{N}\sigma_r^2 \tag{2.36}$$

where s_r^2 is the variance of the radial exit position of the photons collected during the simuation.

The first moment of the temporal distribution, $\langle t \rangle$, is the mean time of flight of the photons emitted by the surface S

$$\langle t \rangle = \int_0^\infty t\mathcal{P}[R(t)]\ dt \tag{2.37}$$

where

$$\mathcal{P}[R(t)] = \frac{\int_{t-dt}^{t+dt}\int_{r=0}^{\infty}\int_{S^{2-}}(1-R_F)L(r_{z=0},\hat{\Omega},t)\ \mathrm{d}\hat{\Omega}\ 2\pi r\ \mathrm{d}r\ \mathrm{d}t}{R} \tag{2.38}$$

$\mathcal{P}[R(t)]$ can be estimated for a discrete discrete time value t_l representative for the time bin Δt_r from a MC simulation as

$$\mathcal{P}[R(t_l)] \approx \frac{\frac{1}{N}\sum_{i=1}^{N} b_i w_i}{\bar{R}_{tot}} \qquad \text{where } b_i = \begin{cases} 1, & \text{if } t_i \in \Delta t_l, \\ 0, & \text{otherwise.} \end{cases} \tag{2.39}$$

Thus the mean time of flight can be estimated as

$$\langle t \rangle \approx \bar{t} = \frac{\frac{1}{N}\sum_{i=1}^{N} t_i w_i}{\bar{R}_{tot}} = \frac{\sum_{i=0}^{N} t_i w_i}{\sum_{i=0}^{N} w_i} \tag{2.40}$$

The sample variance associated with the calculated value of $\bar{t}$ is

$$var[\bar{t}] = \frac{1}{N}\Big(\frac{1}{N}\frac{\sum_{i=1}^{N} t_i^2 w_i}{\sum_{i=1}^{N} w_i} - [\bar{t}]^2\Big) = \frac{1}{N}s_t^2 \approx \frac{1}{N}\sigma_t^2 \tag{2.41}$$

where s_t^2 is the variance of the time of flight of the photons collected at the top surface.

To decide whether tMC and sMC$_p$ are statistically equivalent we developed a hypothesis testing procedure for these quantities. The population of interest is the set of photon biographies generated through the two simulation methods. For all the optical properties under investigation we generate the samples X_{tMC} and X_{sMC_p} with 10^8 photon biographies. Using these databases we tested the hypothesis

$$\begin{aligned} H_0 &: \mu_{\text{tMC}} = \mu_{\text{sMC}_p} \\ H_1 &: \mu_{\text{tMC}} \neq \mu_{\text{sMC}_p} \end{aligned} \tag{2.42}$$

where $\mu = R, \langle t \rangle, \langle r \rangle$. Even if all of the distributions under investigation (weights, times and radial positions) are ill behaved, i.e. very far from a normal distribution, the difference between the mean of two samples is approximately normal if the sample size is so large that the conditions of the Central Limit Theorem apply [29]. Under this condition we can assume that if the tMC and the sMC approaches are equivalent the difference between the sample mean $\bar{X}_{\text{tMC}}$ and $\bar{X}_{\text{sMC}_p}$, with $(\bar{X} = \bar{R}_{tot}, \bar{t}, \bar{r})$, is well approximated by a t statistic [29]. To be more sensitive to possible discrepancies between the two models we did not assume *a priori* that $\sigma^2_{\text{tMC}} = \sigma^2_{\text{sMC}_p}$, so we used the statistic

$$t_0^* = \frac{\bar{X}_{\text{tMC}} - \bar{X}_{\text{sMC}_p}}{\sqrt{\frac{s^2_{\text{tMC}}}{N} + \frac{s^2_{\text{sMC}_p}}{N}}} \tag{2.43}$$

which approximately follows a t-Distribution with ν degrees of freedom

$$\nu = \frac{\left(\frac{s^2_{\text{tMC}}}{N} + \frac{s^2_{\text{sMC}_p}}{N}\right)^2}{\frac{(s^2_{\text{tMC}}/N)^2}{N+1} + \frac{(s^2_{\text{sMC}_p}/N)^2}{N+1}} - 2 \tag{2.44}$$

To decide whether to reject or not the null hypothesis H_0 we compute the statistic with a level of significance $\alpha = 0.05$. This leads to the definition of the corresponding 95% confidence interval (CI). If the difference of the measured sample means falls within this interval, i.e. the measured p-value is larger than α, we fail to reject H_0, whereas if the p-value is less than or equal to α we would reject the hypothesis that tMC and sMC are equivalent.

Statistical Analysis Results

We start by considering the metrics identified in the previous section to characterize the reflectance signal generated through a Monte Carlo simulation. The objective here is to determine if the sMC$_p$ method provides equivalent results as compared to the tMC method and its range of applicability. Using both tMC and sMC$_p$ methods we generated a dataset of photons biographies for fifteen different combinations of optical properties, where $\mu_a \in [0.001 - 0.3]$ mm^{-1} and $\mu_s' \in [0.5 - 2.0]$ mm $^{-1}$. We followed the process explained in Section (2.3) to test the hypothesis of equivalence between the two approaches.

The results obtained for the reflectance are showed in Table (2.1). Both the measured value of $\bar{R}_{tot}$ and the standard deviation, s_R, have a relative difference smaller the 1% when calculated with the two approaches. The null hypothesis $H_0 : R_{\text{tMC}} = R_{sMC_p}$ can never be rejected as the p-value is always larger then 0.05. The 95% confidence interval is always very narrow meaning that the equivalence between the two methods is verified from both statistical and practical points.

The radial and the temporal distribution of the reflected photons have been compared in terms of their first moments. The results are shown in Tables 2.2 and 2.3. The absolute differences of the measured first moments are always smaller than 0.007 mm and 0.2 ps, respectively. The standard deviation of the two populations also shows very good agreement. Both the hypothesis $H_0 : \langle r \rangle_{\text{tMC}} = \langle r \rangle_{\text{sMC}_p}$ and $H_0 : \langle t \rangle_{\text{tMC}} = \langle t \rangle_{\text{sMC}_p}$ are never rejected as the p-value is always larger

then the chosen level of significance. The respective confidence interval are always smaller then 0.01 mm and 0.3 ps.

Table 2.1: Statistical analysis of the measured reflectance using tMC or sMC_p.

μ_a **[mm^{-1}]**	μ_s' **[mm^{-1}]**	$R_{\mathbf{tMC}}$	$R_{\mathbf{sMC}_p}$	$s_{\mathbf{tMC}}$	$s_{\mathbf{sMC}_p}$	p**-value**	**CI** $\cdot 10^3$
0.001	0.5	0.77938	0.77942	0.29456	0.29455	0.399	0.163
0.001	0.7	0.80577	0.80580	0.27863	0.27861	0.454	0.154
0.001	1.0	0.83032	0.83031	0.26144	0.26146	0.700	0.145
0.001	1.2	0.84154	0.84155	0.25270	0.25270	0.763	0.140
0.001	1.5	0.85425	0.85422	0.24204	0.24206	0.464	0.134
0.001	2.0	0.86889	0.86891	0.22858	0.22857	0.617	0.127
0.010	1.0	0.60386	0.60384	0.35417	0.35417	0.687	0.196
0.030	1.0	0.44117	0.44115	0.35700	0.35700	0.658	0.198
0.100	0.5	0.16079	0.16080	0.24903	0.24903	0.768	0.138
0.100	0.7	0.20338	0.20343	0.27692	0.27694	0.236	0.154
0.100	1.0	0.25350	0.25348	0.30345	0.30344	0.643	0.168
0.100	1.2	0.28060	0.28059	0.31537	0.31537	0.785	0.175
0.100	1.5	0.31484	0.31481	0.32826	0.32824	0.468	0.182
0.100	2.0	0.36005	0.36003	0.34179	0.34179	0.757	0.189
0.300	1.0	0.11659	0.11658	0.21348	0.21349	0.757	0.118

Table 2.2: Statistical analysis of the first moment of the radial distribution of tMC and sMC$_p$.

μ_a[mm^{-1}]	μ_s'[mm^{-1}]	r_{tMC}[mm]	r_{sMC_p}[mm]	s_{tMC}[mm]	s_{sMC_p}[mm]	p-value	CI $\cdot 10^3$[mm]
0.001	0.5	10.838	10.837	12.801	12.797	0.463	7.0952
0.001	0.7	8.277	8.275	10.169	10.166	0.195	5.6364
0.001	1.0	6.199	6.200	7.957	7.955	0.607	4.4106
0.001	1.2	5.344	5.344	7.016	7.015	0.476	3.8890
0.001	1.5	4.450	4.451	6.012	6.011	0.683	3.3326
0.001	2.0	3.511	3.510	4.925	4.923	0.338	2.7298
0.010	1.0	3.773	3.774	3.788	3.788	0.222	2.1000
0.030	1.0	2.797	2.798	2.599	2.599	0.147	1.4406
0.100	0.5	2.776	2.776	2.498	2.498	0.912	1.3850
0.100	0.7	2.305	2.305	2.060	2.059	0.333	1.1416
0.100	1.0	1.863	1.864	1.664	1.664	0.198	0.9224
0.100	1.2	1.664	1.664	1.489	1.489	0.178	0.8253
0.100	1.5	1.442	1.442	1.296	1.296	0.623	0.7186
0.100	2.0	1.192	1.192	1.082	1.082	0.915	0.5996
0.300	1.0	1.132	1.132	1.037	1.038	0.868	0.5751

Table 2.3: Statistical analysis of the first moment of the temporal distribution of tMC and sMC$_p$.

μ_a[mm^{-1}]	μ_s'[mm^{-1}]	t_{tMC}[ns]	t_{sMC_p}[ns]	s_{tMC}[ns]	s_{sMC_p}[ns]	p-value	CI $\cdot 10^3$[ns]
0.001	0.5	0.49976	0.49963	1.11281	1.11266	0.393	0.2123
0.001	0.7	0.42640	0.42633	1.02392	1.02378	0.617	0.1953
0.001	1.0	0.35981	0.35982	0.93703	0.93711	0.939	0.1788
0.001	1.2	0.32983	0.32978	0.89570	0.89563	0.690	0.1709
0.001	1.5	0.29620	0.29627	0.84722	0.84730	0.524	0.1616
0.001	2.0	0.25796	0.25789	0.78890	0.78875	0.527	0.1505
0.010	1.0	0.10419	0.10420	0.16480	0.16481	0.754	0.0314
0.030	1.0	0.05565	0.05565	0.07116	0.07116	0.832	0.0136
0.100	0.5	0.03459	0.03459	0.03258	0.03259	0.319	0.0062
0.100	0.7	0.03073	0.03073	0.03028	0.03028	0.611	0.0058
0.100	1.0	0.02693	0.02694	0.02800	0.02800	0.685	0.0053
0.100	1.2	0.02513	0.02513	0.02689	0.02690	0.726	0.0051
0.100	1.5	0.02305	0.02305	0.02559	0.02559	0.342	0.0049
0.100	2.0	0.02056	0.02057	0.02399	0.02399	0.593	0.0046
0.300	1.0	0.01318	0.01318	0.01186	0.01187	0.494	0.0023

2.4 Single Monte Carlo Implementation

Monte Carlo simulation itself is a meshless computation, however a mesh is needed to extract information from the simulation output. For example to obtain the space and time resolved reflectance, $R(r,t)|_{z=0}$, at a given location (r_0, t_0) it is necessary to integrate the radiance over the whole upper pointing hemisphere, S^{2-} and over the spatial and temporal interval covered by the bin where the photons are collected.

The sMC equations (Eqs. (2.3) and (2.4)) can potentially be used to derive the value of the reflectance for any couple of optical properties, μ_a and μ_s. As the reference reflectance is defined over a finite set of spatial and temporal bin one needs to interpolate these native points in order to evaluate $R(r,t)$ continuously.

The binning method and the interpolation technique have a very strong impact on the accuracy of the sMC$_i$ results. The goal is to obtain a net of nominal values that covers a wide physical range over the temporal and over the spatial dimension as this allows for large scattering variations. These native point should be as accurate as possible and they should capture the dynamic of the reflectance signal which exhibits a very sharp and quick dynamic for smaller source detector separations and for shorter times and a smoother and slower dynamic for the longer distances and for the larger times.

While trying to achieve the accuracy requirements, it is desirable to maintain the solver as 'light' as possible, thus the number of native points should be small enough to reduce the storage size and the computing effort of the solver.

Binning

When the output of a MC simulation is processed to obtain the radial and temporal resolved reflectance, i.e. the probability that a photon has to be emitted from the top surface at a time t and at a distance r from the injection point, the weights of the detected photons need to be tallied in a set of radial and time bins each of finite width.

For each photon that escapes the $z = 0$ surface at a radial position r_i after a time of flight t_i a tally of w_i is added to the reflectance $R(r_k, t_l)$ where k is the index associated with the radial ring that contains r_i and l is the index for a time interval that includes t_i.

This binning process is necessary to obtain $R(r_k, t_l)$ using either tMC or sMC$_p$ approaches. For the sMC$_i$ approach the binning process is invoked at a previous stage, when the reference simulation is binned to obtain the nominal values $R(r_k, t_l)$ which are processed to calculate $R_r(r,t)$ as illustrated in the flowchart in Fig 2.2.

The standard deviation associated with the reflectance values should be at least an order of magnitude smaller then the reflectance values. This is relevant for the construction of the reference signal used for sMC$_i$ to obtain accurate nominal values over a wide physical domain.

It is clear that the binning process plays a critical role for the analysis carried on for this work as it introduces discretization errors that will strongly affect the results. Three different discretization techniques have been examined during this work.

The first one is commonly defined as equal width discretization (EWD) [30] and is based on the subdivision of the physical range into $m_r \times m_t$ bins of constant size. This binning strategy is the most commonly adopted for the evaluation of the reflectance signal from the output of a MC simulation [23]. A slight variation often presented in the literature consist in the use of different sets of uniform bins [1]. This alternative has not been considered in this work.

The second approach, often referred to as equal frequency discretization (EFD) [31], divides the sorted values into $m_r \times m_t$ intervals so that each interval contains approximately the same number of training instances. Instead of fixing the boundary of the bins *a priori*, these are dynamically built based on the radial and the temporal cumulative distribution function (CDF) of the collected photons. Thus each interval contains $N_{out}/(m_r \times m_t)$ (possibly duplicated) photons with adjacent values of radial distance and time of flight, where N_{out} is the number of photons that were not terminated during the simulation. This binning process requires a sorting of the photon database according to the radial position

Since the number of photons that needs to be sorted is very large ($\simeq 10^8$) and since the run-time required for the sorting operation has a order of growth $O(n \log_2 n)$ this operation was not carried out using MATLAB, as the rest of the analysis. Rather the output of the MC simulation was sorted using a program developed in standard C, based on the *qsort* algorithm.

Once the number of radial bins m_r is chosen it is possible to calculate the bin limits that give a radial CFD with a constant number of photons, N/m_r, collected in each radial interval. The lower and upper limit of the radial interval are defined by the radial coordinate of the first and last photon tallied in each bin. In general, the division of N total photons by m_r intervals has some left over photons, m. This remainder is handled considering one extra photon for all the fist m intervals. Figure 2.3 shows an example of CFD calculated from the photon database generated with a tMC simulation.

Once the radial bins have been calculated the same approach is used to evaluate the temporal bins for each spatial interval. This means that for each subset of photons, which has been collected within the same spatial interval, we sort them according to their time of flight and we divide them by the number of temporal intervals, m_t. After handling the remainder photons with the same approach used for the radial subdivision, we find the bin limits that lead to a temporal CDF with a constant number of photons in each temporal interval. The time bins limits are set according to the value of time of flight of the first and last photon of each subsubdivision. Figure 2.4 shows an example of the temporal CFD obtained for different radial distances.

For the construction of the reference reflectance used for the sMC_i we developed a binning method based on an adaptive discretization (AD) algorithm. The number of bins in this case is not imposed *a priori* and the bin limits are dynamically built trying to satisfy the following set of conditions that we imposed: (*i*) the number of photons collected within each radial bin has to be at least $n_r = 5 \cdot 10^5$; (*ii*) the number of photons collected in each time bin, $n_t(r)$, increases as a function of the radial distance going from 2500 to 5000; (*iii*) the distance between two adjacent radial bins has to satisfy the condition $r_{k+1} - r_k \leq \Delta r_{max} = 0.2$ mm; (*iv*) the distance between two adjacent bins along the time dimension has to satisfy $t_{l+1} - r_l \leq \Delta t_{max} = 0.02$ ns; (*v*) the relative difference between two adjacent reflectance values along the temporal dimension has to satisfy $(R_{k+1} - R_k)/R_k \leq \Delta R_{rel,max} = 0.1$.

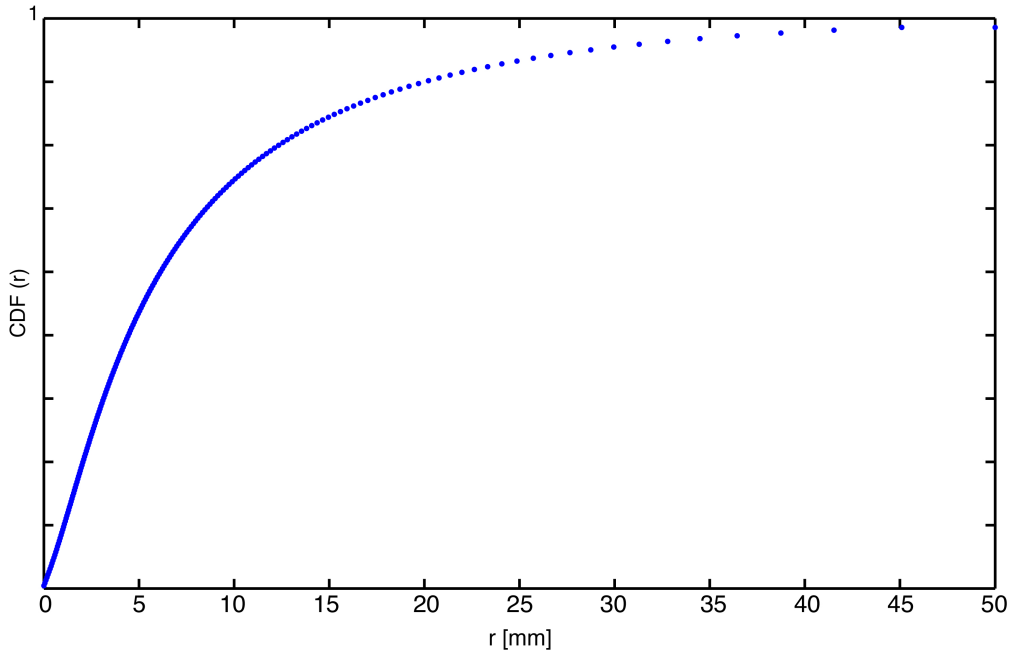

Figure 2.3: Example of the radial CDF obtained using EFD on the output of a tMC simulation.

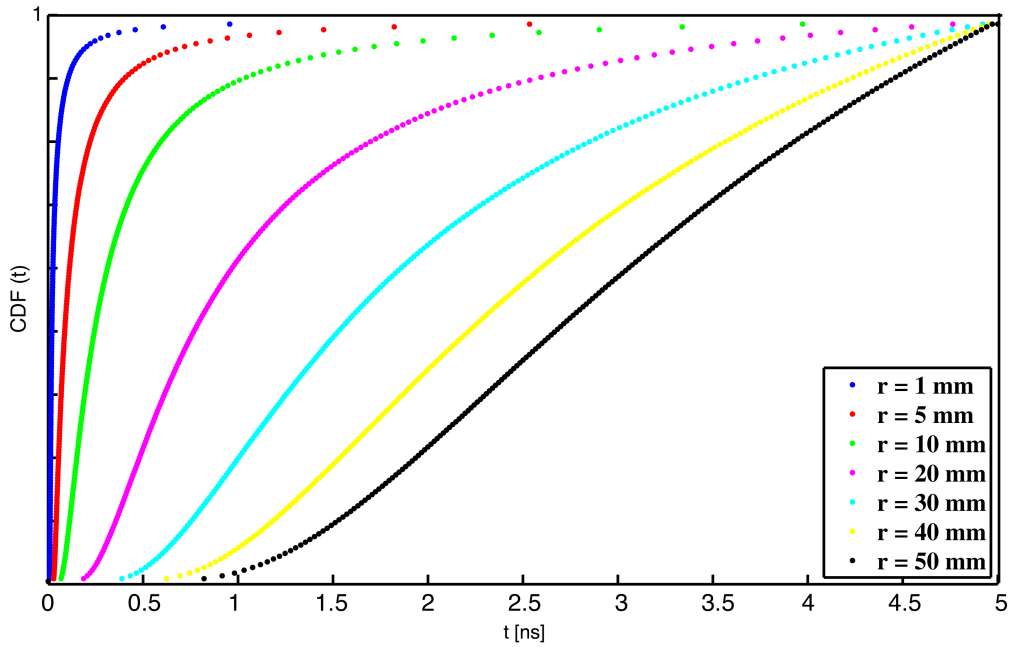

Figure 2.4: Example of the temporal CDF for different radial bins obtained using EFD on the output of a tMC simulation.

We develop this model to overcome the weaknesses of the previous binning approaches. Specifically, both EFD and EWD are referred as parametric binning techniques because the number of bins is determined *a priori* by the user without any reference to the properties of the training data. EWD makes no use of any information held in the collected data at all, and the variance of the measured values in those bins where a small number of photons is collected becomes too large. EFD is slightly better because the number of bins is predefined but their location is determined by the distribution of the measured data and each bin contains nearly the same amount of photons. In this case, when a large number of photons is collected in each bin, the sampled nominal values may be 'too far' from each other thus causing large inaccuracies in the interpolation.

Other values for the parameters n_r, $n_t(r)$, Δr_{max}, Δt_{max} and ΔR_{min} use to obtain the reference signal have been tested. The values chosen are those that gave the smaller variance for the measured values of $R(r_k, t_l)$ and reduced the noisy trend without loosing the sharp features of the reflectance signal.

The flowchart in Fig. 2.5 shows the logic of the algorithm developed to discretize the data along the radial dimension. The first step consists of sorting all the photon biographies generated with the reference simulation, according to the radial exit position. The first n_r photons are tallied in the first radial bin, which is represented by the mean of the radial position, r_1, (Fig. 2.6a) of the photons collected within its boundaries $r_{min} = r_f$ and $r_{max} = r_l$, where f and l are the indexes of the first and of the last processed photon.

This sub set of photons is fed to the algorithm that discretizes the data along the temporal dimension computing $R(r_1, t_l)$ (Fig. 2.7). Once the first iteration is completed it is possible to analyze the second subset of n_r photons. After calculating the nominal radial position of the second spatial bin, condition (iii) is checked. If not satisfied a windowing process is activated: the index of the first photon, f, is reduced by a factor of 0.25. This process is iterated until $r_2 - r_1 \leq \Delta r_{max}$ or until the difference between the index of the first photon in the two adjacent radial bins, $f_2 - f_1$, would be smaller then $5 \cdot 10^4$. The effect of this process is schematically illustrated in Figs. 2.6b and 2.6c. The last reflectance curve $R(r_{last}, t_l)$ is excluded if condition (i) is not valid.

The flowchart in Fig. 2.7 shows the algorithm that processes the sub sets of photons, collected within each radial bin, used to discretize the data along the temporal dimension and to compute $R(r_k = \text{const}, t_l)$. After sorting the time of flight, the first n_t photons are tallied in a bin represented by the mean, t_1, of the time of flight of the photons collected between $t_{min} = t_f$ and $t_{max} = t_l$, where f and l are the indexes of the first and of the last processed photon (Fig. 2.8a). After having defined the boundaries of the first bin, $R(r_k, t_1)$ is calculated. Conditions (iii), (iv) and (v) are not verified for the first bin.

When the next n_t photons are processed, the nominal value that represents the bin, t_2, is evaluated as the average of the times of the collected photons. Before calculating the reflectance, $R(r_k, t_2)$, condition (iv) is checked as illustrated in Fig. 2.8b. If $t_2 - t_1 \leq \Delta t_{max}$ the value $R(r_k, t_2)$ is computed. Otherwise the same windowing method used for the radial discretization is applied (Fig. 2.8c). This process is repeated until condition (iv) is satisfied or until the windowing would lead to a difference in the index of the first photon collected in two adjacent bins smaller then 100 units.

Once the time bin has been defined, $R(r_k, t_2)$ is calculated and condition (v) is checked (Fig. 2.9a). The same windowing process is applied to obtain reflectance values with relative variations smaller

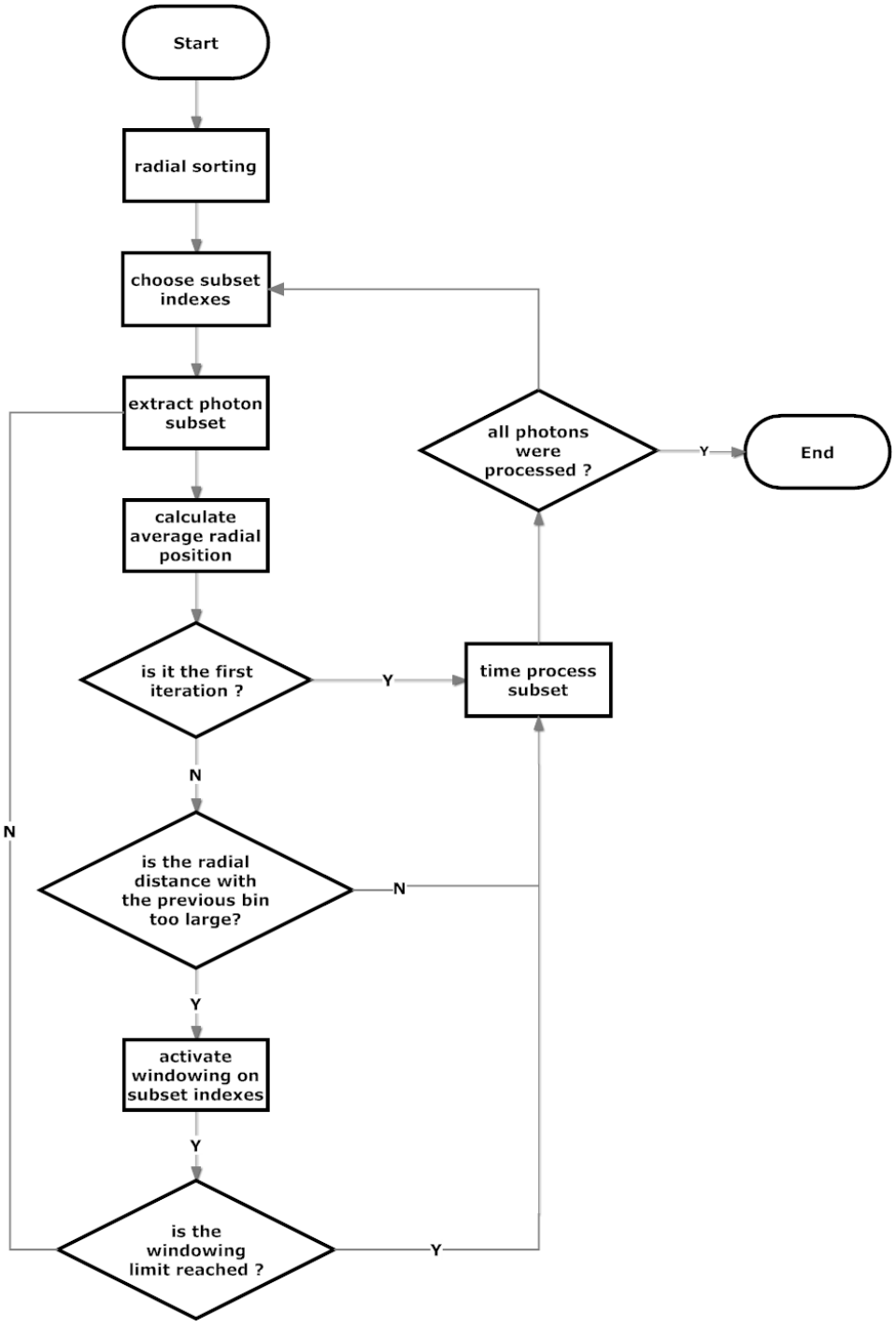

Figure 2.5: Flowchart of the adaptive discretization along the radial dimension.

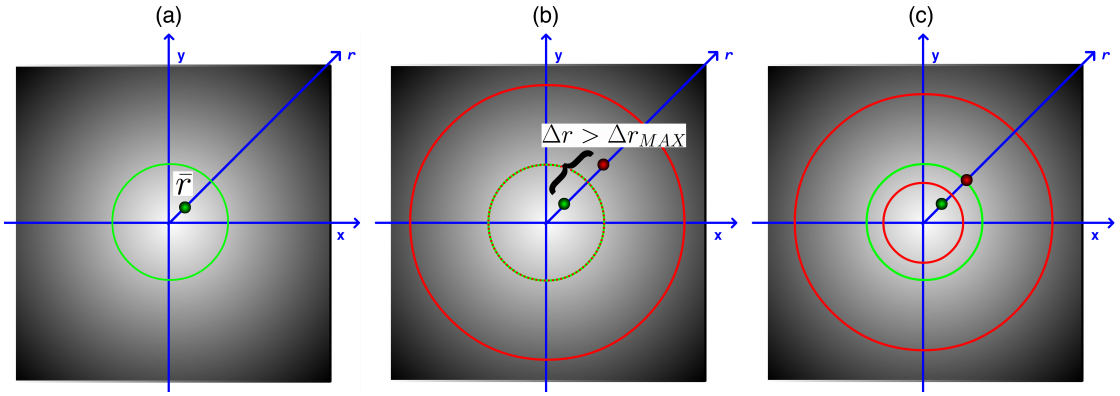

Figure 2.6: Adaptive discretization along the radial dimension: (a) representation of the first radial bin; (b) representation of the second radial bin and comparison of the distance between the two nominal positions with the imposed Δr_{MAX}; (c) windowing mechanism activated if $\Delta r > \Delta r_{MAX}$

then 10% (Fig. 2.9b). It is important to note that the windowing due to condition (iv) was activated only on the tail of the curve while the windowing to reduce the relative difference between adjacent reflectance values was activated only on the rise of the curve.

After that all the sub set has been processed the last value of $R(r_k = \text{const}, t_l)$ is discarded if condition (ii) is not satisfied, as shown in Fig. 2.10. One should note that condition (v) is not imposed along the radial dimension. This is because the time locations where the reflectance is calculated are different from one radial bin to another as a result of the AD technique. Above that the trend of the reflectance curves for fixed time along the radial dimension have slower variations and are monotonically decreasing.
Once the entire photon dataset is processed and discretized along the radial and the temporal dimensions the nominal values of the reflectance, $R(r_k, t_l)$, are stored.

Independently from the binning mechanism, the representation of all the photons collected within a bin with the nominal coordinates (r_k, t_l) introduces a discretization error. Typically each bin is represented by its middle points. To reduce this error we decided to use the mean of the radial position and the mean time of flight of all the photons collected within each bin. This error reduction has not been examined carefully but we noted that when EFD is used or when EWD with large bins is used, the use of the mid point often leads to artifacts in the measured reflectance.
Regardless of binning approach the value of the reflectance calculated over an annular bin of area ΔA_k over a time span Δt_l has been computed using Eq. (1.20) and the standard deviation of the reflectance measured in the specific bin has been calculated through Eq. (1.23).

Reference Reflectance

In principle the use of Eqs. (2.3) - (2.4) enables the calculation of $R(r, t)$ for any value of absorption and scattering coefficient. However with a MC simulation it is possible to measure the reflectance only for a discrete set of positions. As a result it is necessary to interpolate between these native points in order to calculate $R(r, t)$ for continuous values of r and t for an arbitrary set of optical

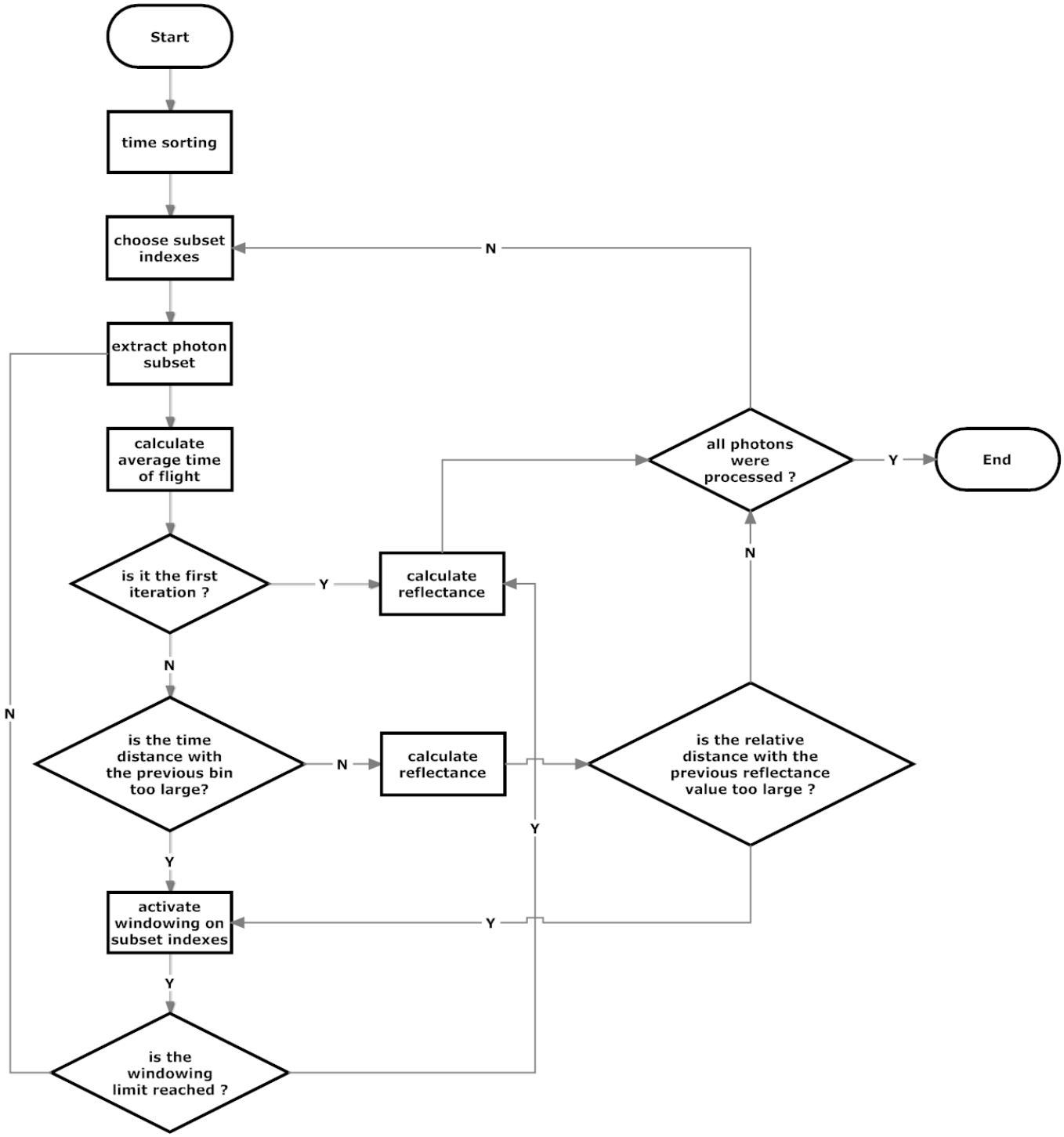

Figure 2.7: Flowchart of the adaptive discretization along the temporal dimension.

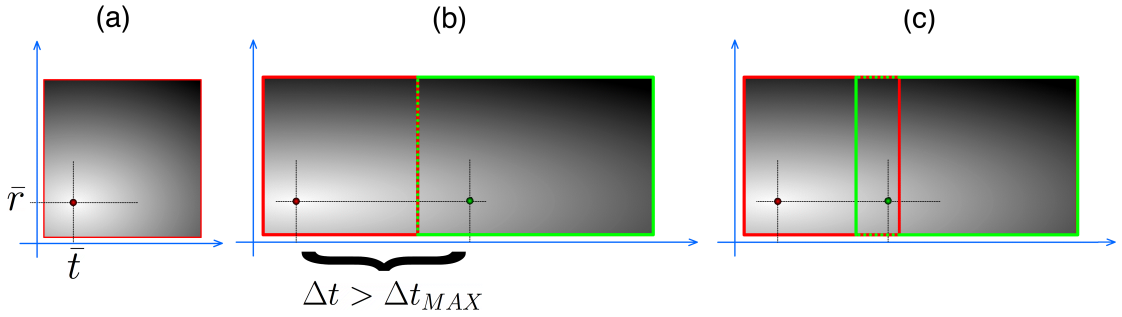

Figure 2.8: Adaptive discretization along the temporal dimension: (a) representation of the first radial bin; (b) representation of the second radial bin and comparison of the distance between the two nominal positions with the imposed Δt_{MAX}; (c) windowing mechanism activated if $\Delta t > \Delta t_{MAX}$

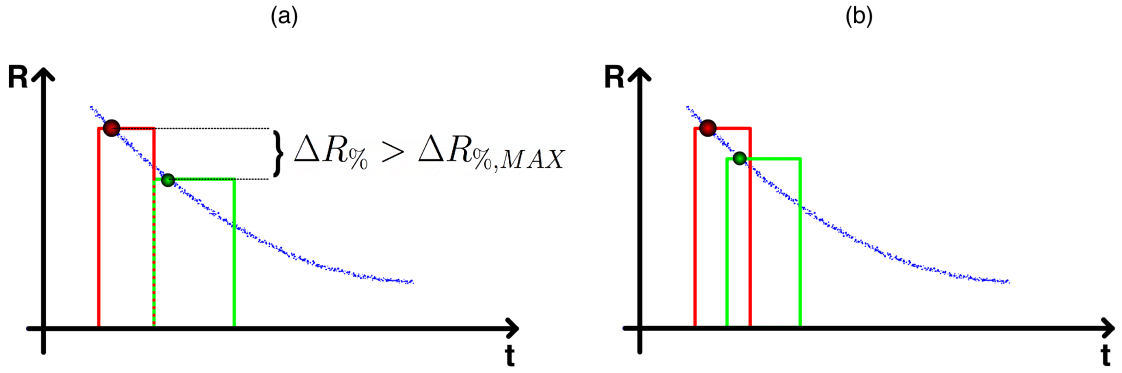

Figure 2.9: Windowing mechanism used to reduce the relative variation of the reflectance between adjacent bins

properties.

As reported by different authors [1, 22] one of the main limits of the sMC approach is the reduction of dynamic range due to the weak capability of obtaining an accurate representation of the reference reflectance for large distances and long times. These are located where the results obtained with a uniform binning of the MC output become very noisy. Typical values for the optical parameters of biological tissues in the red and near infrared spectral region set the time scale of photon migration events in the range of 1-10 ns, while the typical source detector separation used for real life measurements rarely exceeds a few centimeters. To be able to represent the reflectance signal over the physical domain of interest, even when the value of μ_s becomes very large, we tried to obtain the native set of reflectance values, $R_r(r_k, t_l)$ over a time range from 0 to 20 ns and over a spatial range from 0 to 100 mm.

First of all the adaptive binning technique previously described was used to bin the output of the reference simulation. Since the number of the reflectance values and their temporal locations are different for every radial bin, we resampled each reflectance curve $R(r_k = \text{constant}, t_l)$ in a uniform time vector, T. These time points have been chosen in a way that reflected the cumulative distribution function of all the photons, using a decreasing density of sampled points per unit time in the range [0-20] ns.

The AD approach showed one limitation due to the drop in the number of photons that are collected at late times. For this reason the last valid value $R(r_k, t_{last})$ is situated at a time location shorter then 20 ns for radial distances $r_k < 15$ mm. We tried to use different binning approaches and extrapolation methods to obtain nominal values for these spatial and temporal range. The approach that gave the most satisfying results was to define a set of bins of width 0.1 ns from the last valid time location to 20 ns. For each radial bin that exhibited this problem, the photons collected within its limits were tallied in these bins and each bin was represented by the average of the times of the photons collected within its boundaries. The variance associated with the new set of discrete points was still too large to use them directly for the creation of the reference surface, so on the tail of the curves we fitted a non linear function, $f_t(t)$, with three free parameters (a, b, c)

$$f_t(t) = \frac{a}{t^{3/2}}\left[\exp\left(-\frac{b}{t}\right) - \exp\left(-\frac{c}{t}\right)\right] \tag{2.45}$$

which has the form of a source-image Green's function without absorption decay. Even though the approach is based on diffusion approximation, the general functional form fits the data very well most likely because the photons collected at these distances after a 'long' time have undergone a very large number of collisions. Figure 2.10 shows the result of this approach for a source detector separation of 1 mm.

To improve the accuracy of the representation of the rise of the reflectance signal we extrapolated extra points even for all the curves for the earlier times. For every radial bin we recorded the time of the first photon t_0. The time span from t_0 to the representative position of the first bin, t_1, was split into ten uniform bins where the photons where tallied. This provided the time coordinate for each bin, given by the mean of the time of flights of the photons collected within its boundaries, and the correspondent reflectance value. The points sampled with this method generally had a very large uncertainty so we did not use them directly for the construction of the reference surface, but we

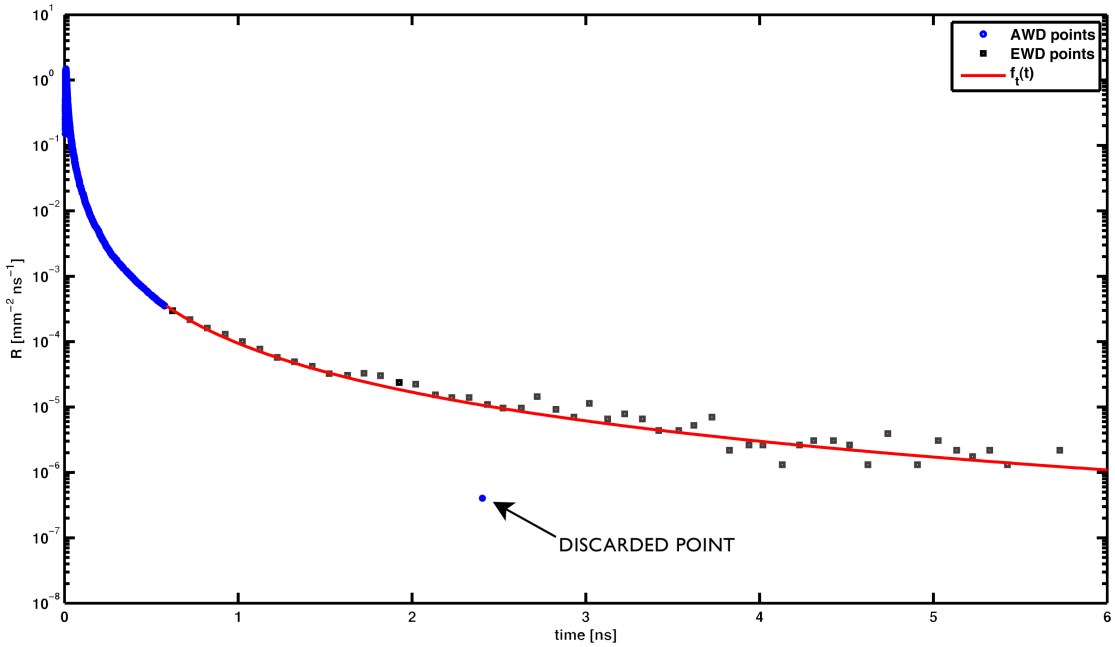

Figure 2.10: Results of the fitting approach used to extrapolate points on the tail of the curve for $r_k = 1$ mm .

tried different fitting approaches. The best results were obtained fitting the $\log_{10}$ of the measured discrete values on the rise of the curve with a third degree polynomial function, $f_r(t)$. For each radial bin this polynomial expression was used to extrapolate values for the points of T between the time of the first collected photon, t_0, and the time of the first reflectance value obtained with the binning process, t_1. The results obtained for a radial distance increasing from 1 to 10 mm are shown in figure 2.11.

To resample the reflectance curves at the temporal locations specified by T, the least square approximating 3-rd degree Non Uniform Rational B-splines (NURBS) curve was calculated for each curve $R(r_k = \text{constant}, t_l)$. This approximation smoothed the oscillations due to the statistical noise caused by the stochastic nature of the MC method, as one can see comparing Fig. 2.11 with Fig. 2.12. After calculating the approximating NURBS curve we resampled it to obtain $R_r(r_k = \text{constant}, t_l)$. The values of $R_r(r_k, t_l)$ obtained after resampling are shown in Fig. 2.12 for radial distances spanning from 5 to 100 mm.

Using this approach we obtained a set of (436×826) nominal values that covered the range $r \in [0, 100]$ mm and $t \in [0, 20]$ ns.
The reduction of the noise obtained with the resampling allowed us to use these reference points, $R_r(r_k, t_l)$ as native points for the interpolation necessary to calculate $R(r, t)$ for continuous values of r and t for an arbitrary set of optical properties using Eqs. (2.3) - (2.4).

We used a 3-rd by 3-rd degree NURBS surface to interpolate the points $R_r(r_k, t_l)$. We chose to use NURBS for their capability of representing freeform shapes using fast and stable algorithms which require an amount of information which is usually much smaller than the amount of information required

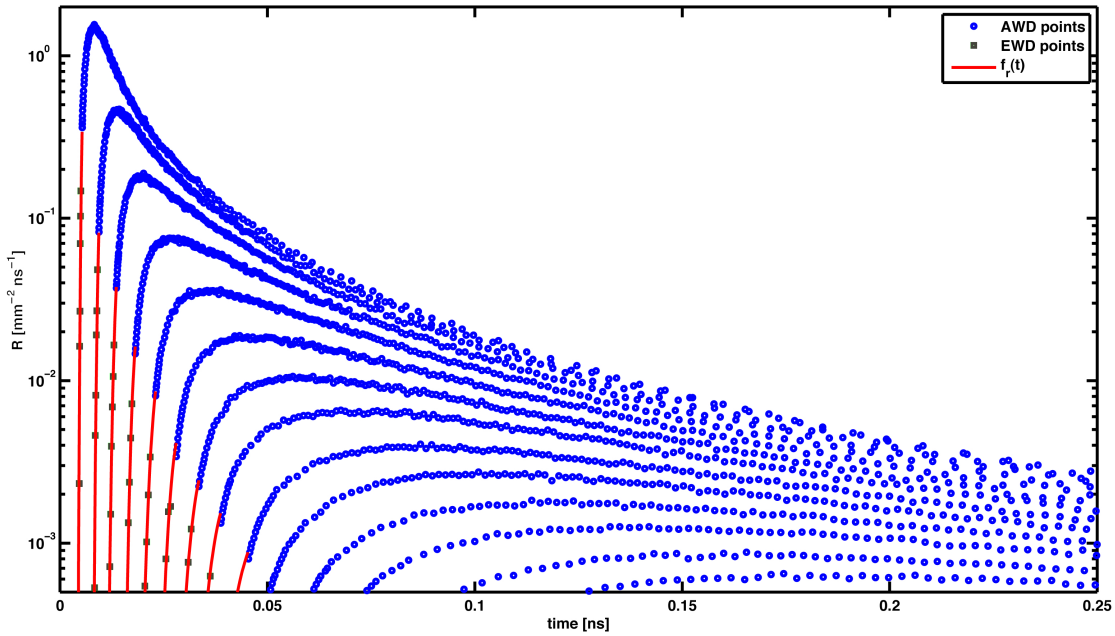

Figure 2.11: Results of the fitting approach used to extrapolate points on the rise of the curve for $r_k \in [1-10]$ mm .

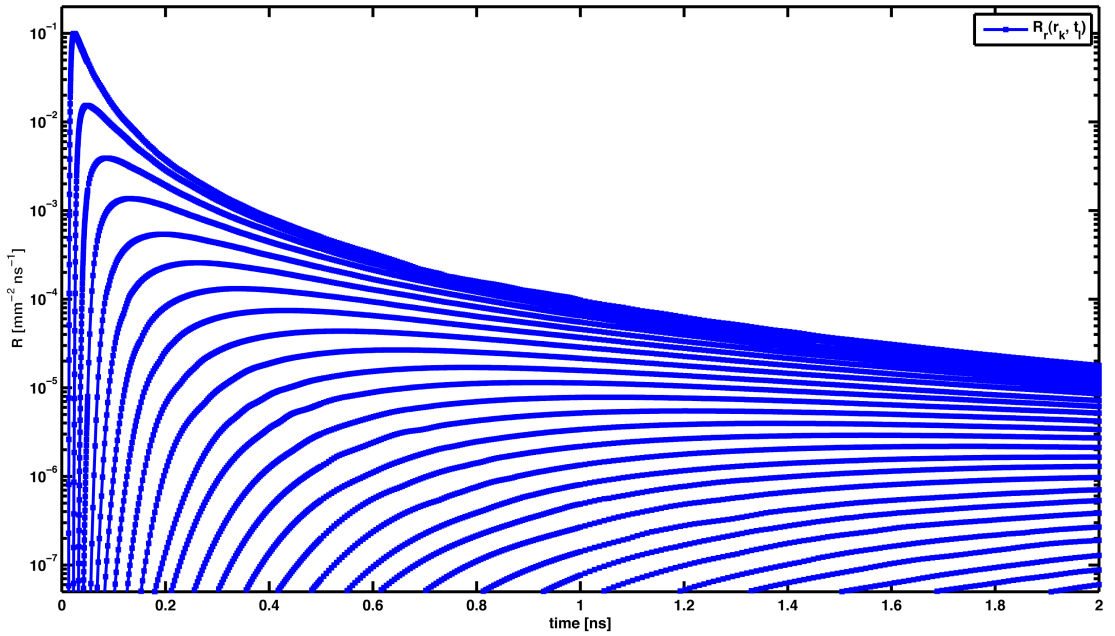

Figure 2.12: Values of $R_r(r_k, t_l)$ for $r_k \in [5-100]$ mm obtained after binning, extrapolating and resampling.

by other fitting methods. A specific NURBS fitting toolbox has been implemented for this work, it is described in appendix B. Details of the theory of NURBS curves and surfaces can be found in [32, 33].

Spatially-Resolved Reflectance

The steady state reflectance, $R(r)$, at a radial location r, is evaluated performing an analytical integration of the temporally-resolved reflectance curve, $R(r,t)$

$$\begin{aligned} R(r) &= \int_0^{t_{max}\ \mu_{s,r}/\mu_s} R(r,t)\mathrm{d}t = \int_0^{t_{max}} \frac{\mu_s^3}{\mu_{s,r}^3} R_r\left(\frac{\mu_s}{\mu_{s,r}} r, t\right) \exp(-\mu_a v t)\mathrm{d}t \\ &= \int_0^{t_{max}} \frac{\mu_s^3}{\mu_{s,r}^3} C\left(\frac{\mu_s}{\mu_{s,r}} r, t\right) \exp(-\mu_a v t)\mathrm{d}t \end{aligned} \tag{2.46}$$

where $t_{max} = 20$ ns and $C(,t)$ represents the 3-rd degree b-spline curve obtained from the interpolating surface for a constant value of the radial position.

To reduce the error given by the finiteness of the integration interval we added the integral, $\Delta R(r)$, of the temporally-resolved reflectance curve in the range $[t_{max}, \infty]$ to the calculated value of $R(r)$. The value of $\Delta R(r)$ is extrapolated as

$$\Delta R_{r_k} = \int_{t_{max}}^{\infty} \exp(-\mu_a v t) \cdot 10^{at+b} = -\frac{\exp(-\mu_a v t_{max}) \cdot 10^{(at_{max}+b)}}{a - \mu_a} \tag{2.47}$$

where a and b are the coefficients of a 1-st degree polynomial, $at + b$, obtained interpolating the log_{10} of two points on the tail of the curve, $log_{10}\left(R(0.9995 \cdot t_{max})\right)$ and $log_{10}(R(0.95 \cdot t_{max}))$. We used this approach because the reference reflectance obtained from the reference simulation exhibited a linear decay in the log_{10} space for late times.

Chapter 3

Single Monte Carlo Solver Analysis

3.1 Introduction

A common goal in the application of light transport in medicine is to determine the optical properties (OPs) of biological tissue to characterize its morphology, biochemical composition and physiological state. Knowledge of the tissue OPs, optical absorption μ_a and scattering coefficient μ_s, is desirable for different applications such as drug dosimetry, photosensitive spectroscopy, blood oximetry, brain imaging or pathological tissue detection. Various spectroscopy techniques have been extensively studied for different physical domains in order to improve the accuracy of the measurement of the optical properties of human tissues from the analysis of experimental spectroscopy data.

The relationship between the measured physical quantities such as reflectance, fluence or radiance and the OPs of the tissue under investigation is established by the RTE (Eq. (1.1)). One common approach to resolve such inverse problems is to use a radiative transport model to provide predictions for measured data based on an assumed set of optical properties. Such a model is then used in conjunction with a nonlinear optimization algorithm to determine the set of optical absorption and scattering properties that produce a radiative transport prediction that best matches the experimental data.

A model that uses OPs as input to calculate the measured physical quantities is called a forward model or forward solver. Once an appropriate forward solver is chosen, a trial and error strategy can be used to estimate the OPs. Trial OPs are repeatedly inserted into the forward model to generate values of the observed quantities until preset criteria determine that values of the calculated quantities are sufficiently close to those measured, and the resultant OPs are deemed to be the true OPs. This entire process is called the inverse model or inversion scheme.

Although a turbid medium such as tissue usually is described by three interaction parameters, the anisotropy factor g, the absorption and the scattering coefficients, it is often the case that use of two parameters, μ_a and the reduced scattering coefficient $\mu_s' = (1 - g)\ \mu_s$, are convenient and

sufficiently accurate for characterization. Therefore, the OPs that were sought for this study are the absorption and the reduced scattering coefficients.

Generally speaking, forward methods for solving the transport equation fall into two categories: analytical and numerical techniques. For methods involving analytical techniques, the observed physical quantities cannot be explicitly expressed as elementary functions of OPs except for very simple cases. Hence, various approximations are employed to simplify the mathematics of the RTE. In photon migration applications, the most commonly used radiative transport approximation is the standard diffusion model (SDA) [8, 34]. Methods involving numerical techniques include Monte Carlo (MC) simulation, the finite element method (FEM), and those borrowed from neutron transport theory such as the harmonic expansion method (PN) and the discrete ordinates method. MC is the most typically used in the photon migration framework because of its potential of representing any physical situation without any approximation. Analytical forward solvers are fast, but cannot determine the measured quantities accurately in cases where the approximations used to obtain analytical expressions fail. The appropriate use of the SDA, for example, is restricted to highly scattering media [$\mu_s'/\mu_a \geq 10$], over length scales much larger than the transport mean free path $l^* = (\mu_a + \mu_s')^{-1}$, and at locations remote from collimated sources or interfaces possessing significant refractive index, n, mismatch. Numerical methods, on the other hand, may be very accurate, but the associated computational burden often prevents their use as a forward solver for an inverse model.

Since MC has been introduced in the field of biomedical optics [6] a great deal of attention has been focused on its application as a forward model to represent photon migration within turbid media. Two paths have been followed to use MC as a forward solver for inverse problem solutions overcoming its time consuming limitations. The first one is based on the possibility of reusing the output of a MC simulation to derive the values of photometric quantities. After this idea was introduced by Graaf [35] various works [1, 18, 19, 17] stemmed from it and lead to the definition of the single Monte Carlo (sMC) [1] method. The other path followed was to try to improve the computational process associated with a MC simulation using multithreading techniques [36, 37] which increase the computing efficiency, executing multiple threads simultaneously.

In this work we focus on the use of a sMC_i based model (from now referred to as sMC only) for the evaluation of diffuse reflectance signals and for the recovery of optical properties from simulated reflectance data. Thanks to its analytical nature, the sMC model has the potential to overcome the time consuming limitations of traditional MC techniques without the need of any physical approximation. The main limitation of the sMC method based on the interpolation of a reference reflectance, is that it is valid only for infinite and semi-infinite homogeneous media. It is still important to evaluate its potential in inverse problem solution as in many applications of photon migration the goal is to measure the bulk optical properties of the tissue. Other technical limitations of the sMC technique are the discretization and interpolation errors which arise from the process used to derive the reflectance signal from a MC simulation with a limited number of photons.

First of all we analyze the performance of the sMC NURBS based forward solver (NFS) developed in the Virtual Tissue Simulator. After providing a a definition of a gold standard for $R(r,t)$ and for $R(r)$, we choose an error metric used to assert the accuracy of the model output when compared to these gold standard values.

Then we focus on the use of the NFS to measure OPs from simulated time-resolved reflectance

(TRR) signals and from steady state reflectance (SSR) signals for semi-infinite homogeneous media for both the diffusive and the non diffusive regimes. Using MC simulated data the only source of noise is the intrinsic variability of the measured values due to the stochastic nature of the MC method. In real life situations one has to deal with many other noise sources, such as the non ideality of the instrumental system which limits the accuracy of the results. However the use of simulated measured data is a proper choice when the goal of the analysis is to assert the capabilities and the accuracy of a forward solver used in an inversion problem. This is because the data is ideal, within the variability of the MC process itself and because the true optical properties are known exactly. This allows us to focus on the model and optimization capabilities in the inversion process.

3.2 Forward Solver Analysis

To validate and assert the quality of a transport model, its output is typically compared to Monte Carlo results because the photometric quantities provided by a MC simulation are commonly considered as the gold standard for photon migration in diffusive media, such as biological tissues.

To evaluate the performance of the implemented sMC model we measured its discrepancies from MC generated data. For this work we generated the gold standard values processing data that were collected using our traditional MC (tMC) program. For all the simulations we assumed constant value of anisotropy, $g = 0.8$, and constant refractive index, $n = 1.4$. The absorption coefficient spanned the range $\mu_a = [0.001 - 0.3]$ mm^{-1}, while the value of the scattering coefficient covered the range $\mu_s' = [0.5 - 2]$ mm^{-1}. The noise level of the data measured from a MC simulation depends on the number of injected photons, N. According to photon noise statistics [38] the $SNR = R/\sigma$ increases as a square law as a function of N. For this study we used $N = 10^8$ for each set of optical properties.

The number of photons that are processed is not the only feature that affects the degree if inaccuracy associated with the stochastic values generated through MC simulation. The way these data is discretized and processed has a strong impact over the standard deviation associated with each reflectance value.

3.2.1 Gold Standard Reflectance

TRR Data

The TRR gold standard values, $R_{GS}(r_k, t_l)$, were computed using Eq. (1.20). The nominal values, r_k and t_l, are evaluated as the average of the radial position and of the time of flight of the photons collected within the bin boundaries, respectively. The standard deviation of the reflectance measured in the specific bin has been calculated using Eq. (1.23). The relative standard deviation of the measured values using EFD or EWD using has been calculated as

$$\sigma_{rel}(r_k, t_l) = \frac{\sigma_{\mathrm{GS}}(r_k, t_l)}{R_{\mathrm{GS}}(r_k, t_l)} \tag{3.1}$$

We used a set of 200×200 bins to calculate the reflectance values over the range $r \in [0, 50]$ mm and $t \in [0, 5]$ ns using the two discretization approaches. For all the 15 combination of optical properties the mean of the relative standard deviation measured using EFD was smaller than 3%. Figures 3.1 , 3.2 , 3.3 show that the value of σ_{rel} is remarkably uniform over the entire domain. For larger values of the absorption coefficient, σ_{rel} increases for short distances and late times and for long distances and short times. This is because the reflectance signal is weaker in these regions and the physical span covered by the EFD bins is large in order to collect the required number of photons. The maximum value of the relative standard deviation becomes larger than 5% only for $\mu_a \geq 0.1$ mm^{-1}.

The relative standard deviation obtained with EWD is not uniform, but it increases strongly for longer times and larger distances with a mean value larger than 5% and a maximum value that reaches 100% for any combination of the optical properties. A comparison of the uncertainty obtained using the same number of bins using the two techniques may lead one to under-appreciate the improvement obtained with EFD. The uncertainty measured using a 200 x 200 set of uniform bins is smaller then the one measured with EFD over certain regions. This is because the uniform bins have radial and temporal width of Δr = 0.25 mm and Δt = 0.025 ns. Thus the amount of photons tallied within their limits is very large for short distances and short times and the statistical noise is reduced. However these bins are too large to capture the sharp peak of the reflectance signal. For a more fair comparison we used EWD with 250 radial intervals of width $\Delta r = 0.2$ mm and 1000 time bins of width Δt = 5 ps. The performance of the EWD in the far region is greatly reduced when the number of bins is increased, the mean of σ_{rel} is always larger the 15%.

Figures 3.1 , 3.2 , 3.3 show the result obtained using the three approaches for $\mu_s' = 1$ mm^{-1} and for $\mu_a = (0.001, 0.01, 0.1)$ mm^{-1} respectively. EWD is simple and suitable for various situations but it is inadequate for the relative error analysis that we wanted to develop because we have no control over the relative standard deviation associated with each bin. Even with the larger number of bins, the relative standard deviation is smaller using EWD rather then EFD for short times and small source detector separations, but it is important to note that the size of the EFD bins is smaller. The cumulative distribution functions of the time of flight shown in Fig. 2.4, for different radial bins, reveals the weakness of the uniform binning. Specifically, sampling with the same frequency events that have different temporal behaviors allow neither a capturing of the sharp dynamic of the reflectance signals nor to avoid the oscillations due to the stochastic nature of the measurement. This can be clearly seen from the examples shown in Figs. 3.4 - 3.5.

Due to the limitations of the EWD approach we chose the EFD approach to obtain the gold standard values used for the forward solver analysis. For all the combinations of optical properties the nominal values associated with each bin were stored and the sMC forward solver was used to evaluate the reflectance signal for the same locations.

SSR Data

SSR measurements consist of the determination of the reflectance signal $R(r)$, as a function of the source-detector (s-d) separation, r. In this work we considered a maximal radial distance $r_{max} = 20$ mm and the SSR gold standard values have been calculated using the same radial bins defined using EFD on the TRR data. All the photons reflected within the radial range are accounted without

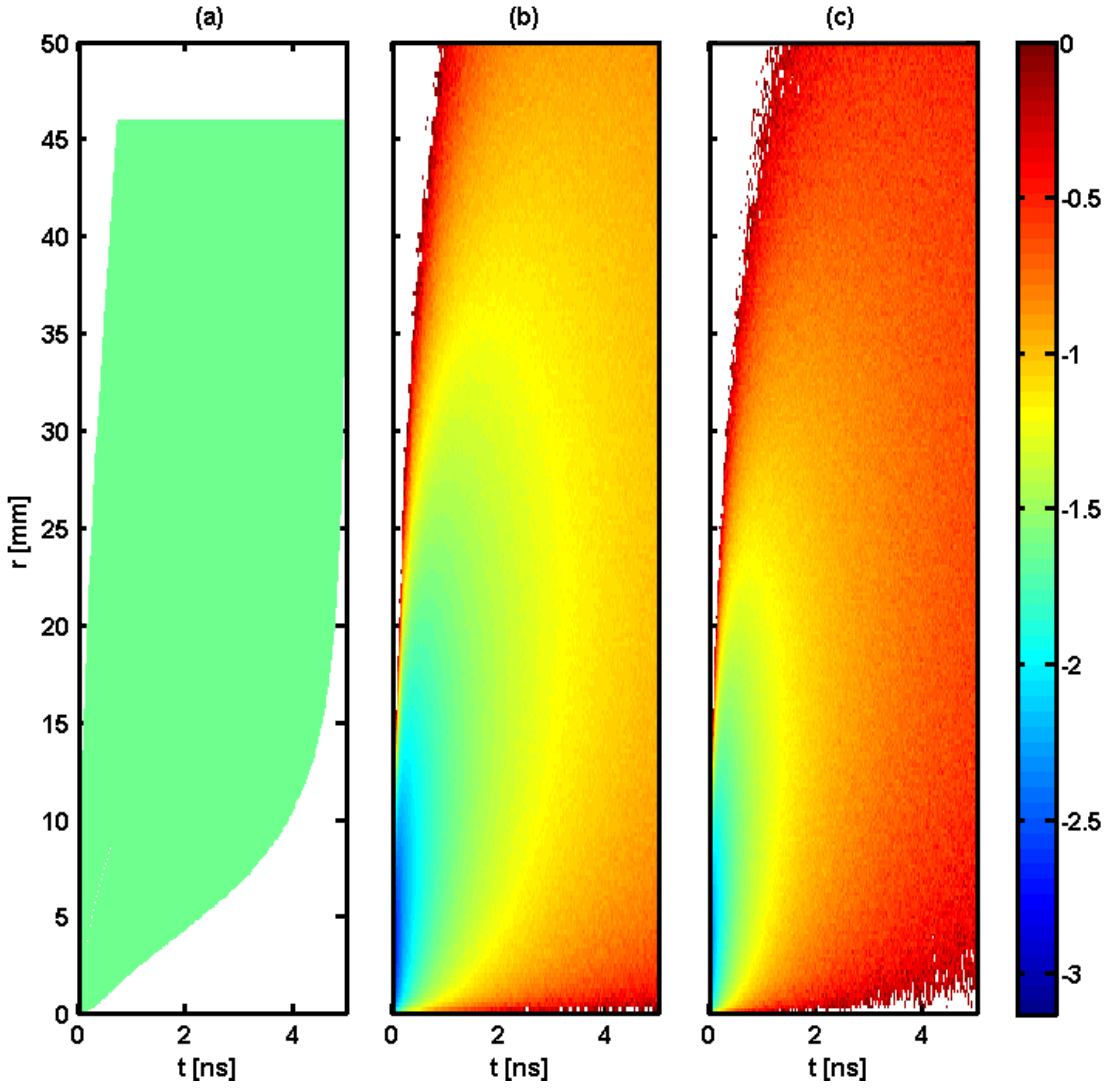

Figure 3.1: Relative standard deviation of the discretized reflectance obtained with (a) 200 x 200 EFD bins, (b) 200 x 200 EWD bins, (c) 250 x 1000 EWD bins on the output of a tMC simulation with $\mu_a = 0.001$ mm^{-1} and $\mu_s' = 1$ mm^{-1}.

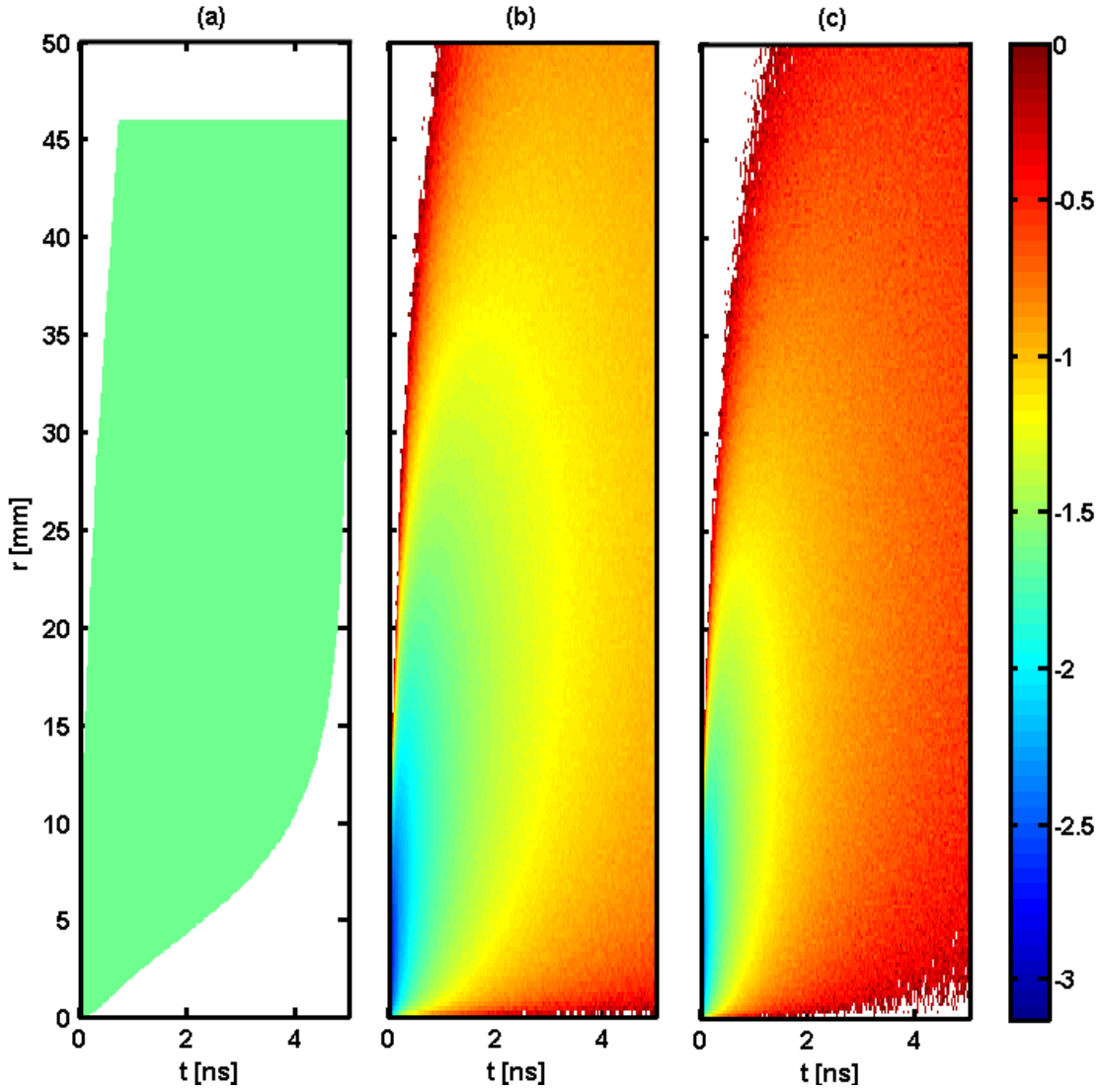

Figure 3.2: Relative standard deviation of the discretized reflectance obtained with (a) 200 x 200 EFD bins, (b) 200 x 200 EWD bins, (c) 250 x 1000 EWD bins on the output of a tMC simulation with $\mu_a = 0.01$ mm^{-1} and $\mu_s' = 1$ mm^{-1}.

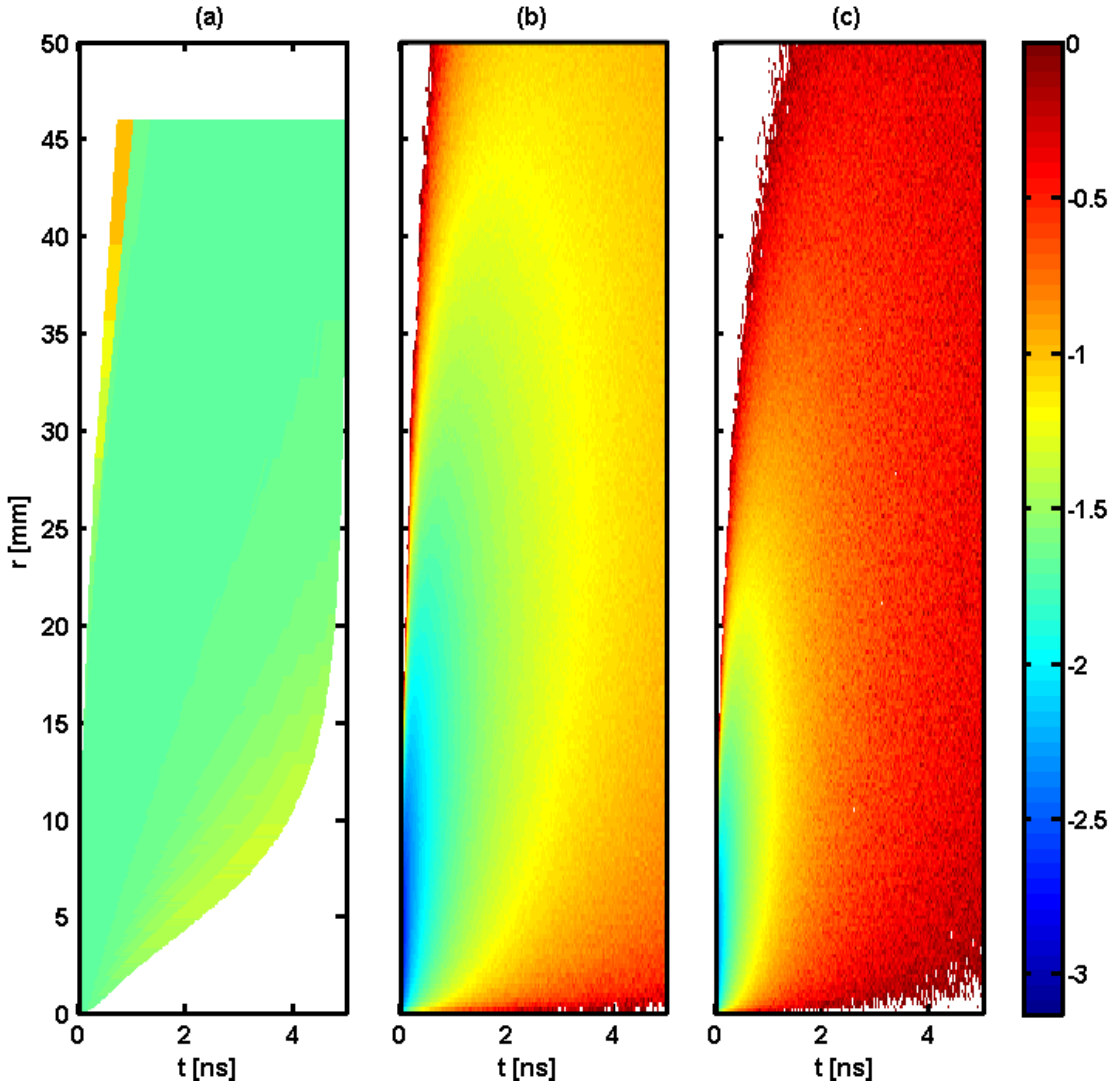

Figure 3.3: Relative standard deviation of the discretized reflectance obtained with (a) 200 x 200 EFD bins, (b) 200 x 200 EWD bins, (c) 250 x 1000 EWD bins on the output of a tMC simulation with $\mu_a = 0.1$ mm^{-1} and $\mu_s' = 1$ mm^{-1}.

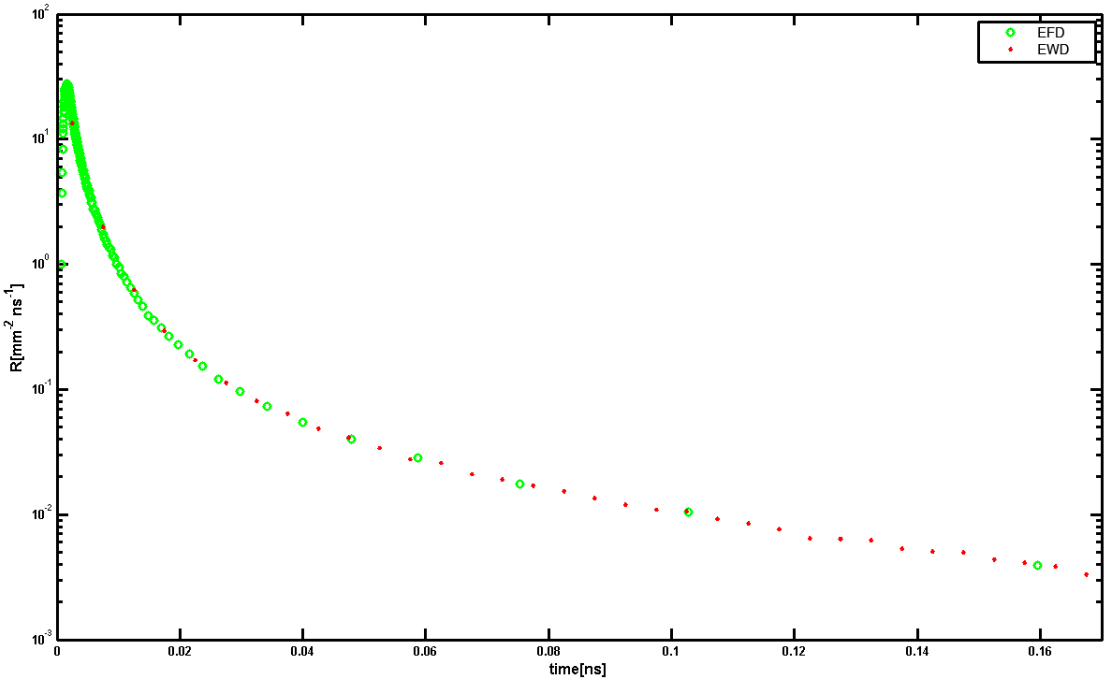

Figure 3.4: Reflectance curve at radial distance $r_k = 1$ mm obtained using EFD with 200 time bins and EWD with 1000 time bins.

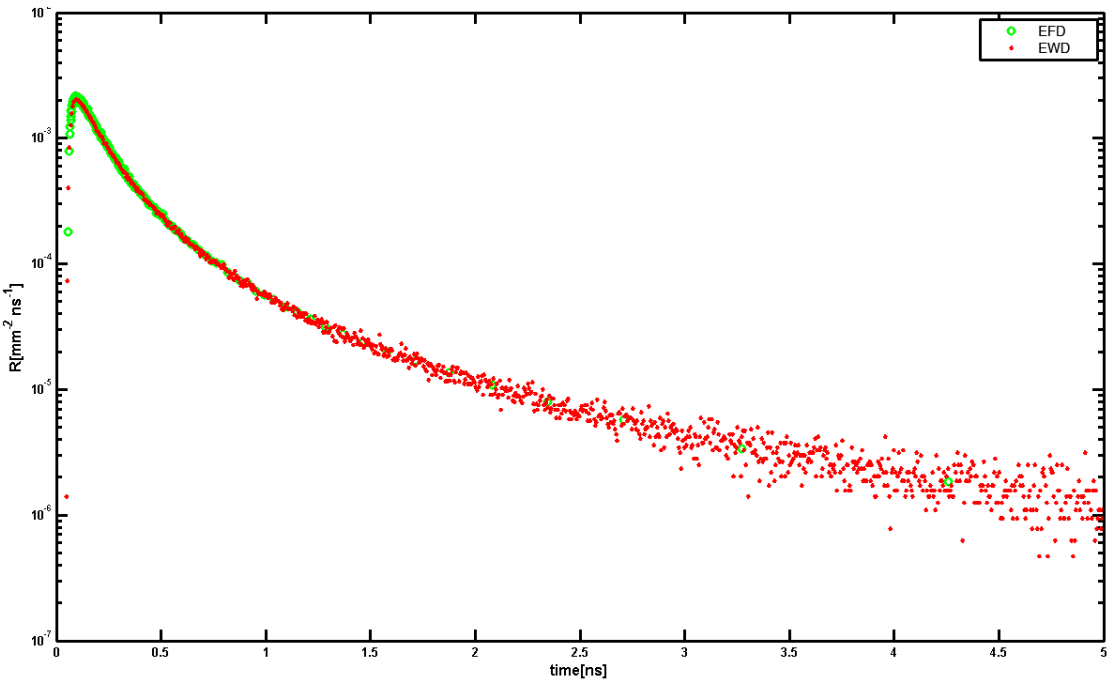

Figure 3.5: Reflectance curve at radial distance $r_k = 10$ mm obtained using EFD with 200 time bins and EWD with 1000 time bins.

performing any sort of time gating and the values of $R_{GS}(r_k)$ were calculated through Eq. (1.22). The nominal values of r_k have been evaluated as the mean of the radial positions of the photons collected within the k-th radial bin. The standard deviation of each steady state reflectance values was calculated using Eq. (1.23).

3.2.2 Error Analysis

We study the accuracy of the reflectance values obtained with the implemented sMC model in terms of the absolute and the relative error between those result and the gold standard results

$$\epsilon_{abs} = |R_{\text{GS}} - R_{\text{sMC}}| \tag{3.2}$$

$$\epsilon_{rel} = \frac{R_{\text{GS}} - R_{\text{sMC}}}{R_{\text{GS}}} \tag{3.3}$$

To calculate the relative error associated with the spatially- and temporally-resolved reflectance results we use the absolute value.

The values chosen as gold standard are stochastic in nature, so one should bear in mind the intrinsic uncertainty associated with R_{GS} when interpreting the relative error results. We calculated this uncertainty using the relative standard deviation of the measured tMC values

$$\sigma_{rel}(r_k, t_l) = \frac{\sigma_{\text{GS}}}{R_{\text{GS}}} \tag{3.4}$$

TRR Results

To calculate the relative error of the sMC approach we calculated $R_{\text{GS}}(r_k, t_l)$ using EFD with a 200 x 200 set of bins. For all the combinations of optical properties under investigation we calculated $R_{\text{sMC}}(r_k, t_l)$ for the same nominal spatial and temporal locations of the gold standard results. We used the NURBS surface obtained with the procedure explained in § 2.4 to calculate $R_{\text{sMC}}(r_k, t_l)$. First of all the linear scaling given by the scattering coefficient was imposed using Eq. (2.3), after that the impact of non zero absorption is calculated using Eq. (2.4).

Figures 3.6 to 3.12 show (a) the $\log_{10}$ of the gold standard reflectance measured from the tMC simulations, (b) the $\log_{10}$ of the of the absolute error measured using sMC, (c) the $\log_{10}$ of the relative standard deviation of the gold standard values and (d) the $\log_{10}$ of the relative error measured using sMC for different combinations of optical properties. These values are represented using colormaps as a function of the spatial coordinate, r, and of the temporal coordinate, t. The spatial and temporal range showed extends only to 20 mm and 2 ns to improve the resolution of the visualization over the region where the largest contribution of the reflectance signal is measured.

The relative error of the reflectance calculated with the sMC approach show some characteristic features. The first one is that the error measured for the first temporal bin is as large as 100% after a radial distances that depends on the optical coefficients. It is important to note that this large

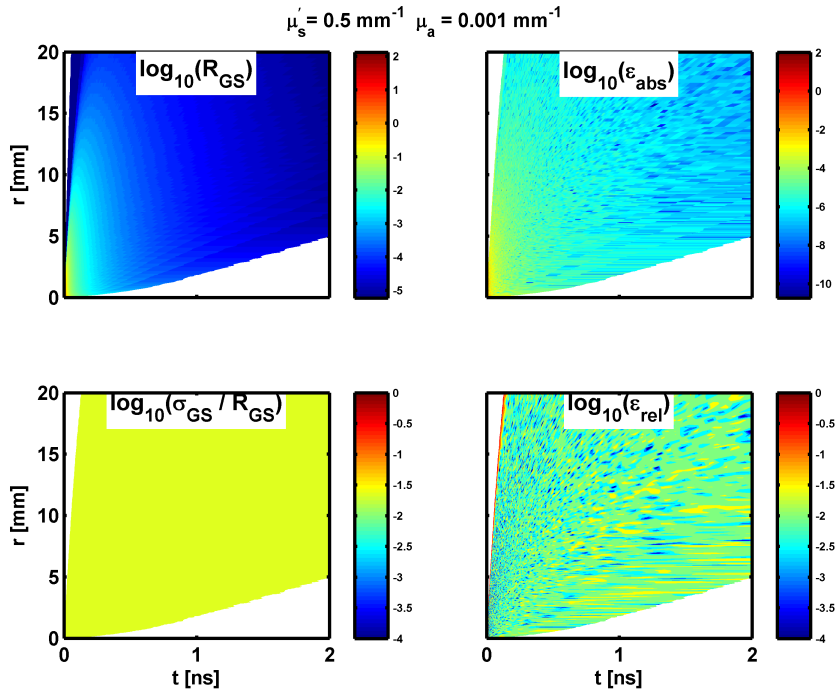

Figure 3.6: TRR error analysis for $\mu_s' = 0.5$ mm^{-1} and $\mu_a = 0.001$ mm^{-1}.

error is measured only for the earliest time bins, where the reflectance value is much smaller then the peak value. Additionally the relative standard deviation associated with the gold standard values evaluated for the first time bins at large source detector separations is generally larger than the average relative standard deviation measured over the entire physical range.

Figures 3.6, 3.7 and 3.8 show the measured quantities for a constant value of $\mu_a = 0.001$ mm^{-1} and for $\mu_s' = [0.5, 1.0, 2.0]$ mm^{-1}, respectively. For all these cases the relative standard deviation of the gold standard values is almost uniform over the entire range of investigation. Thanks to the low value of the absorption coefficient, the intrinsic uncertainty of the gold standard values is very low and the mean value of σ_{rel} evaluated from the represented physical range is always lower than 3%.

From the relative error maps one can see that the implemented forward solver is extremely accurate over the range of investigation. If we exclude the earliest times for large distances, the relative error is always smaller than 5% for any value of the scattering coefficient and the mean of the sMC relative error is as small as 1%.

These results indicate that, when μ_a is small, the sMC model is able to calculate accurately the reflectance signal even when the perturbation of the scattering coefficient with respect to the reference value is very large ($\pm$100%). From Figs. 3.8 one can see that the error introduced by the extrapolating method based on the Green's function fitting is very small when the absorption coefficient is small. The values obtained in the latest time bins for short distances are obtained by the scaling of the reference reflectance in a range where the reference nominal values were obtained

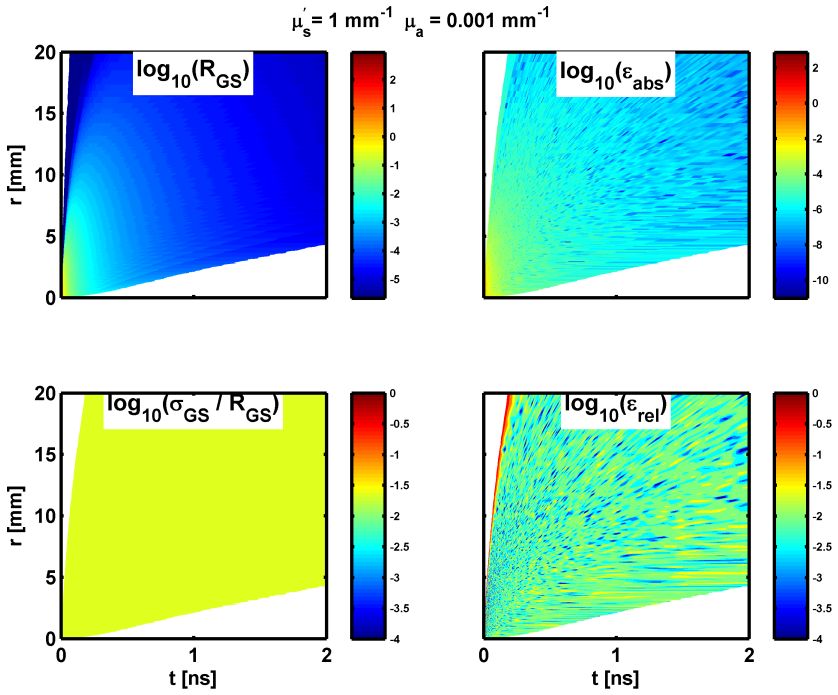

Figure 3.7: TRR error analysis for $\mu_s' = 1$ mm^{-1} and $\mu_a = 0.001$ mm^{-1}.

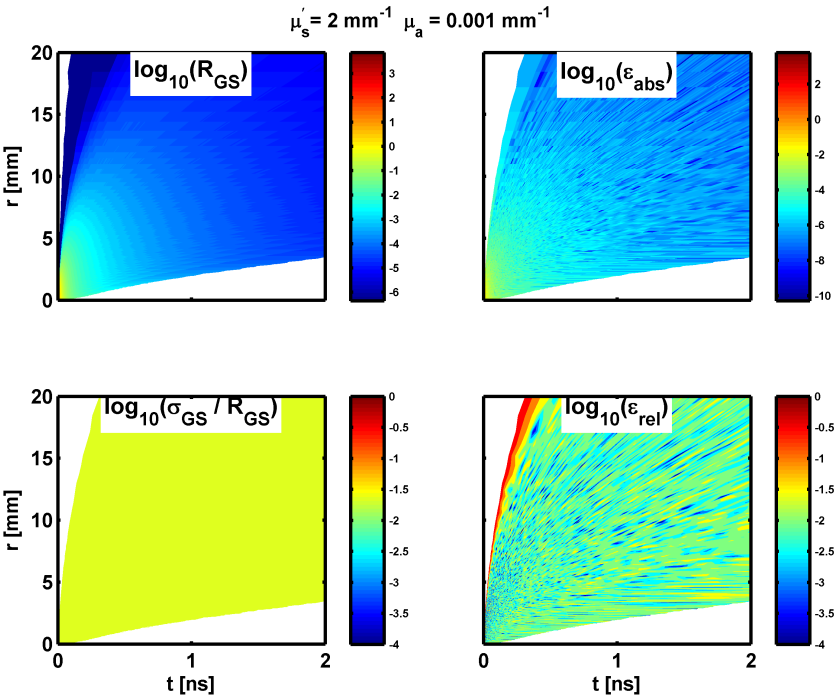

Figure 3.8: TRR error analysis for $\mu_s' = 2$ mm^{-1} and $\mu_a = 0.001$ mm^{-1}.

with the fitting approach, and the relative error is still very small.

For all the (μ_a, μ_s') pairs under investigation, it is possible to see that the reflectance values evaluated for the first time bin is as large as 100%. When the value of μ_s' becomes larger this error becomes more remarkable and the temporal range where the sMC predictions are not accurate becomes wider. This is due to the fact that the reflectance values evaluated for $\mu_s' > \mu_{s,r}'$ are the result of the shrinking of the reference values. Thus the values of $R(r,t)$ evaluated at $r = 20$ mm for $\mu_s' = 2$ mm^{-1} are mapped form the reference values calculated for $r = 40$ mm. For large source-detector separations and early times the reference values are measured with a lower accuracy due to the weakness of the reflectance signal, thus when these values are scaled to evaluate the reflectance signal the error becomes larger. As previously mentioned, one should note that the values of $R_{GS}(r_k = \text{constant}, t_l)$ measured for the earliest time bins are one or two orders of magnitude smaller that the peak value of the temporally resolved curve.

Figures 3.9, 3.10, 3.11 and 3.12 show the results of the TRR forward solver analysis for a constant value of the scattering coefficient, $\mu_s' = 1$ mm^{-1} and for $\mu_a = 0.01, 0.03, 0.1, 0.3$ mm^{-1}. It is immediate to note that increasing the value of the absorption coefficient results in larger relative errors for late times, thus the physical range where the sMC model is accurate shrinks when μ_a grows. For μ_a values smaller than 0.1 mm^{-1} and for any value of μ_s' that we have considered, the relative error measured has a mean value smaller than the mean value of the relative standard deviation of the gold standard values (which is almost constant). This is due to the smoothness of the reference signal which reduces the effect of the statistical noise. Comparing Fig. 3.7 with Fig. 3.9 one can see that the larger value of μ_a results in larger relative errors for short distances and late times. Increasing the absorption to $\mu_a = 0.03$ mm (Fig. 3.10) the range of source-detector separations and the temporal span where the error increases becomes larger.

For $\mu_a \geq 0.1$, the mean of the relative error is larger then the mean of the relative standard deviation. The error measured in the latest time bins increases as shown in Figs. 3.11 and 3.12. For $\mu_a \geq 0.1$ mm^{-1} it becomes larger than 50% and for $\mu_a = 0.3$ mm^{-1} it reaches 100% over the physical range shown. These larger inaccuracies are mainly due to the discretization error related to the measurement of the reference signal that make Eqs. (2.3) - (2.4) valid only in an approximate way. For μ_s' perturbations the error is smaller because of the linear mapping, while for μ_a perturbations the error propagates exponentially, resulting in larger inaccuracies. It is important to note that the gold standard relative standard deviation measured in these bins increases as well. More than that, while these large values of the relative error one must recognize that the high absorption results in reflectance values that are at least 8 orders of magnitude smaller than the maximum value of the $R_{\text{GS}}(r_k = \text{constant}, t_l)$ curve. When viewed in this context these relative errors are not as bad as it may appear.

One of the main limitations of the sMC method is the fact that the reference signal is measured over a finite physical range that limits the values of r and t where the reflectance can be derived and the scattering variations that can be modeled. The reference signal represented by the NURBS surface used for this work extends till 20 ns and till 100 mm, thus it is possible to overcome the dynamic range limitation previously reported. The accuracy of the results given by the sMC method for large distances and long times decreases with increasing value of the absorption coefficients. As reported by Kienle and co-workers the interpolation errors are larger for short times and small distances and for large μ_s' perturbations, where an inaccurate discretization method would lead to

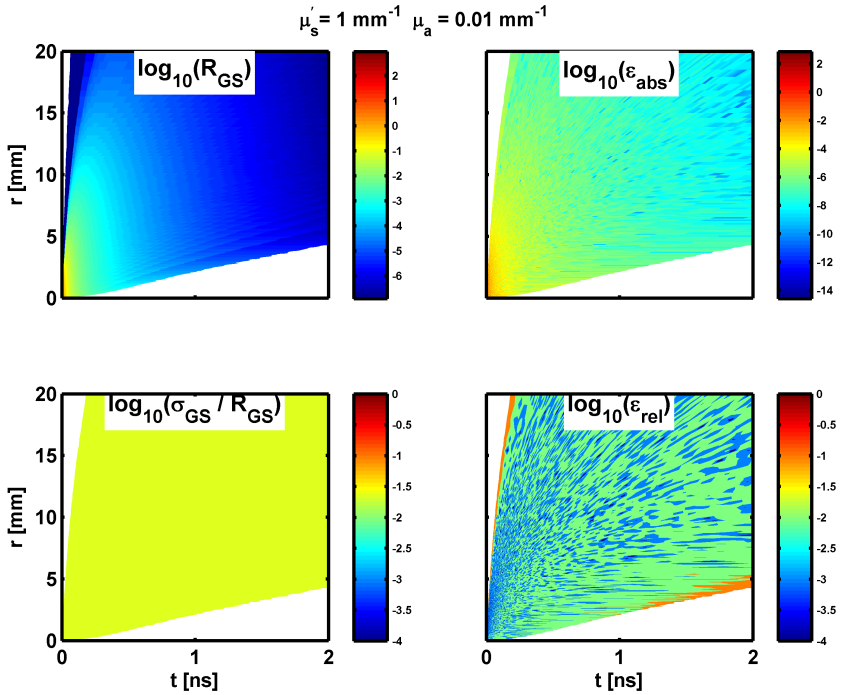

Figure 3.9: TRR error analysis for $\mu_s' = 1$ mm^{-1} and $\mu_a = 0.01$ mm^{-1}.

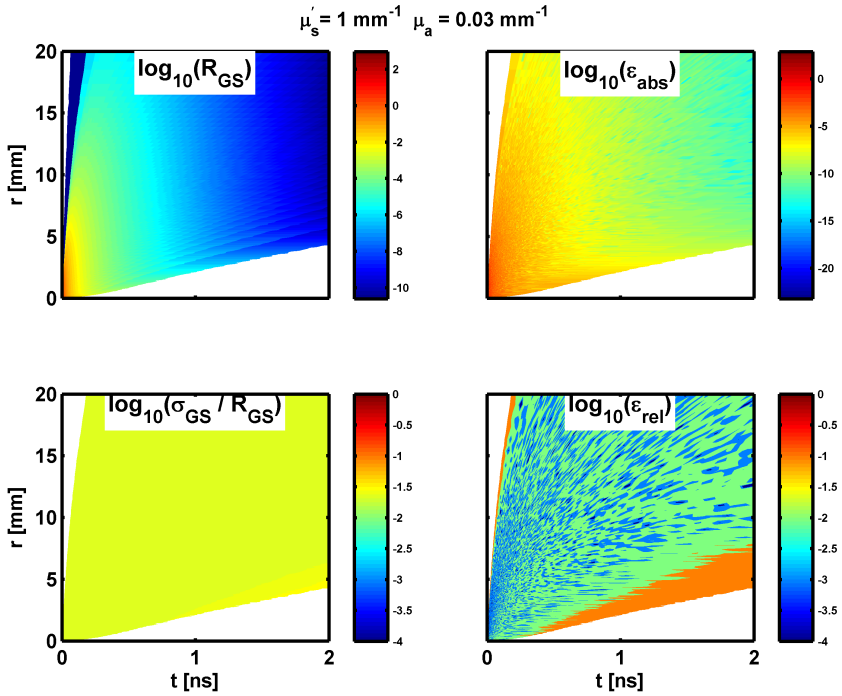

Figure 3.10: TRR error analysis for $\mu_s' = 1$ mm^{-1} and $\mu_a = 0.03$ mm^{-1}.

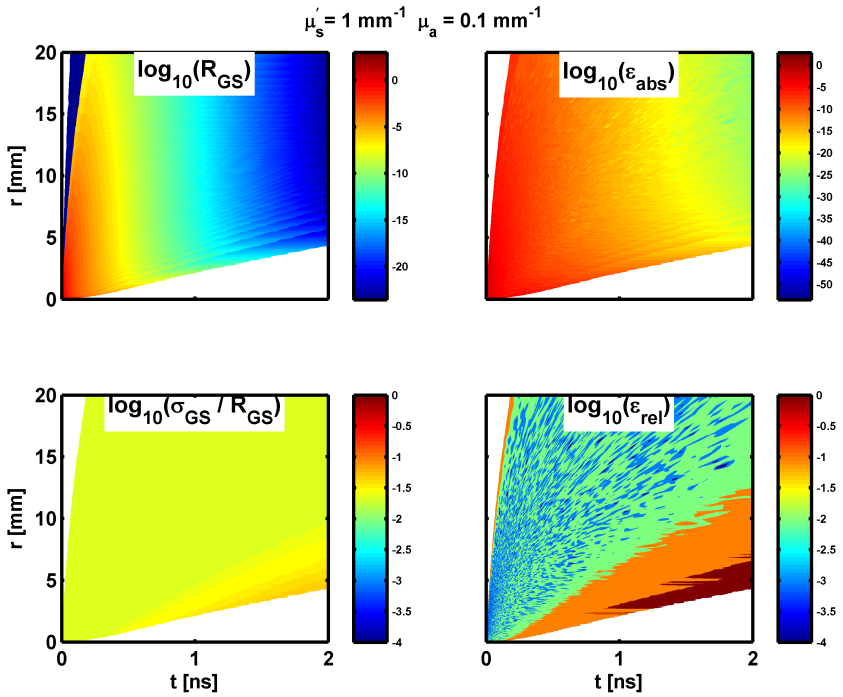

Figure 3.11: TRR error analysis for $\mu_s' = 1$ mm^{-1} and $\mu_a = 0.1$ mm^{-1}.

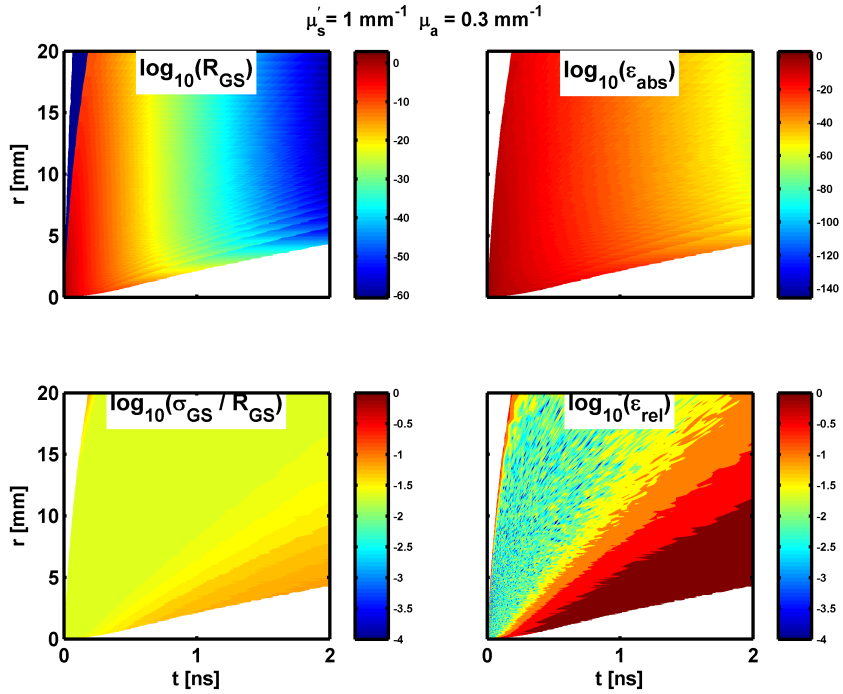

Figure 3.12: TRR error analysis for $\mu_s' = 1$ mm^{-1} and $\mu_a = 0.3$ mm^{-1}.

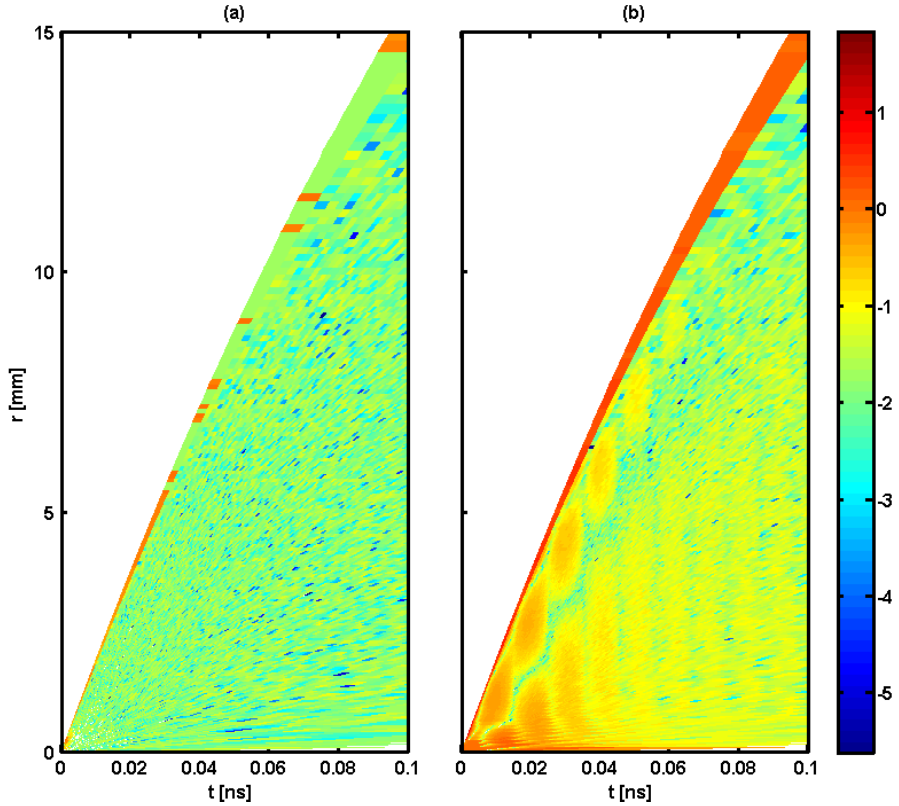

Figure 3.13: (a) Log_{10} of the relative error of the sMC_i approach using NURBS interpolation on the reference values, (b) $\log_{10}$ of the relative error of the sMC_i approach based on linear interpolation of the uniformly binned reflectance for $\mu_a = 0.1$ mm^{-1} and $\mu_s' = 0.5$ mm^{-1}

the loss of information due to the inability of obtaining nominal values that capture faithfully the rapid variations of the reflectance signal. Figure 3.13 shows the $\log_{10}$ of the relative error measured for times shorter then 0.1 ns and source detector distances smaller then 15 mm for $\mu_a = 0.1$ mm^{-1} and $\mu_s' = 0.5$ mm^{-1} using the NURBS surface built upon the reference nominal data or using linear interpolation of the reflectance binned in uniform bins with $\Delta t = 5$ ps and $\Delta r = 0.2$ mm. The improvement given by the developed approach is very clear. The reflectance signal is reproduced with good accuracy even when the optical properties chosen represent a large perturbation from the reference reflectance.

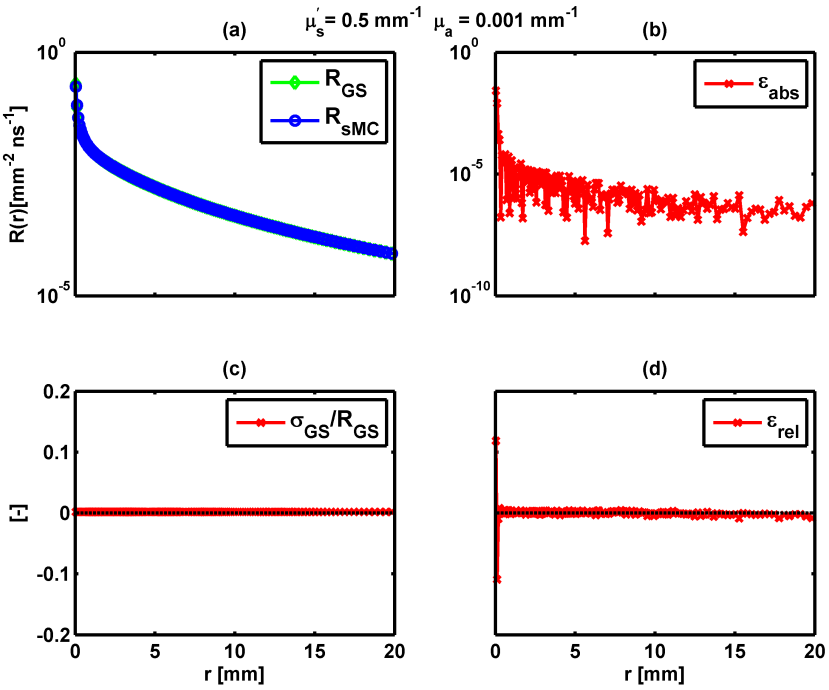

Figure 3.14: SSR error analysis for $\mu_s' = 0.5$ mm^{-1} and $\mu_a = 0.001$ mm^{-1}.

SSR Results

The results of the forward solver error analysis for the steady state reflectance, $R(r)$, are shown in Figs. 3.14 to 3.18. Each image is associated with a (μ_a, μ_s') pair and it shows (a) the $\log_{10}$ of the gold standard signal and the $\log_{10}$ of the sMC model predictions as a function of the source detector separation, (b) the $\log_{10}$ of the absolute error calculated using Eq. (3.2), (c) the relative standard deviation associated with the gold standard values and (d) the relative error of the steady state reflectance evaluated with the sMC forward solver. Thanks to the very low value of the relative standard deviation of the gold standard data it makes sense to use the relative error as a metric of comparison to evaluate the performance of the forward solver. For all the (μ_a, μ_s') pairs tested in this work, the sMC predictions show good agreement with the gold standard values. The value of the relative error seems to be unbiased as it is centered above zero. The magnitude of the relative error is in general smaller than 5% for the range $r \in [0, 20]$ mm. For all the combinations of the optical properties the maximum relative error is observed for the two shortest radial distances due to the largest interpolation error and to the the fact that a large portion of the temporally-resolved curve that is integrated to evaluate $R(r)_{\text{sMC}}$ is obtained in a region where the reference signal was obtained using the Green's function fitting approach (Eq. (2.45)).

Figures 3.14 to 3.15 show the results of the forward analysis for a constant value of $\mu_a = 0.001$ mm^{-1} and for $\mu_s' = [0.5, 2.0]$ mm^{-1}. It is remarkable that a perturbation of -100% of the scattering coefficient with respect to the reference case can be calculated with very high accuracy. For $\mu_s' = 0.5$ mm^{-1} (Fig. 3.14) the relative error is rarely larger than 1% over the entire range of analysis. When

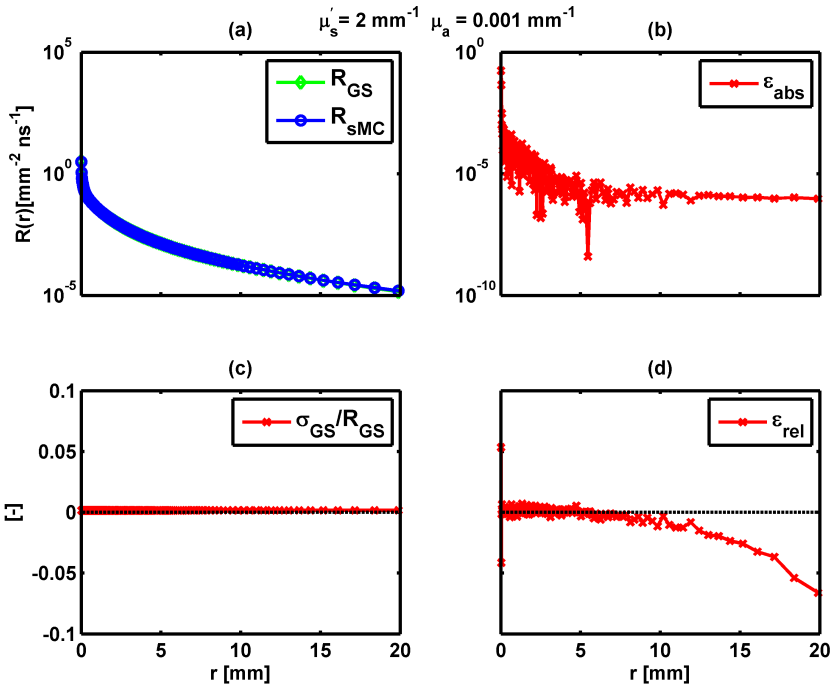

Figure 3.15: SSR error analysis for $\mu_s' = 2$ mm^{-1} and $\mu_a = 0.001$ mm^{-1}.

μ_s' is increased with respect to the reference case the results are not as good. Fig. 3.15 shows the forward solver analysis results for $\mu_s' = 2$ mm^{-1}, which corresponds to a perturbation of 100%. The spatial range where the relative error is small shrinks with respect to the previous case. This is due to the propagation of discretization and interpolation errors and to the larger inaccuracy of the reference signal, $R_r(r, t)$, for larger source detector separations.

Figures 3.16, 3.17 and 3.18 show the forward solver analysis for an absorption perturbation, $\mu_a = 0.01, 0.1, 0.3$ mm^{-1}, and for a value of the scattering coefficient equivalent with the value of the reference reflectance. Increasing the absorption results in larger errors for the long source-detector separations. As mentioned in § 2.2 both the scaling equations are valid as an approximation, the error due to the scaling propagates linearly while the one associated with the absorption de-weighting propagates exponentially leading to larger errors even for the SSR domain. One should note that in the range of source-detector separations where the forward solver results inaccurate for high values of the absorption coefficient, the gold standard signal, $R_{GS}(r_k, t_l)$, is from 5 to 10 orders of magnitude smaller than the peak of the reflectance curve.

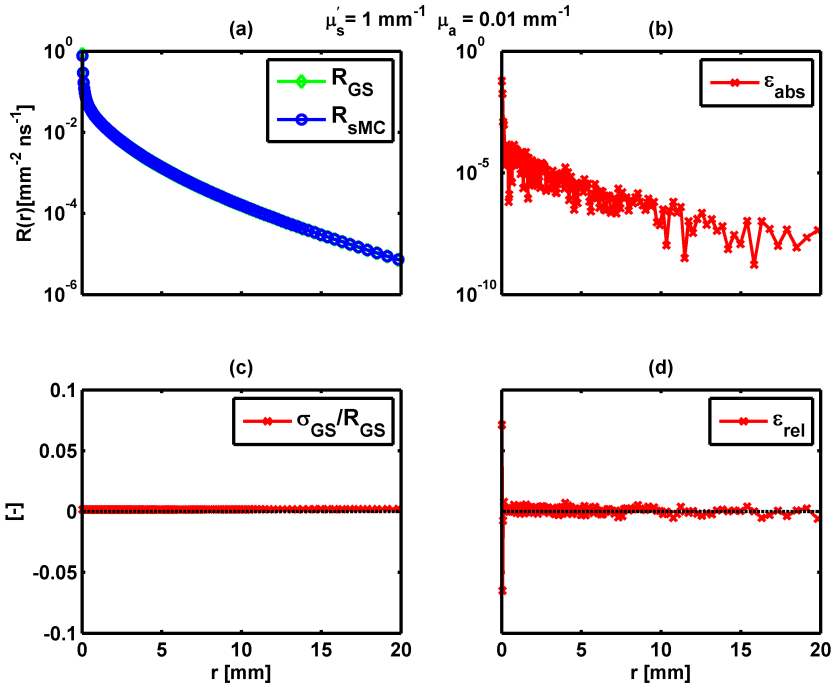

Figure 3.16: SSR error analysis for $\mu_s' = 1$ mm^{-1} and $\mu_a = 0.01$ mm^{-1}.

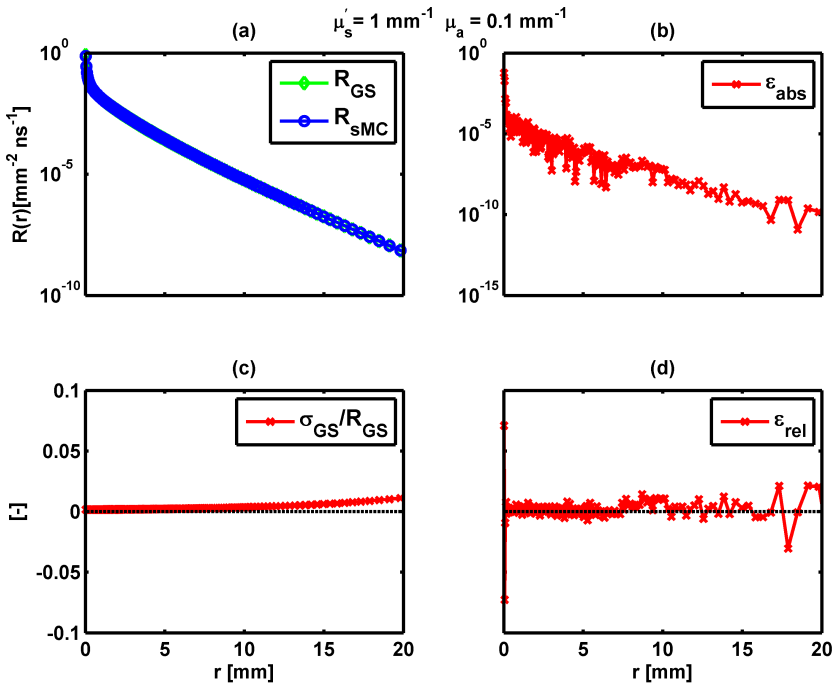

Figure 3.17: SSR error analysis for $\mu_s' = 1$ mm^{-1} and $\mu_a = 0.1$ mm^{-1}.

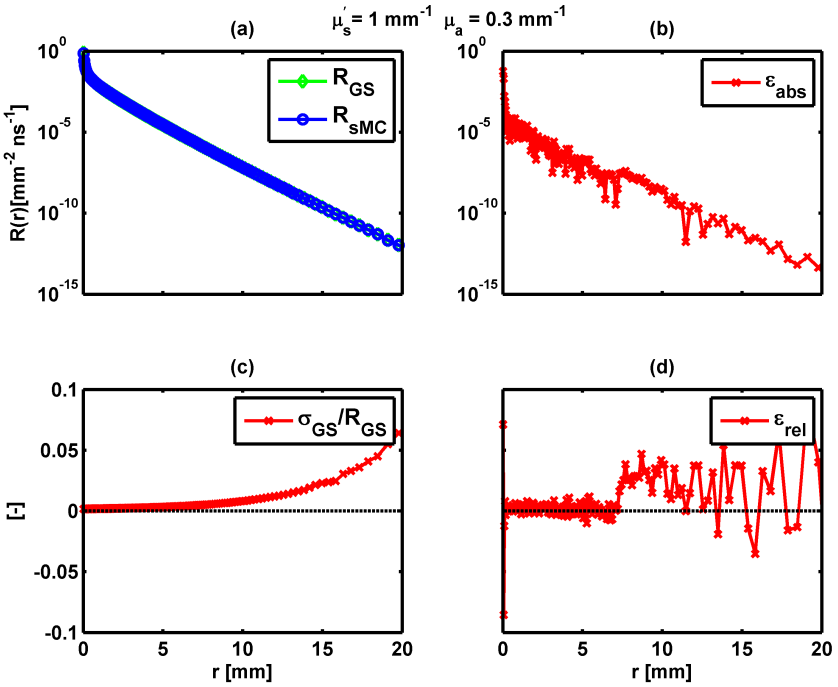

Figure 3.18: SSR error analysis for $\mu_s' = 1$ mm^{-1} and $\mu_a = 0.3$ mm^{-1}.

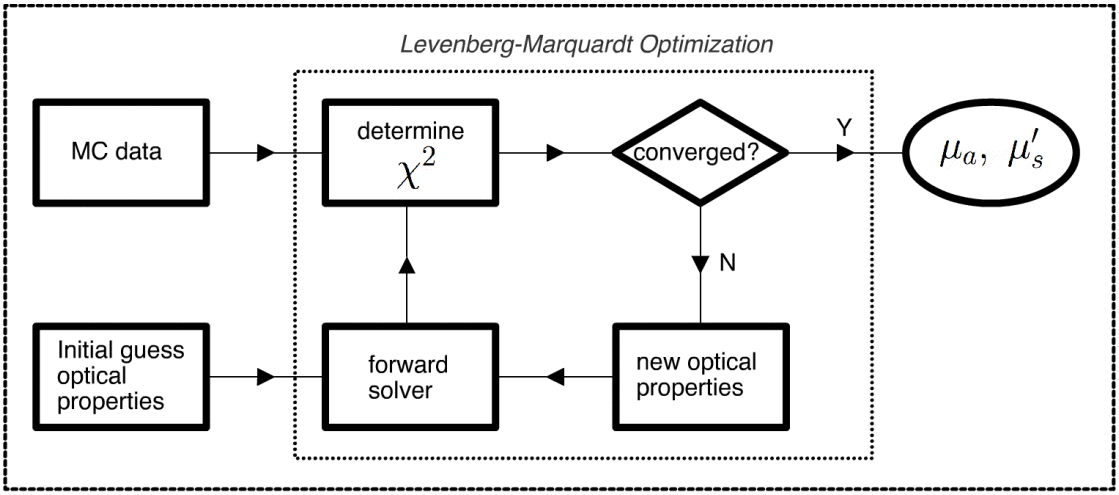

Figure 3.19: Schematic representation of the nonlinear optimization algorithm.

3.3 Inverse Solver Analysis

The recovery of optical properties (OPs) from measured reflectance signals is performed solving an inverse problem. Here we analyze the capability of the implemented sMC model to solve such inverse problem for different spectroscopy domains. Such model is used in conjunction with a nonlinear optimization algorithm to determine the set of optical properties that produce a prediction of the reflectance that best matches the experimental data.

3.3.1 Inversion Scheme

Figure (3.19) shows the generic inversion scheme used for the OPs recovery. Non-linear least squares fitting is an integral part of most spectroscopy analysis. The process embodies the fundamental process of hypothesis testing for a candidate forward model which may explain the data. In each step of the algorithm, simulated measurements data is generated using independent MC simulations. The forward model employed is the NURBS forward solver based on the single Monte Carlo method. A Levenberg-Marquardt (LM) [39] algorithm minimizes the sum of squares differnce, χ^2, between the measured data and the model predictions at trial optical properties. χ^2 is defined as

$$\chi^2 = \sum_{i=1}^{D} \left[\frac{R_{m,i} - R_{p,i}(\mu_a, \mu_s')}{\sigma_i} \right]^2 \tag{3.5}$$

where D is the number of measured reflectance values, R_m is the measured data, R_p represents the reflectance predicted by the forward model given optical properties (μ_a, μ_s') and σ_i is the standard deviation associated with each measured point. The trial OPs are adjusted until one of the imposed convergence criteria is verified. For a maximum number of iterations $I = 200$, we set the relative chi-square convergence criterium (i.e. the relative difference between χ^2 values resulting from

successive iterations), the relative parameter convergence criterium (i.e. the relative difference between the input optical properties values chosen for successive iterations) and the orthogonality convergence criterium (i.e. the degree to which the residuals are orthogonal to the Jacobian columns) all to the threshold value $t_h = 10^{-10}$.

To ensure full sampling of the parameter space and to avoid convergence to local minima we executed nine trials of the LM algorithm using various combinations of optical properties as an initial guess. We chose $\mu_a = [0.0042, 0.0173, 0.0721]$ mm^{-1} to cover uniformly the log_{10} of the absorption range $[0.001 - 0.3]$ mm^{-1} and values of $\mu_s' = [0.875, 1.250, 1.625]$ mm^{-1} to sample the scattering range $[0.5 - 2]$ mm^{-1} in a uniform way. For every converged trial we store the estimated OPs and the calculated χ^2 and the elapsed time, ΔT. The average of the recorded values $(\mu_{a,a},\ \mu_{s,a}')$ and the best OPs $(\mu_{a,b},\ \mu_{s,b}')$ i.e. those with the lowest χ^2, are output. We calculate the relative error of the output values as

$$\begin{aligned} \epsilon_{rel}(\mu_a) &= \frac{|\mu_a - \mu_{a,r}|}{\mu_a} \\ \epsilon_{rel}(\mu_s') &= \frac{|\mu_s' - \mu_{s,r}'|}{\mu_s'} \end{aligned} \tag{3.6}$$

where $(\mu_a,\ \mu_s')$ are the true OPs and $(\mu_{a,r},\ \mu_{s,r}')$ are those recovered (best or average) by the inversion algorithm. To evaluate the general performance of the forward model in the inverse problem solution for time resolved measurements we calculate the mean of the these relative errors over all the set of optical properties tested. Thus we define

$$\begin{aligned} \bar{\epsilon}_{rel}(\mu_a) &= \sum_i \epsilon_{rel}(\mu_{a,i}) \\ \bar{\epsilon}_{rel}(\mu_s') &= \sum_i \epsilon_{rel}(\mu_{s,i}') \end{aligned} \tag{3.7}$$

where i is the index representing each specific set of optical properties tested. We use the notations $\bar{\epsilon}_{rel,b}(\mu_a)$ and $\bar{\epsilon}_{rel,b}(\mu_s')$ to indicate the mean relative errors obtained from all the best results (which means that for every set of OPs we measure the relative error of the iteration with the lowest χ^2 and then we average them) and the notations $\bar{\epsilon}_{rel,a}(\mu_a)$ and $\bar{\epsilon}_{rel,a}(\mu_s')$ to indicate the mean of the relative errors obtained from the average results (which means that for every set of OPs we measure the relative error of the average OPs recovered with the multiple trials and then we average them). We chose to follow this approach to be able to present the results in a concise way.

3.3.2 Data Generation

For this work an extensive set of SSR data, $R(r)$, and TRR data, $R(r, t)$ were generated through MC simulations. For all the simulations we assumed constant value of anisotropy, $g = 0.8$, and constant refractive index, $n = 1.4$. The absorption coefficient spanned the range $\mu_a = [0.001 - 0.3]$ mm^{-1}, while the value of the scattering coefficient covered the range $\mu_s' = [0.5 - 2]$ mm^{-1}. The

noise level of the data measured from a MC simulation depends on the number of injected photons, N. According to photon noise statistics [38] the $SNR = R/\sigma$ increases as a square law as a function of N. For this study we used $N = 10^8$ for each set of optical properties.

Using MC simulated data the only source of noise is the intrinsic variability of the measured values due to the stochastic nature of the MC method. The large amount of photons traced results in SSR signals with mean $SNR > 100$ and TRR signals with mean $SNR > 15$ for all the optical properties under investigation. To assert the robustness of the inversion model in a less ideal case we reprocessed the measured data adding an increasing percentage of Gaussian noise, $n_p = [0.1\%, 1\%, 10\%]$.

When dealing with fitting problems it is important to note that the accuracy of the recovered parameters does not rely only on the quality of the forward model and of the inversion algorithms adopted. Another main factor that plays a crucial role in the accuracy of the results is the 'quality' of the measured data used to calculate χ^2 using Eq. (3.5). Apart from the SNR of the reflectance values other factors that influence the accuracy of the recovered OPs are the physical resolution of the detectors (Δr and Δt), the number of measured points fed to the optimization algorithm and the physical range over which these data are collected. For the spectroscopy domains under investigation we considered various sets of inverse problem situations to fully determine the performance of the implemented NFS.

TRR Data

The values of $R(r_k, t_l)$ was computed using Eq. (1.20) and each bin was represented by its middle point, r_k and its middle point , t_l.The standard deviation of the reflectance measured in the specific bin has been calculated using Eq (1.23). The spatially- and temporally-resolved reflectance has been calculated over the range $r \in [0 - 22]$ mm and $t \in [0 - 5]$ ns. We used uniform radial bins of width $\Delta r = 0.25$ mm to discretize the spatial dimension.

For the discretization of the temporal dimension we used different values of $\Delta t = (1, 5, 25)$ ps. These values were chosen following the time resolution of some TCSPC systems available on the market [40, 41]. The measured reflectance data was generated at s-d separations $r_k = [0.3, 1, 2, 5, 10, 20]$ mm. For all these radial distances we measured $R(r_k, t_l)$ using the different time resolutions. The larger source-detector separations (r = 10, 20 mm) have been chosen to evaluate the performance of the sMC forward solver for the recovery of optical proprieties in the diffusive regime. The other s-d separations are generally to small to use models based on the diffusion approximation, thus we seek higher performances of the sMC model over this range.

Apart from the s-d separation and the time resolution, another factor that affects the accuracy of the recovered OPs is the fitting range, i.e. the ' temporal portion' of the $R(t)$ curve fed to the inversion algorithm. The influence of the choice of the fitting range for TRR curves has been discussed in several articles [42, 17, 18]. In this work the fit was performed in a range of the curve delimited by two markers where the measured signal was over a fixed threshold. Different marker combinations have been tested to evaluate the influence of the fitting range. The right marker was set on the tail of the curve to exclude points where the reflectance is lower then $m_t = [20\%, 1\%, 0.1\%]$ of the peak of the curve. The left marker was set to $m_r = [80\%, 50\%]$ on the leading edge of the signal. The standard choice, suggested by Cubeddu and coworkers is to use $m_r = 80\%$ and $m_t = 1\%$. We

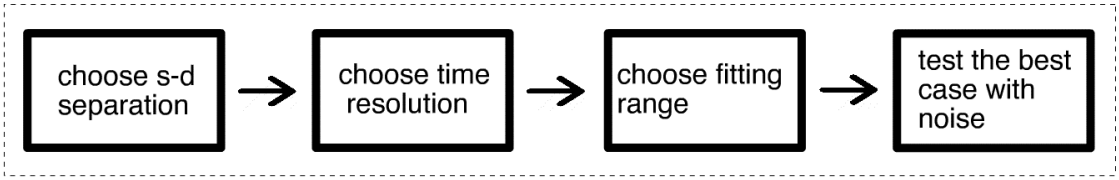

Figure 3.20: Schematic representation of the TRR data analysis.

consider this fitting range, (80/1), as the reference case.

The choice of these markers influences the number of fitted reflectance values, D, which affects the computational time and the accuracy of the results. Using the same fitting markers and the same temporal resolution, Δt, for a fixed radial location, does not result in a constant value of D for different optical properties, because the fitting range depends on the amplitude of the reflectance signal. We indicate with $\bar{D}$ the mean number of points fitted for specific values of the markers, of the temporal resolution and of the radial distance obtained by averaging the number of points fitted for each set of OPs under investigation.

The flowchart in Fig. (3.20) illustrates the steps followed for the analysis of TRR data. For each radial distance we establish the most appropriate time resolution using the standard markers. Then we evaluate the influence of the other fitting ranges on the performance of the inversion procedure. We base the choice of the best parameters on the mean relative errors, $\bar{\epsilon}_{rel}(\mu_a)$ and $\bar{\epsilon}_{rel}(\mu_s')$, of the recovered OPs and on the computing time required to solve the inverse problem. We indicate with $\bar{\Delta T}$ the mean computing time for specific values of the markers, of the temporal resolution and of the radial distance obtained by averaging the computing time measured for each of the sets of OPs under investigation. Once we define the parameters which yield the best results we note the degradation of the NFS performance as the percentage of noise added to the measured curves is increased.

SSR Data

The SSR data were calculated over a radial range that extended till a maximal radial distance $r_{max} = 22$ mm. We used a set of annular bins with $\Delta r = 0.25$ mm were the simulated photons are tallied to evaluate $R(r_k)$ using Eq. (1.22). The value of r_k is given by the middle position of the k-th radial bin. All the photons reflected within r_{max} are accounted without performing any sort of time gating. The standard deviation of each steady state reflectance point was calculated using Eq. (1.23). We evaluated the influence of the number of detectors, D, where the signal is collected. We used $D = [86, 43, 21, 11]$ equi-spaced detectors to cover uniformly the entire range of measurement. When the number of detectors is reduced we use the same bins but we discard some of them, no gathering or larger detectors have been used. For each pair (μ_a, μ_s') tested we measure the time, ΔT, elapsed for the solution of the inverse problem using the sMC model. The computing time for a single $R(r)$ curve calculated over 100 points is shorter then 2 seconds. However the multiple iterations needed to solve the inverse problem results in long computing times, especially when a larger number of detectors is used. The process (described in § 2.4) is not optimal for the SSR domain as it requires the computation of all the $R(r, t)$ curves for each radial distance and

their integration in order to obtain the SSR signal.

3.3.3 TRR Optical Properties Recovery

Tables 3.1, 3.2, 3.3, 3.4, 3.5 and 3.6 summarize the performance of the NFS for the OPs recovery from TRR measurements without noise addition for the six source-detector separations considered in this work. For each combination of time resolution and fitting range these tables report the mean of the relative error of the recovered values for the best and for the average case, the mean time elapsed for the inverse problem solution and the mean number of time bins. These values were calculated averaging the measured values of all the fifteen sets of optical properties under investigation to have a general overview regarding the performance of the proposed model over a wide range of OPs, for different source-detector separations and for different features of the analyzed curves.

Non-Diffusive Regime

When the distance between the source and the detector is too small, i.e $r < 3l^*$, the true angular distribution of the photons that travel through the medium can not be neglected, thus model based on the standard diffusion approximation can not be used as they assume an isotropic distribution of light within the propagating medium. Short source detector separations are an interesting case for the analysis of reflectance signals as they are associated with a lower depth probed by the photons, thus can yield and isolate informations relative to the upper layers of the tissue. For this porpoise it is necessary to have a model that can be used to solve inverse problems quickly and accurately. The forward analysis performed in § 3.2, showed that the sMC solver implemented for this work can be used to derive the reflectance signal $R(r, t)$ for source detector separations that fall within the non-diffusive regime. The values calculated by the sMC model agree with the gold standard values obtained through MC simulations, thus the solver can potentially be used for the recovery of OPs for this range. Here we show the results obtained from the inversion for four s-d separations of $r = 0.3, 1, 2, 5$ mm. The last one can be assumed as a boundary between the diffusive and the non-diffusive regime considering the optical properties range under investigation.

For the shortest radial distance, $r = 0.3$ mm (Table 3.1), the lowest errors are obtained using the smallest time resolution, $\Delta t = 1$ ps, and the (80/0.1) fitting range. In this case the mean relative error of the best recovered values is around 60% for μ_a and around 2% for μ_s'. Reducing the temporal resolution to 5 or 25 ps results in the impossibility of capturing the rapid dynamic of the TRR curves at such a short s-d separation. Reducing the fitting range on the tail to $m_t = [1\%, 20\%]$ increases the relative error of the measured absorption while the accuracy of the recovered reduced scattering seems to have small dependence on the fitting range. The worsening of the recovered μ_a is mainly due to the fact that most of the photons collected at this distance have very short pathlength, so a wider portion of the curve needs to be included in the fitting range to gain sensitivity to the absorption coefficient. It is interesting to note that the value of $\bar{\epsilon}_{rel,b}(\mu_a)$ for $\Delta t = 1$ ps and fitting range (80/0.1) is reduced to 3.9% if the measurements with $\mu_a = 0.001$ mm^{-1} are excluded from the averaged ensemble. The lack of sensitivity to absorption due to short pathlengths is accentuated for small values of μ_a, even resulting in negative values of the recovered absorption. It is remarkable that the recovered average OPs have very good agreement with the best ones indicating that the

Table 3.1: Averaged inverse problem results for TRR measurement at $r = 0.3$ mm.

Δt **[ps]**	m_r **%**	m_t **%**	$\bar{\epsilon}_{rel,b}(\mu_a)$	$\bar{\epsilon}_{rel,a}(\mu_a)$	$\bar{\epsilon}_{rel,b}(\mu_s')$	$\bar{\epsilon}_{rel,a}(\mu_s')$	$\bar{\Delta T}$**[sec]**	$\bar{D}$
1	80	0.1	0.635	0.635	0.019	0.019	0.20	114
1	80	1.0	1.496	1.496	0.021	0.022	0.12	43
1	50	1.0	1.510	1.510	0.020	0.020	0.08	43
1	50	20.0	8.614	8.614	0.030	0.030	0.02	9
5	80	0.1	2.755	2.755	0.082	0.082	0.05	30
5	80	1.0	7.209	7.056	0.091	0.090	0.02	12
5	50	1.0	7.209	7.056	0.091	0.090	0.03	12
5	50	20.0	26.659	26.659	0.111	0.111	0.01	4
25	80	0.1	9.754	9.558	0.850	0.839	0.02	8
25	80	1.0	14.927	16.409	0.935	0.994	0.01	4
25	50	1.0	14.927	16.409	0.935	0.994	0.01	4
25	50	20.0	28.534	30.202	1.082	1.167	0.01	2

performance of the inversion algorithm is almost independent from the initial guess. This would allow us to reduce the number of trials for the resolution of the inverse problem which would reduce the computing time.

Comparing the recovered OPs using the different time resolutions for the standard fitting range, (80/1), It is clear that the smaller time resolution yields the most accurate results. The measured μ_s' is generally within 10% of the real value even for $\Delta t = 5$ ps. For the most accurate temporal resolution the influence of the fitting range on the recovered OPs was analyzed. Using the range (80/0.1) improves the accuracy of the recovered μ_a, except for the cases where $\mu_a = 0.001$ mm^{-1}. The recovered μ_s' is only weakly affected by the fitting range. The relative error $\epsilon_{rel,b}(\mu_s')$ is always smaller then 2%.

For the case with the lower relative errors, i.e. $\Delta t = 1$ ps, $m_r = 80\%$ and $m_t = 0.1\%$, we tested the performance of the NFS for the OPs recovery from TRR measurements with addition of different noise percentages. The results are shown in Fig (3.21). For $n_p = [0.1\%, 1\%]$ the effect of the noise addiction does not worsen the precision of the recovered parameters. For $n_p = 10\%$ the results become less accurate, but, discarding the relative error of the recovered absorption coefficients for the cases with $\mu_a = 0.001$ mm $^{-1}$, the measured coefficients remain within 10% of the true values.

For the second source-detector separation, $r = 1$ mm, the highest performance is obtained for $\Delta t = 1$ ps, $m_r = 80\%$ and $m_t = 0.1\%$. The averaged results are shown in Table (3.2). With respect to the previous radial distance there is a clear improvement in the recovery of the absorption coefficient. The mean error, $\epsilon_{rel,b}(\mu_a)$, is 15%. Once again, excluding the cases with $\mu_a = 0.001$ mm^{-1} results in a reduction of $\epsilon_{rel,b}(\mu_a)$ to 1.4%. The recovered values of μ_s' are in general within 2% of the true values. The average time lapse necessary to solve the inverse problem with nine initial guesses is $\bar{\Delta T} = 0.5$ sec. The good agreement between the best and the average mean relative errors indicates that the number of initial guesses could be reduced.

Even for a s-d separation of $r = 1$ mm, it is desirable to have a time resolution of 1 ps to obtain

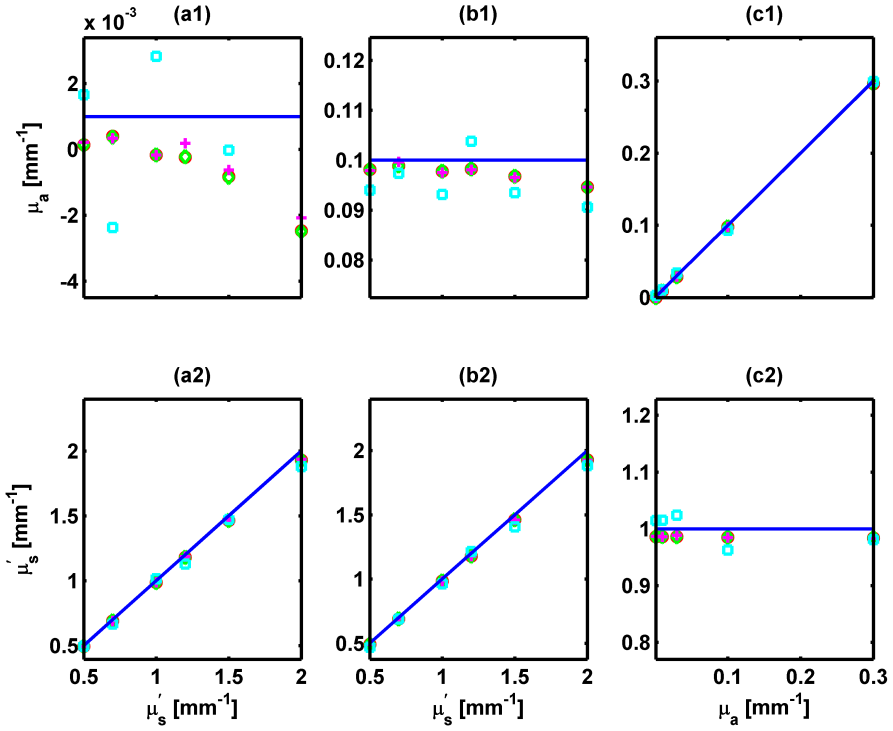

Figure 3.21: Recovered optical properties from TRR curves at $r = 0.3$ mm, using $\Delta t = 1$ ps, fitting range (80/0.1), for noise percentage addition (○) $n_p = 0\%$, (◇) $n_p = 0.1\%$, (+) $n_p = 1\%$, (□) $n_p = 10\%$

Table 3.2: Averaged inverse problem results for TRR measurement at $r = 1$ mm.

Δt **[ps]**	m_r **%**	m_t **%**	$\bar{\epsilon}_{rel,b}(\mu_a)$	$\bar{\epsilon}_{rel,a}(\mu_a)$	$\bar{\epsilon}_{rel,b}(\mu_s')$	$\bar{\epsilon}_{rel,a}(\mu_s')$	$\Delta\bar{T}$**[sec]**	$\bar{D}$
1	80	0.1	0.145	0.145	0.012	0.012	0.48	222
1	80	1.0	0.486	0.442	0.021	0.020	0.20	91
1	50	1.0	0.448	0.402	0.015	0.018	0.17	92
1	50	20.0	3.186	3.755	0.039	0.084	0.05	20
5	80	0.1	1.039	0.934	0.083	0.088	0.17	50
5	80	1.0	2.306	2.376	0.109	0.112	0.06	21
5	50	1.0	2.306	2.376	0.109	0.112	0.06	21
5	50	20.0	18.375	17.481	0.382	0.421	0.03	6
25	80	0.1	4.002	6.919	0.450	0.876	0.06	13
25	80	1.0	9.807	10.487	0.483	0.927	0.02	6
25	50	1.0	9.807	10.487	0.483	0.927	0.03	6
25	50	20.0	50.703	68.588	4.540	4.358	0.01	2

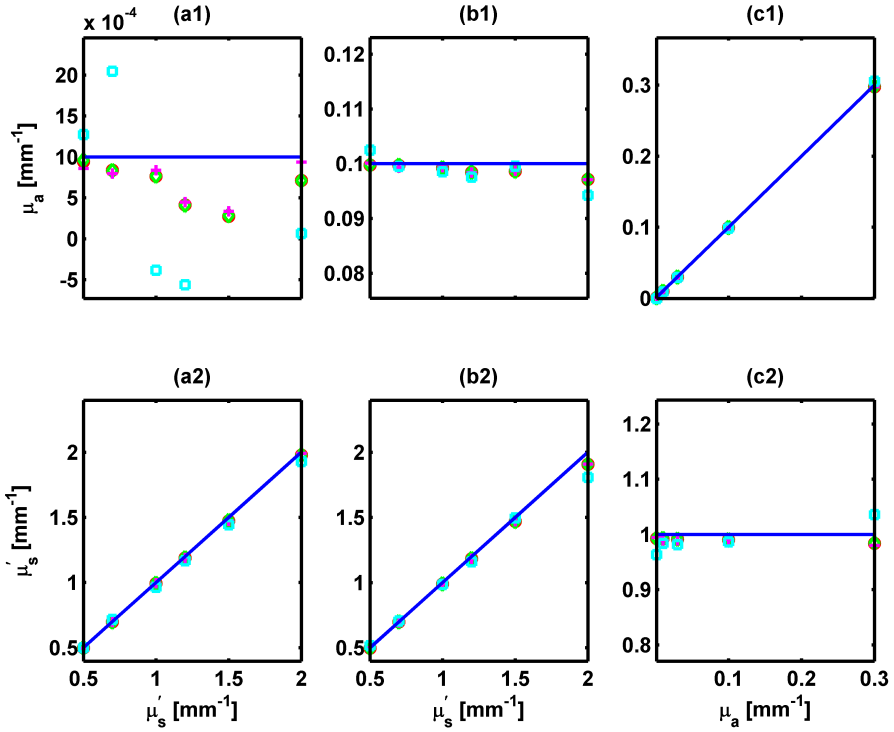

Figure 3.22: Recovered optical properties from TRR curves at $r = 1$ mm, using $\Delta t = 1$ ps, fitting range (80/0.1), for noise percentage addition (○) $n_p = 0\%$, (◇) $n_p = 0.1\%$, (+) $n_p = 1\%$, (□) $n_p = 10\%$

accurate results. Compared to the previous case the improvement in the measured μ_s' using $\Delta t = 1$ ps instead of $\Delta t = 5ps$ is clear. Using the (80,0.1) fitting range instead of the standard one results in a slight improvement of the recovered OPs. The larger portion of the tail allows to improve the estimation of the absorption coefficient.

For different percentage of added noise, we used the sMC model for the recovery of OPs for $r = 2$ mm using $\Delta t = 1$ ps and using the (80,0.1) fitting range. The accuracy of the recovered values worsens slightly only for $n_p = 10\%$ as one can see in Fig. (3.22).

For $r = 2$ mm, the averaged results are reported in Table (3.3). The mean relative errors of the best recovered OPs for $\Delta t = 1$ ps, $m_r = 80\%$ and $m_t = 0.1\%$, are 5% and 1% for μ_a and μ_s' respectively. The larger contributions to $\epsilon_{rel,b}(\mu_a)$ are due to the cases with the smallest value of the absorption coefficient, but at this s-d separation most of the collected photons have a pathlength sufficiently large to gain more sensitivity to μ_a. For this radial distance the best recovered OPs have a relative error that is around one order of magnitude smaller then the average case, indicating that a reduction of the number of initial guesses would affect the quality of the recovered parameters.

The recovered OPs for different time resolutions using the standard fitting range, (80/1), have been compared. Even using $\Delta t = 5$ ps results in accurate recovered OPs, but the best performances are obtained for the smallest time resolution, $\Delta t = 1$ ps.

Table 3.3: Averaged inverse problem results for TRR measurement at $r = 2$ mm.

Δt **[ps]**	m_r **%**	m_t **%**	$\bar{\epsilon}_{rel,b}(\mu_a)$	$\bar{\epsilon}_{rel,a}(\mu_a)$	$\bar{\epsilon}_{rel,b}(\mu'_s)$	$\bar{\epsilon}_{rel,a}(\mu'_s)$	$\bar{\Delta T}$**[sec]**	$\bar{D}$
1	80	0.1	0.050	1.864	0.011	0.193	1.63	370
1	80	1.0	0.154	3.231	0.023	0.355	0.68	157
1	50	1.0	0.142	4.818	0.021	0.370	0.57	158
1	50	20.0	1.543	10.215	0.054	0.404	0.11	37
5	80	0.1	0.107	3.346	0.035	0.268	0.35	76
5	80	1.0	0.315	5.250	0.043	0.367	0.16	33
5	50	1.0	0.315	5.250	0.043	0.367	0.16	33
5	50	20.0	1.431	10.381	0.074	0.407	0.03	8
25	80	0.1	0.306	3.686	0.182	0.433	0.15	20
25	80	1.0	0.821	4.477	0.285	0.425	0.06	10
25	50	1.0	0.821	4.477	0.285	0.425	0.06	10
25	50	20.0	3.118	8.115	0.457	0.608	0.02	3

Analyzing the results using different fitting ranges one can note the improvement obtained using the (80/0.1) fitting range. Using the standard range for this distance reduces the mean computing time by half because of the smaller number of time bins included in the analysis. Anyway the value of $\bar{\Delta T}$ for the (80/0.1) range is smaller then 2 seconds and yields more accurate results. Using the (80/0.1) fitting range with $\Delta t = 1$, the implemented model has been tested adding increasing percentages of noise. The results reported in Fig. (3.23) indicate that only for $n_p = 10\%$ the accuracy is slightly reduced.

Table (3.4) shows the results obtained for s-d separation $r = 5$ mm. The choice of the best parameters is between the two cases $\Delta t = 1$ ps, $m_r = 50\%$ and $m_t = 20\%$ or $\Delta t = 5$ ps, $m_r = 80\%$ and $m_t = 0.1\%$. Even if the second one has a larger value of $\bar{\Delta T}$ and of $\epsilon_{rel,b}(\mu'_s)$, the improvement of the recovered μ_a and the good agreement of the average errors, $\bar{\epsilon}_{rel,a}(\mu_a)$ and $\bar{\epsilon}_{rel,a}(\mu'_s)$, with the best ones, $\bar{\epsilon}_{rel,b}(\mu_a)$ and $\bar{\epsilon}_{rel,b}(\mu'_s)$, of the second case led us to choose it as the best candidate.

For the standard range the quality of the results is similar using both $\Delta t = 1$ ps or $\Delta t = 5$ ps. A time resolution of 1 ps with the (80/0.1) fitting range results in a larger number of measured points included in the fitting problem. The increase in the measured relative errors may be partially caused by the inaccuracy of the NFS in the representation of the tail of the reflectance curve for long times and relatively short distances. The good results obtained reducing the temporal resolution to 5 ps over the same fitting range may signify that the relative error increase is due to the number of points processed by the inversion scheme: including a larger number of values characterized by lower SNR on the tail of the signal does not add useful information and the performance of the inversion scheme is reduced.

For a s-d separation of $r = 5$ mm, it is possible to see that the influence of the different fitting ranges is quite weak: only for the case with $\mu_a = 0.001$ mm^{-1} and $\mu'_s = 0.5$ mm^{-1} the improvement given by the (80/0.1) fitting range becomes apparent. The NFS results illustrate the robustness of the method to the addition of noise because the accuracy of the recovered OPs decreases only for

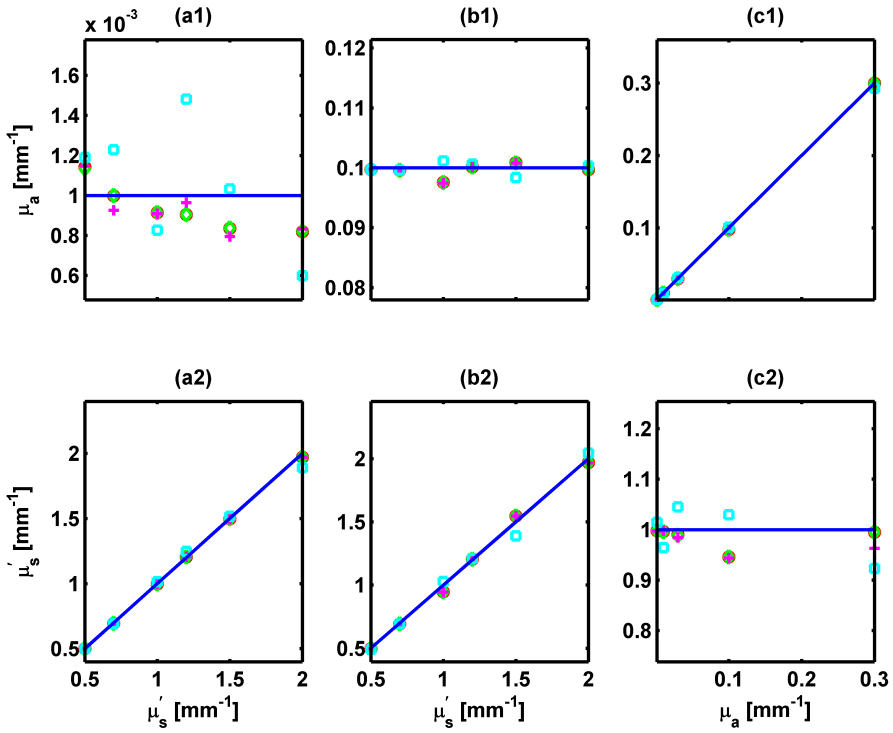

Figure 3.23: Recovered optical properties from TRR curves at $r = 2$ mm, using $\Delta t = 1$ ps, fitting range (80/0.1), for noise percentage addition (○) $n_p = 0\%$, (◇) $n_p = 0.1\%$, (+) $n_p = 1\%$, (□) $n_p = 10\%$

Table 3.4: Averaged inverse problem results for TRR measurement at $r = 5$ mm.

Δt **[ps]**	m_r **%**	m_t **%**	$\bar{\epsilon}_{rel,b}(\mu_a)$	$\bar{\epsilon}_{rel,a}(\mu_a)$	$\bar{\epsilon}_{rel,b}(\mu_s')$	$\bar{\epsilon}_{rel,a}(\mu_s')$	$\bar{\Delta T}$**[sec]**	$\bar{D}$
1	80	0.1	0.036	0.036	0.016	0.021	2.95	881
1	80	1.0	0.103	0.111	0.021	0.024	1.24	409
1	50	1.0	0.081	0.081	0.019	0.019	1.08	414
1	50	20.0	0.078	0.201	0.009	0.017	0.29	111
5	80	0.1	0.014	0.021	0.015	0.034	0.74	186
5	80	1.0	0.103	0.103	0.020	0.025	0.29	84
5	50	1.0	0.097	0.104	0.018	0.025	0.28	85
5	50	20.0	0.158	0.268	0.011	0.025	0.06	23
25	80	0.1	0.309	0.342	0.165	0.174	0.14	40
25	80	1.0	0.453	0.517	0.171	0.183	0.06	19
25	50	1.0	0.454	0.472	0.171	0.173	0.06	19
25	50	20.0	0.738	0.738	0.190	0.187	0.02	6

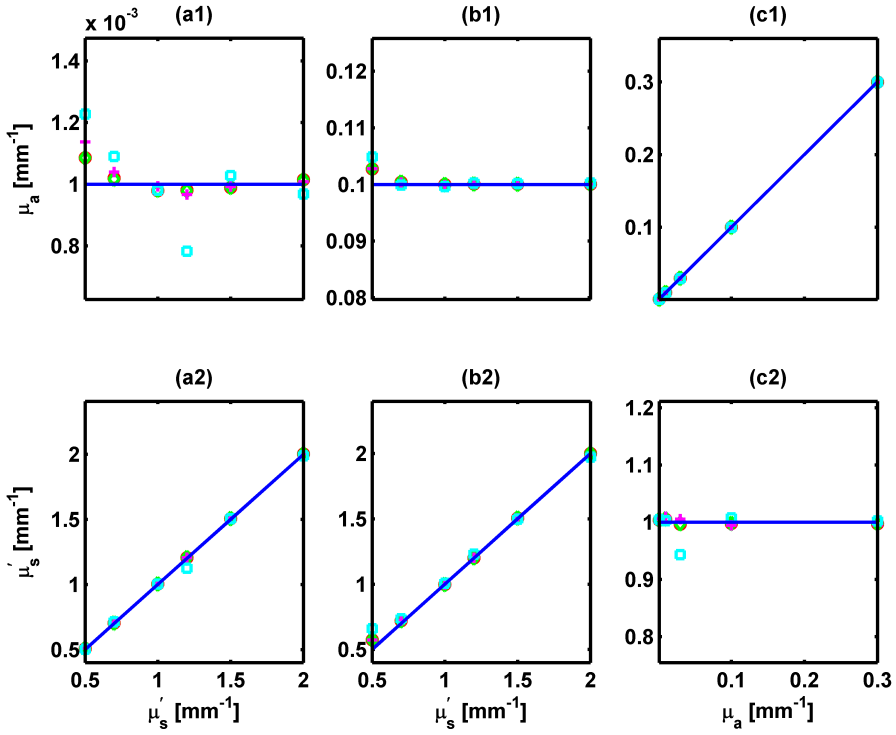

Figure 3.24: Recovered optical properties from TRR curves at $r = 5$ mm, using $\Delta t = 5$ ps, fitting range (80/0.1), for noise percentage addition (○) $n_p = 0\%$, (◇) $n_p = 0.1\%$, (+) $n_p = 1\%$, (□) $n_p = 10\%$.

Table 3.5: Averaged inverse problem results for TRR measurement at $r = 10$ mm.

Δt **[ps]**	m_r **%**	m_t **%**	$\bar{\epsilon}_{rel,b}(\mu_a)$	$\bar{\epsilon}_{rel,a}(\mu_a)$	$\bar{\epsilon}_{rel,b}(\mu_s')$	$\bar{\epsilon}_{rel,a}(\mu_s')$	$\Delta\bar{T}$**[sec]**	$\bar{D}$
1	80	0.1	0.280	0.075	0.269	0.036	6.09	1766
1	80	1.0	0.023	0.089	0.004	0.041	3.98	1061
1	50	1.0	0.023	0.035	0.004	0.011	2.80	1083
1	50	20.0	0.032	0.035	0.005	0.012	0.84	306
5	80	0.1	0.008	0.037	0.004	0.023	1.49	395
5	80	1.0	0.007	0.056	0.004	0.016	0.81	212
5	50	1.0	0.007	0.277	0.003	0.009	0.75	215
5	50	20.0	0.026	0.207	0.004	0.024	0.23	64
25	80	0.1	0.005	0.047	0.008	0.048	0.31	81
25	80	1.0	0.009	0.073	0.010	0.051	0.23	44
25	50	1.0	0.009	0.012	0.009	0.025	0.25	45
25	50	20.0	0.026	0.025	0.010	0.008	0.05	14

seldom cases and for $n_p = 10\%$ as illustrated in Fig (3.24).

Diffusive Regime

For a source-detector separation as large as $5l^*$, models based on the standard diffusion approximation can be used for the recovery of OPs [5]. Monte Carlo techniques are typically used for the non diffusive regime, where other analytical models fail in the accurate description of the reflectance signals. From the forward solver analysis presented in § 3.2 we have understood that the implemented sMC model can be used to derive $R(r, t)$ both for the non-diffusive and for the diffusive regime. Here we show two examples to establish if the implemented forward solver can be used for the solution of inverse problems in the diffusive-regime.

Table 3.5 shows the OPs recovery results for a s-d separation of $r = 10$ mm. We chose the parameters $\Delta t = 5$ ps, $m_r = 80\%$ and $m_t = 1\%$ as they yield the best performance for the solution of the inverse problem. The best recovered OPs agree within 1% of the true values for most of the cases under investigation. The average values show very good agreement with the best ones and the computing time is smaller than 1 second. Increasing the s-d separation enables the OPs recovery from TRR curves to become less challenging and other combinations of time resolution and markers yield accurate results.

Analyzing the influence of different time resolutions one can see that the larger number of time bins associated with the smallest Δt worsens the efficiency of the fitting algorithm. Using $\Delta t = 5$ ps instead of $\Delta t = 25$ ps gives a slight improvement.

All the fitting ranges can be used without ever compromising the accuracy of the recovered OPs. Only for the smallest μ_a, using $m_t = 20\%$ reduces the precision in the estimation of the absorption coefficient. The recovered OPs with the addition of noise are shown in Fig. (3.25). At this s-d separation the NFS is very robust to the presence of noise and the recovered OPs are always within 3% of the true values even for $n_p = 10\%$.

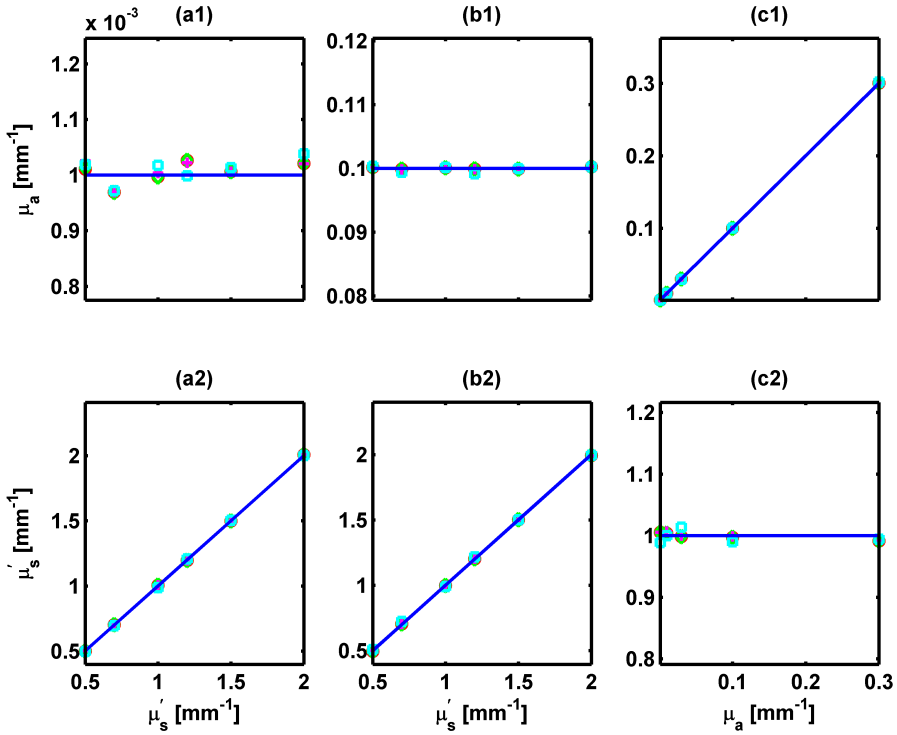

Figure 3.25: Recovered optical properties from TRR curves at $r = 10$ mm, using $\Delta t = 5$ ps, fitting range (80/1), for noise percentage addition (○) $n_p = 0\%$, (◇) $n_p = 0.1\%$, (+) $n_p = 1\%$, (□) $n_p = 10\%$

Table 3.6: Averaged inverse problem results for TRR measurement at $r = 20$ mm.

Δt **[ps]**	m_r **%**	m_t **%**	$\bar{\epsilon}_{rel,b}(\mu_a)$	$\bar{\epsilon}_{rel,a}(\mu_a)$	$\bar{\epsilon}_{rel,b}(\mu_s')$	$\bar{\epsilon}_{rel,a}(\mu_s')$	$\Delta\bar{T}$**[sec]**	$\bar{D}$
1	80	0.1	0.601	0.071	0.602	0.091	9.66	2148
1	80	1.0	0.423	0.093	0.405	0.101	10.01	1745
1	50	1.0	0.489	0.073	0.469	0.057	7.40	1791
1	50	20.0	0.298	0.281	0.271	0.228	3.21	748
5	80	0.1	0.076	0.082	0.073	0.082	2.14	440
5	80	1.0	0.076	0.064	0.072	0.066	1.96	401
5	50	1.0	0.076	0.123	0.072	0.045	1.88	414
5	50	20.0	0.076	0.270	0.075	0.135	0.94	171
25	80	0.1	0.005	0.127	0.007	0.088	0.46	90
25	80	1.0	0.004	0.113	0.004	0.068	0.54	81
25	50	1.0	0.005	0.253	0.007	0.068	0.39	83
25	50	20.0	0.008	0.421	0.009	0.120	0.22	36

A source detector of $r = 20$ mm is as large as $10l^*$ for all the optical properties considered in this work. For this radial distance the larger value of Δt is the one characterized by the lower relative errors, as one can see in Table (3.6). The smallest Δt yields too many points and the fitting algorithm does not always converge. For $m_r = 80\%$ and $m_t = 1\%$ we obtain $\epsilon_{rel,b}(\mu_a) = 0.4\%$ and $\epsilon_{rel,b}(\mu_s') = 0.4\%$, even the for the average case the recovered OPs are close to the true ones.
We chose the standard fitting range, but its improvement compared to the other cases is very small. The robustness against the addition of noise is satisfactory even for this distance as even for $n_p = 10\%$ the recovered OPs are very close to the true ones, resulting in relative errors generally smaller than 2% as shown in Fig. (3.26).

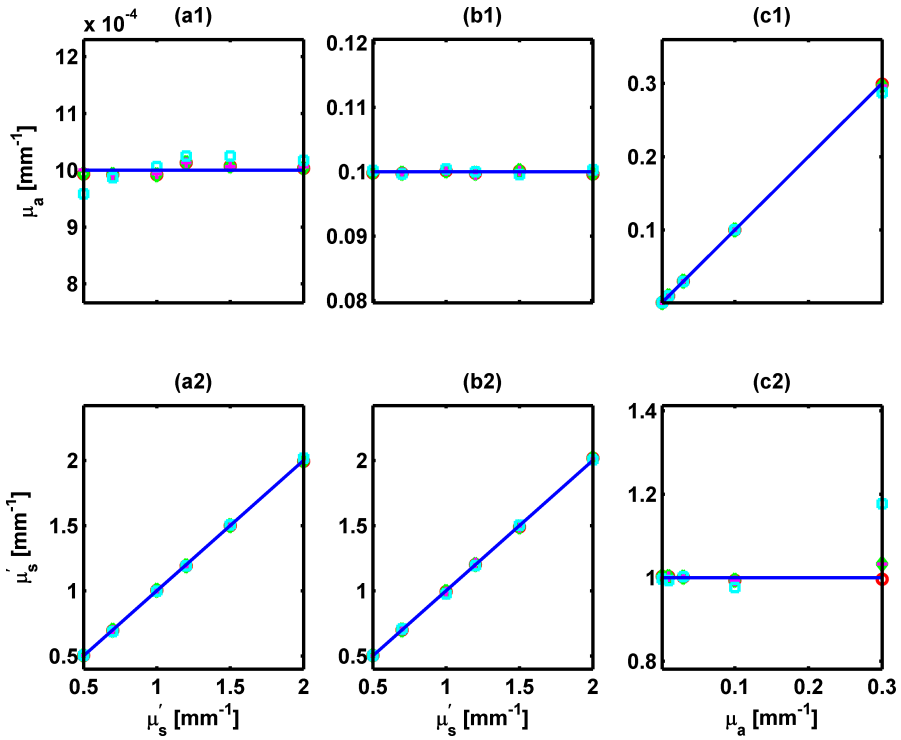

Figure 3.26: Recovered optical properties from TRR curves at $r = 20$ mm, using $\Delta t = 25$ ps, fitting range (80/0.1), for noise percentage addition (○) $n_p = 0\%$, (◇) $n_p = 0.1\%$, (+) $n_p = 1\%$, (□) $n_p = 10\%$

Table 3.7: Inverse problem results for $r \in [0.5 - 22]$ mm using 86 detectors without noise addition.

$\mu_a[\mathbf{mm}^{-1}]$	$\epsilon_{rel,b}(\mu_a)$	$\epsilon_{rel,a}(\mu_a)$	$\mu'_s[\mathbf{mm}^{-1}]$	$\epsilon_{rel,b}(\mu'_s)$	$\epsilon_{rel,a}(\mu'_s)$	$\Delta T[\mathbf{sec}]$	D
0.001	0.075	1.013	0.5	0.0152	0.3522	257	86
0.001	0.018	1.157	0.7	0.0006	0.0812	172	86
0.001	0.008	1.833	1.0	0.0003	0.0038	204	86
0.001	0.053	1.953	1.2	0.0007	0.0286	203	86
0.001	0.971	1.736	1.5	0.082	0.1442	153	86
0.001	1.015	1.878	2.0	0.0811	0.2691	165	86
0.010	0.002	0.130	1.0	0.0003	0.0925	133	86
0.030	0.002	0.277	1.0	0.0000	0.2578	155	86
0.100	0.002	0.314	0.5	0.0001	1.0813	128	86
0.100	0.002	0.213	0.7	0.0005	0.5633	142	86
0.100	0.002	0.211	1.0	0.0003	0.5222	164	86
0.100	0.002	0.106	1.2	0.0002	0.2735	215	86
0.100	0.002	0.104	1.5	0.0005	0.2714	191	86
0.100	0.004	0.004	2.0	0.0008	0.0008	214	86
0.300	0.003	0.003	1.0	0.0006	0.0006	229	86

3.3.4 SSR Optical Properties Recovery

Number of Detectors

The results obtained for the inverse problem over the range $r \in [0.5 - 22]$ mm changing the number of virtual detectors used for the signal detection are reported in Tables 3.7, 3.8, 3.9 and 3.10. The represented values are (following the column order) the true value of the absorption coefficient, μ_a, the relative error of the best recovered μ_a, $\epsilon_{rel,b}(\mu_a)$, the relative error of the average recovered μ_a, $\epsilon_{rel,a}(\mu_a)$, the true value of the reduced scattering coefficient, μ'_s and the respective best, $\epsilon_{rel,b}(\mu'_s)$, and average, $\epsilon_{rel,a}(\mu'_s)$, relative errors, the time elapsed to solve the inverse problem, ΔT, and the number of detectors used, D.

The values reported in Table (3.7) were obtained using all the virtual detectors used to cover the measurement domain. To evaluate the ideal performance of the NFS for inverse problems in the steady state domain no noise was added to the measured signals. The recovered OPs are in general within 10% of the real values. For small values of the absorption coefficient, $\mu_a = 0.001$ mm^{-1}, and for large scattering coefficients, $\mu'_s > 1.2$ the relative error of the best recovered μ_a increases, but it remains smaller then 10% for the recovered scattering coefficients. From the forward solver analysis performed in § 3.2 one would expect the worsening of the results associated with higher values of the scattering coefficient where the model becomes less accurate. This effect is enhanced when a large number of detectors is situated in a region where the sMC results are not accurate. The measured ΔT is always larger then 2 minutes. This is due to the large amount of time needed to compute $R(r)$ with the NFS. We tried to use a discrete summing method instead of the analytical integration of the NURBS curves. The time decreases by a factor smaller then 2% and the accuracy of the recovered OPs was only slightly modified. For the solution of an inverse problem the computational

Table 3.8: Inverse problem results for $r \in [0.5 - 22]$ mm using 43 detectors without noise addition.

$\mu_a[\mathbf{mm}^{-1}]$	$\epsilon_{rel,b}(\mu_a)$	$\epsilon_{rel,a}(\mu_a)$	$\mu'_s[\mathbf{mm}^{-1}]$	$\epsilon_{rel,b}(\mu'_s)$	$\epsilon_{rel,a}(\mu'_s)$	$\Delta T[\mathbf{sec}]$	D
0.001	0.367	0.669	0.5	0.0105	0.0300	70	43
0.001	0.094	0.899	0.7	0.0106	0.0108	79	43
0.001	0.044	1.062	1.0	0.0006	0.0463	64	43
0.001	0.050	1.190	1.2	0.0013	0.0821	70	43
0.001	0.077	2.066	1.5	0.0020	0.1451	62	43
0.001	0.081	2.920	2.0	0.0008	0.2142	64	43
0.010	0.002	0.100	1.0	0.0004	0.0135	71	43
0.030	0.002	0.300	1.0	0.0001	0.1437	63	43
0.100	0.002	0.325	0.5	0.0001	0.6540	62	43
0.100	0.002	0.327	0.7	0.0002	0.5576	71	43
0.100	0.002	0.319	1.0	0.0003	5.7322	82	43
0.100	0.002	0.313	1.2	0.0001	1.0192	87	43
0.100	0.002	0.210	1.5	0.0010	0.5078	95	43
0.100	0.003	0.201	2.0	0.0010	1.2958	97	43
0.300	0.003	0.003	1.0	0.0007	0.0007	102	43

burden depends on the number of detectors, on the convergence criteria and on the number of initial guesses that are input to the LM algorithm. The accuracy of the average results is clearly worse then the best case, for this reason the reduction of the initial guesses would strongly affect the accuracy of the recovered parameters because the solver performance seems to be strongly dependent from the initial guess.

The previous results consider al the virtual detectors where the SSR signal was recorded. The presented cases are not typical of real life situations. When the spatial distribution of photons is measured with camera-based systems ([7]) the adjacent pixels are generally gathered to obtain a smaller number of measured values with a higher SNR. For fiber-based systems [8, 9] the typical number of probes used to cover a radial range that spans 2 cm, is around 10. Tables 3.8, 3.9 and 3.10 show the result obtained reducing the number of detectors over the same range to $D = [43, 21, 11]$ respectively.

Reducing by half the number of virtual detectors, the performance of the NFS does not change strongly for the recovery of the optical properties as reported in Table 3.8. The recovered values of μ_a are worse in the case of low absorption, while the measurement of μ'_s is improved as the best results are always within 2% of the real values. Even for this case the solver exhibits a strong dependency from the OPs initial guess so the number of iterations required for the inversion ca not be reduced and the computing time required is over a minute.

The performance of the NFS as a forward solver for inverse problem resolution improves compared to the previous cases when the number of detectors is further reduced, as one can see from Tables 3.9 and 3.10. This may be due to the fact that when larger data are analyzed to solve fitting problems the additional amount of information may be excessive. If the data is not consistent due to presence of intrinsic noise the performance of the inversion algorithm decreases. As noted during the forward

Table 3.9: Inverse problem results for $r \in [0.5 - 22]$ mm using 21 of the detectors without noise addition.

$\mu_a[\mathbf{mm}^{-1}]$	$\epsilon_{rel,b}(\mu_a)$	$\epsilon_{rel,a}(\mu_a)$	$\mu_s'[\mathbf{mm}^{-1}]$	$\epsilon_{rel,b}(\mu_s')$	$\epsilon_{rel,a}(\mu_s')$	$\Delta T[\mathbf{sec}]$	D
0.001	0.057	0.366	0.5	0.0016	0.0579	31	21
0.001	0.021	0.531	0.7	0.0012	0.0166	29	21
0.001	0.044	0.874	1.0	0.0011	0.0477	35	21
0.001	0.055	1.712	1.2	0.0008	0.0832	33	21
0.001	0.078	2.205	1.5	0.0021	0.1406	35	21
0.001	0.074	2.809	2.0	0.0003	0.1756	38	21
0.010	0.003	0.149	1.0	0.0009	0.0087	36	21
0.030	0.002	0.299	1.0	0.0006	0.1427	32	21
0.100	0.002	0.325	0.5	0.0003	0.7209	27	21
0.100	0.003	0.220	0.7	0.0006	0.2890	34	21
0.100	0.002	0.324	1.0	0.0002	0.6232	49	21
0.100	0.002	0.314	1.2	0.0006	1.1728	54	21
0.100	0.002	0.315	1.5	0.0011	0.9063	50	21
0.100	0.004	0.115	2.0	0.0010	1.4017	50	21
0.300	0.003	0.003	1.0	0.0003	0.0003	52	21

Table 3.10: Inverse problem results for $r \in [0.5 - 22]$ mm using 11 of the detectors without noise addition.

$\mu_a[\mathbf{mm}^{-1}]$	$\epsilon_{rel,b}(\mu_a)$	$\epsilon_{rel,a}(\mu_a)$	$\mu_s'[\mathbf{mm}^{-1}]$	$\epsilon_{rel,b}(\mu_s')$	$\epsilon_{rel,a}(\mu_s')$	$\Delta T[\mathbf{sec}]$	D
0.001	0.069	0.065	0.5	0.0013	0.0950	15	11
0.001	0.067	0.407	0.7	0.0007	0.0069	15	11
0.001	0.035	1.037	1.0	0.0004	0.0277	15	11
0.001	0.057	1.280	1.2	0.0005	0.0609	16	11
0.001	0.077	1.155	1.5	0.0023	0.0947	16	11
0.001	0.078	2.133	2.0	0.0003	0.1220	18	11
0.010	0.003	0.221	1.0	0.0003	0.0276	16	11
0.030	0.002	0.303	1.0	0.0001	0.1709	15	11
0.100	0.002	0.325	0.5	0.0005	0.8709	15	11
0.100	0.003	0.316	0.7	0.0003	1.0343	18	11
0.100	0.002	0.312	1.0	0.0001	0.7792	19	11
0.100	0.002	0.318	1.2	0.0017	4.1567	20	11
0.100	0.001	0.305	1.5	0.0019	1.2741	23	11
0.100	0.003	0.306	2.0	0.0002	4.0477	22	11
0.300	0.003	0.202	1.0	0.0003	7.6092	25	11

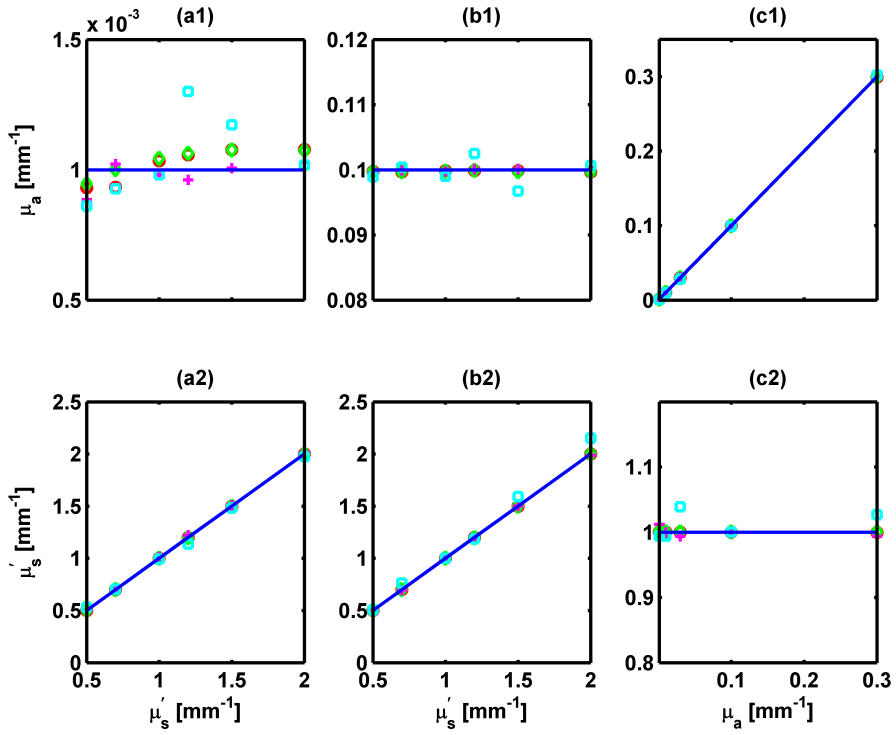

Figure 3.27: Recovered optical properties from SSR curves obtained using $D = 11$ detectors over the range $r \in [0 - 22]$ mm, for noise percentage addition (○) $n_p = 0\%$, (◇) $n_p = 0.1\%$, (+) $n_p = 1\%$, (□) $n_p = 10\%$

solver analysis the sMC model is less accurate for large s-d separations, thus reducing the amount of data collected within the further regions results in an improvement of the recovered values. When the number of detectors is reduced to 21 the best recovered μ_a has a relative error always smaller then 10%. Only for the smaller value of the absorption coefficient this error exceeds 1%. The measured scattering coefficient is always within 0.5% of the true μ'_s. The accuracy of the measured OPs is only slightly worse when the number of detectors is reduced to 11. This reduction results in a computing time which becomes less then half of the previous case. Even for this case the discrepancy between the best OPs and the average ones does not allow one to reduce the number of initial guesses.

NFS Performance with Noise

The performance of the NFS for the recovery of optical properties from SSR data has been tested in the presence of noise. We decided to use the smallest number of detectors, $D = 11$, considered in this study. This is because it is the closest approximation of typical SSR spectroscopy measurements with optical fibers systems. The results are reported in Fig. (3.27). As previously reported, the OPs estimated in the ideal case ($n_p = 0\%$) are within 10% of the true absorption coefficient and within 1% of the true reduced scattering coefficient for all the cases under investigation. For

$n_p = [0.1\%, 1\%]$ the accuracy of the recovered OPs is comparable with the ideal case. The relative error of the recovered absorption is larger than 1% only for $\mu_a = 0.001$ mm^{-1} but it still remains smaller than 10%. The recovered μ_s' is always within 1% of the real value.

For $n_p = 10\%$ and $\mu_a = 0.001$ mm^{-1} the relative error measured for the recovered absorption coefficient reaches 20%,while the measured μ_s' is always within 2% of the true value. For $\mu_a \geq 0.001$ mm^{-1} the value of $\epsilon_{rel,b}(\mu_a)$ is always smaller than 5%, while $\epsilon_{rel,b}(\mu_s')$ is larger then 5% only for $\mu_s' = 2.0$ mm^{-1}. For constant value of $\mu_s' = 1$ and different values of the absorption coefficient the recovered μ_a has a relative error always smaller than 1%, while $\epsilon_{rel,b}(\mu_s')$ is larger than 1% only in one case.

Conclusions

This thesis has focused on the single Monte Carlo (sMC) method (Kienle 1996) which provides radiative transport estimates in a homogeneous medium, for an arbitrary set of optical properties, by rapidly reprocessing the results from a single reference Monte Carlo simulation.

This model describes the relationship between the light signal reflected by a turbid medium and its optical properties. Thus sMC can be used to quantify optical absorption and scattering from measured reflectance signals. The importance of this approach relies on the fact that it overcomes the computational burden associated with traditional Monte Carlo simulations and it can potentially be used to derive reflectance estimates without any physical limitation. While this approach has been adopted by many groups around the world, no one had yet provided a theoretical foundation for its validity, nor a rigorous investigation of its accuracy.

In this work it has been shown how the scaling relations, used for the single Monte Carlo method, can be derived from the RTE and are valid for infinite and semi-infinite geometries only. First of all we provided a justification of the linear scaling used to model scattering variations based on the non-dimensionalization of the Radiative Transport Equation. The equation used to model the effect of non-zero absorption is justified using continuous absorption weighting. Using Beer's Law of attenuation the photon's weights are exponentially reduced according to their total path inside the medium.

This theoretical analysis shows that, although the sMC principles are rigorously valid, the application of the sMC method based on the interpolation of a set of nominal values obtained from a reference simulations is an approximation. This is because the scaling equations are applied on average values obtained from ensembles of photons collected within temporal and spatial bins. The sMC model is rigorous only if applied on a photon by photon basis, which means that each photon biography needs to be stored and post-processed. The photon-by-photon approach was used to prove that the reflectance estimates provided by the traditional MC simulations and the sMC technique are equivalent.

Even if the sMC method, based on the interpolation of the reference values, does not provide a rigorous solution of the radiative problem, its application is faster and the storage size required is smaller when compared to the photon-by-photon approach. The challenge in such method is to construct a reference reflectance over a wide physical range in a way that minimizes the discretization error and its propagation due to interpolation.
In this work three different discretization approaches have been tested. The first one is commonly defined as equal width discretization (EWD) and is based on the subdivision of the physical range

into bins of constant size. The second approach, referred to as equal frequency discretization (EFD), divides the sorted values so that each interval contains approximately the same number of training instances. Both EFD and EWD are referred as parametric binning techniques because the number of bins is determined a priori by the user without any reference to the properties of the training data. To overcome the limitations related to these approaches, we developed an adaptive discretization (AD) technique. The number of bins in this case is not imposed *a priori* and the bin limits are dynamically built trying to satisfy a set of conditions that constrained the number of photons collected within each interval and the three dimensional distance between adjacent bins. Using this approach we were able to obtain a set of nominal values characterized by a very low variance that covered the radial range $r \in [0, 100]$ mm and the temporal range $t \in [0, 20]$ ns. Thanks to the constrictions a larger number of reference values were evaluated in those regions were the reflectance signal exhibits rapid variations rather than where it changes smoothly. An extrapolation approach has been used to add further points to obtain a more dense net of nominal values which can be robustly interpolated.

The reference surface $R_r(r_k, t_l)$ was obtained using the AD approach and it can be used to derive $R(r, t)$ and $R(r)$ for any value of the optical properties. The interpolation is performed using Non-Uniform-Rational-Bsplines (NURBS). For this work a specific fitting toolbox based on NURBS algorithms has been developed. To evaluate the steady state signal, $R(r)$, the reference signal needs to be integrated along the temporal dimension after applying the scaling equations.

To assert the accuracy of the reflectance signal evaluated through the implemented sMC model, we have compared its output with respect to a gold standard signal obtained through independent MC simulations computed for a wide range of optical properties.
For the time-resolved domain, the sMC output resulted very accurate. For $\mu_a < 0.01$ mm^{-1} the sMC output generally agrees within 3% of the gold standard values, even when the perturbation of the scattering coefficient with respect to the reference case was as large as 100%. Increasing the value of the absorption coefficient results in larger relative errors for late times, thus the physical range where the sMC model is accurate shrinks when μ_a grows. While these large values of the relative error, one must recognize that, in the late times range, the high absorption results in reflectance values that are to small to be practically measured.
The steady state results were accurate and generally within 3% of the gold standard values. For a value of the scattering coefficient much larger than the reference one, the accuracy of the sMC model is reduced for large source detector separations. Even increasing the absorption results in larger errors for the long source-detector separations because of the de-weighting that propagates the discretization error exponentially leading to larger inaccuracies for the SSR domain.

We used the sMC model for the solution of inverse problems in the temporal domain for source-detector (s-d) separations in the range [0.3, 20] mm. We studied and identified optimal parameters for the time resolution and for the fitting range. Moreover we tested the capabilities of the sMC solver in the presence of noise added to the simulated data. We showed that both the time resolution and the choice of the fitting range affect the accuracy of the recovered optical properties. The optimal parameters depend on the source-detector separation. For short radial distances it is necessary to use a finer time gating in order to capture the quick dynamic of the signal and to use a wider fitting range to gain sensitivity to the absorption coefficient. On the other side, when the source-detector separation becomes larger the results improve using larger time bins and the influence of the fitting

range is reduced.
The implemented forward solver proved to be accurate and fast in the recovery of both μ_a and μ_s' from time resolved signals for a range of optical properties ($\mu_a \in [0.001, 0.3]$ mm^{-1} and $\mu_s' \in [0.5, 2]$ mm^{-1}) and for source-detector separations ($r \leq 5$ mm) where the diffusion based models result in fairly large errors. The values recovered using the sMC model were in general within 1% of the true scattering coefficient and within 2% of the absorption coefficient. For the shortest source-detector separations the recovery of μ_a becomes challenging when it is very small. The average path of the photons collected at a short distance is very small and variations of the reflectance signal due to absorption variations are small. As a result the recovered μ_a is often inaccurate. It is interesting to note that the correlation between the two measured parameters is very low and the recovered scattering coefficient is always very accurate.
Even for situations that fall within the diffusive regime of photon migration ($r \geq 10$ mm) the accuracy of the developed forward solver is comparable with the performance of the standard diffusion approximation solvers for semi-infinite homogeneous media. The recovered OPs agree within 1% of the true values for most of the cases under investigation.
For the steady state domain we tested the quality of the inversion scheme changing the number of detectors used to measure the SSR curves and we tested the performance of the sMC solver in the presence of additional noise. The recovered values of μ_a and μ_s' are generally within 2% of the true values. The results are worse in the case of low absorption where the relative error becomes as large as 10%.

The implemented solver is able to represent the temporally-resolved reflectance signal with very high accuracy for a wide range of optical properties and over a wide physical domain. Thus it can be used as an inverse solver engine for the recovery of optical properties from experimental data as it works for the diffuse and for the non diffuse limit of photon migration, it is based on very fast and stable algorithms and the amount of data that needs to be stored is relatively small.
The results obtained from the forward analysis in the steady state domain showed that the model can represent within good accuracy the reflectance signal. The optical properties recovered from the solution of inverse problems are quite accurate. However for the steady state domain the large computing time may prevent the adoption of the model as a forward solver for *in-vivo* applications.

Appendix A: The Virtual Tissue Simulator

The Virtual Photonics Technology Initiative

The Virtual Photonics Technology Initiative was established by the Laser Microbeam and Medical Program (LAMMP), an NCRR National Biomedical Technology Center at the Beckman Laser Institute and Medical Clinic in April 2008.

The primary goals of this initiative are:

- Provide easy-to-use software tools with graphical-user interfaces to simulate the propagation and distribution of optical radiation in cells and tissues.
- Supply educational resources that provide the appropriate foundation for the proper usage of these computational tools.
- Stimulate the formation of an active community of experts and developers in Computational Biophotonics to advance this open-source effort.
- Develop improved computational models to simulate and design optical diagnostic, imaging, and therapeutic modalities.

The primary vehicle for the accomplishment of these goals is the ongoing development of the Virtual Tissue Simulator (VTS). The VTS is being designed as a modular and scalable platform to provide an integrated suite of computational tools to define, solve, visualize, and analyze relevant forward and inverse radiative transport problems in Biomedical Optics. This open source software is written in C# and the code is shared on CodePlex.
The design of the VTS is modular has multiple functionalities that may be used through command line and it has a graphical user interface that can be used to carry out multiple tasks

- problem definition
- analysis
- forward solver
- optimization

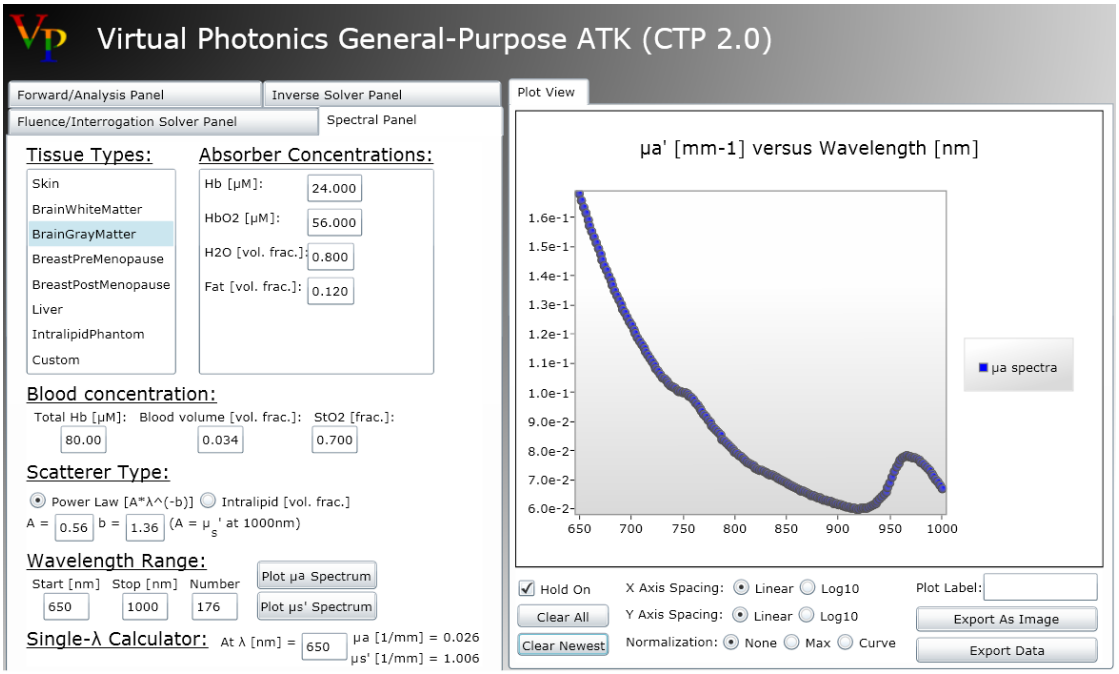

Figure 3.28: Graphical user interface for the evaluation of optical spectra for biological tissue.

The graphical interface facilitates input and output associated with each of these layers.

Problem Definition Layer

This module of the VTS allows the user to select the desired source and detector configurations, tissue geometry, and radiative transport properties.
A special feature of this layer is the ability to define the radiative transport properties of the tissue either conventionally in terms of the optical coefficients for absorption and scattering as well as, if appropriate, moments of the scattering phase function (g1,g2,..,gn) or in terms of tissue morphology and composition. This latter feature will queries the user about the tissue composition i.e., relative content of cells, extra cellular matrix, and vasculature as well as the concentration of important optical chromophores e.g., oxy- and deoxy-hemoglobin, water, melanin, fat, etc. From this user specification of tissue morphology and composition the VTS will automatically calculate the relevant optical properties at the desired wavelengths. Figure 3.28 show the GUI relative to the calculation of optical spectra.

Analysis Layer

The analysis module provides the opportunity to examine various aspects of the radiative transport solutions provided by the solver output. This layer provides three general classes of analysis related

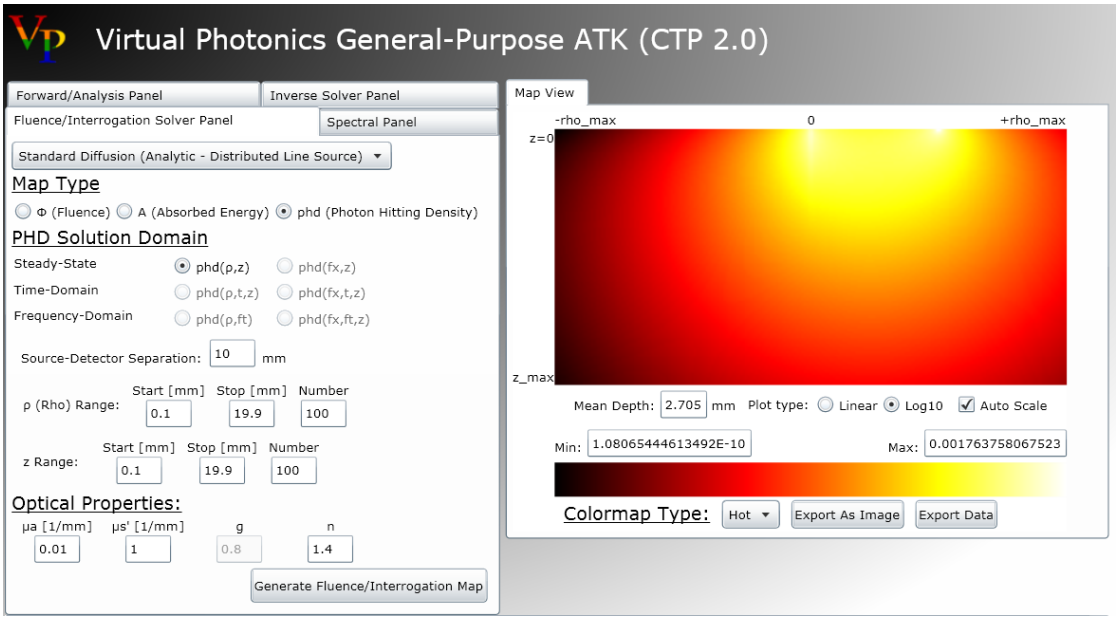

Figure 3.29: Graphical user interface for the generation of fluence/interrogation maps.

to

- perturbation
- sensitivity
- interrogation characteristics of the internal and/or remitted light field

Specifically the perturbation capabilities provide the ability to examine changes in the internal radiant field or remitted light due to perturbations in optical properties or size of internal structures. The sensitivity capabilities provide derivative information (elements of a Jacobian matrix) of the radiative transport solution that is used in gradient-based optimization algorithms. Finally, interrogation capabilities provide solutions to a 3-location transport problem that provides metrics for how specific source-detector configurations optically sample or 'interrogate' a desired target tissue volume of interest, as shown in Fig. 3.29

Solver Layer

This module of the VTS implements various radiative transport models or solvers that the user may use to solve his/her problem. Only a subset of the total available solvers may be active based on the specific source/detector configurations and/or tissue geometry/properties specified by the user. Solvers already developed by core investigators of the Virtual Photonics Technology Initiative are as follows

- Standard Diffusion Approximation (SDA/P1)

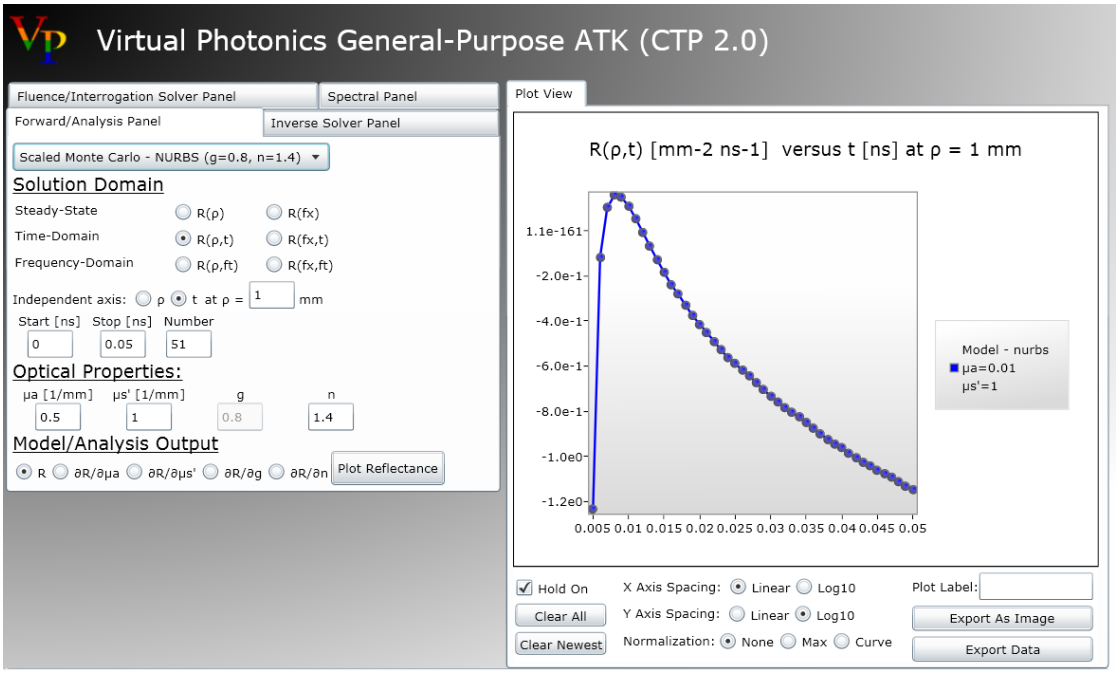

Figure 3.30: Graphical user interface for the visualization of reflectance signals.

- Internal dosimetry and reflectance/transmission
- Higher-Order 'Diffusion' Solvers (PN/δ-PN)
- Single Monte Carlo solver (sMC)
- Conventional Monte Carlo
- Perturbation Monte Carlo

The solvers implemented can be used to study the reflectance for any spectroscopy domain using the GUI shown in Fig.3.30.

Optimization Layer

This module of the VTS will provide capabilities for

- optical/physiological property recovery;
- image reconstruction; and
- design of optical measurements and instrumentation.

Based on the problem specified in the Problem Definition Layer the user will be able to supply either experimental data, or solver data combined with simulated experimental noise, to determine the ability of a given measurement configuration to provide the recover optical/physiological properties

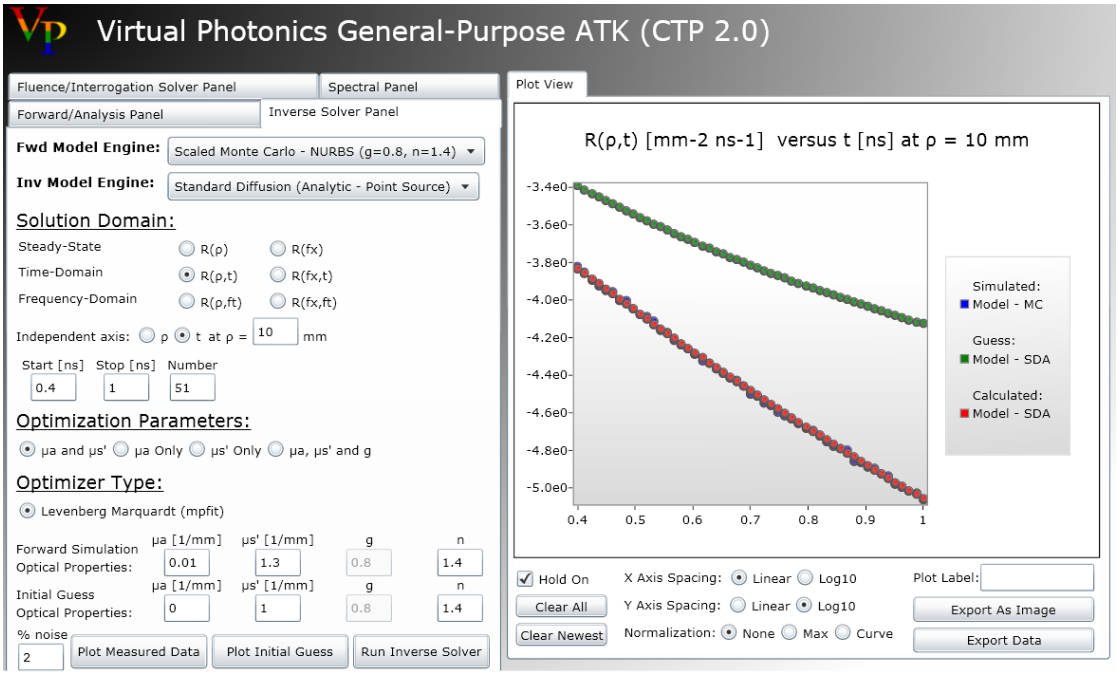

Figure 3.31: Graphical user interface for the resolution of inverse problems.

or render an optical image with sufficient fidelity. The GUI relative to the inverse problem resolution is shown in Fig. 3.31.

Appendix B: Non-Uniform-Rational-Bsplines

Introduction

Non Uniform Rational B-Splines,commonly referred as NURBS, are recognized as powerful tools for geometric design and for mathematic representation of 3-D geometries. The success behind NURBS is largely due to the fact that

- NURBS provide a mathematical representation of both analytic shapes as well as free-form entities;
- designing with NURBS is intuitive; almost every tool and algorithm has an easy-to-understand geometric interpretation;
- NURBS algorithms are fast and numerically stable;
- the amount of information required for a NURBS representation of a piece of geometry is much smaller than the amount of information required by other methods of approximations.

For this reasons NURBS have become the de-facto industry standard for curve and surface representation in computer graphics and have been widely used over the last fifty years.
The aim of the presented ToolBox is to approximate, fit or interpolate curves and surfaces with NURBS through easy-to-use algorithms and functions developed in MATLAB language.
Some of the function used rely upon the NURBS ToolBox by D.M. Spink, a collection of routines for the construction and manipulation of Non Uniform Rational B-Splines.
This ToolBox has been designed to reduce the storage size of datasets used in White Monte Carlo algorithms for determination of optical coefficients of 'semi-infinite' turbid media. With a little effort it is possible to find the control points and the knots vectors which give a very compact and accurate representation of the Reflectance for a homogeneous non-absorbing medium in different physical domains (e.g. $R(\rho, t)$ and $R(k_x, t)$) . Storing only the NURBS elements, i.e. the control points, the knot vector and the degree, the white Monte Carlo simulation can be generated at runtime. Applying the scaling method presented by *Kienle* et *al* [1] this single surface can be used to fit the data and to derive the absorption and reduced scattering coefficients.

Mathematical Preliminaries

Nonrational B-splines curve and surfaces are treated in details in References [2-3]. This section simply establishes the notation used in the following chapters and provides the reader an overview about NURBS to make him familiar with the concepts and with the functions applied in the ToolBox.

A p-th degree NURBS curve is defined by a knot vector U and by the expression

$$C(u) = \frac{\sum_{i=0}^{i=n} P_i w_i N_{i,p}(u)}{\sum_{i=0}^{i=n} w_i N_{i,p}(u)} \tag{3.8}$$

where $P_i = (x_i, y_i, z_i)$ are the $n+1$ 3D control points with an associated positive weight value w_i and $N_{i,p}$ are the p-th degree B-spline basis functions defined on the nonperiodic and nonuniform knot vector

$$U = \{\underbrace{0, \ldots, 0}_{p+1}, u_{p+1}, \ldots, u_{r-p-1}, \underbrace{1, \ldots, 1}_{p+1}\} \tag{3.9}$$

composed by $r+1$ elements, with $r = n+p+1$.

Analogously, a p-th by q-th degree NURBS surface is obtained by taking a bidirectional net of control points, two knot vectors U and V and the tensor-product expression

$$S(u,v) = \frac{\sum_{i=0}^{i=n} \sum_{j=0}^{i=m} P_{i,j} w_{i,j} N_{i,p} N_{i,q}(u)}{\sum_{i=0}^{i=n} w_i N_{i,p}(u)} \tag{3.10}$$

with

$$U = \{\underbrace{0, \ldots, 0}_{p+1}, u_{p+1}, \ldots, ur-p-1, \underbrace{1, \ldots, 1}_{p+1}\} \tag{3.11}$$

$$V = \{\underbrace{0, \ldots, 0}_{q+1}, u_{q+1}, \ldots, us-q-1, \underbrace{1, \ldots, 1}_{q+1}\} \tag{3.12}$$

U has r+1 knots, V has s+1, with $r = n+p+1$ and with $s = m+q+1$.

It is important to notice that NURBS are a parametric representation of a piece of geometry. So each of the coordinates of a point on a curve is represented separately as an explicit function of the independent parameter

$$C(u) = (x(u), y(u)) \qquad 0 \leq \mathrm{u} \leq 1 \tag{3.13}$$

As well for a surface

$$S(u,v) = (x(u,v), y(u,v), z(u,v)) \qquad 0 \leq u,s \leq 1 \tag{3.14}$$

It is straightforward to understand that a NURBS structure, whether a curve or a surface, is defined by three elements: degree, control points and knot vector. Once these are assigned it is possible to evaluate the basis functions and to build up the NURBS representation. All of these elements can

be modified to change the resulting NURBS. In the following chapter it is explained how this can be done. Since curves and surfaces behave in similar ways and share terminology we'll just refer to curves, but all these concepts apply identically to surfaces.

Degree

The degree p is a positive whole number, typically 1, 2, 3 or 5, but can be any positive whole number. NURBS lines and polylines are usually degree 1, NURBS circles are degree 2, and most free-form curves are degree 3 or 5. Sometimes the terms linear, quadratic, cubic, and quintic are used. The degree of a NURBS curve establishes the number of nearby control points that influence any given point on the curve. It is common to refer to the order of a NURBS curve, that is a positive whole number equal to p+1. It is possible to increase the degree of a NURBS curve and not change its shape, while it is not always possible to reduce the degree of a NURBS curve without affecting its shape. Generally increasing the degree makes a curve smoother, so for noisy datas it is possible to reduce the wiggling of the NURBS using a higher degree.

Control Points

The n+1 control points determine the shape of the resulting NURBS as each point of the curve is evaluated by taking a weighted sum of a number of control points. To obtain a curve of degree p at least p+1 control points are necessary. For a curve of p-th degre each control point has influence only on p+1 intervals (defined by the knot vector) of the parameter variable.The fact that a single control point only influences those intervals where it is active is a highly desirable property, known as *local support*. Moving and changing the number of control points is the easiest and most intuitive way to influence the shape of a curve.

Knot Vector

The knot vector is a list of n+p+2 nondecreasing numbers which split the parameter range into nonuniform knot spans. As previously mentioned the knots establish where each control point affects the shape of the curve. Each time the parameter value enters a new knot span, a new control point becomes active, while an old control point is discarded. The first and the last knots always have a multiplicity equal to the order of the curve, while each internal knot has a multiplicity m that goes from 1 (simple knot) to p (full knot). The multiplicity affects the differentiability of the curve which is infinitely continuously differentiable in the interior of a knot span and p-m times continuously differentiable at a knot. The positions of the knots influence the mapping of parameter space to curve space. Changing the knot vector strongly affects the shape of a NURBS curve. Suitable values for the knots are usually evaluated through some averaging or approximating methods which adapt the length of the spans lengths increasing the active control points in those regions where the curvature is higher.

Basis Functions

Once the degree, the control points and the knot vector are assigned it is possible to evaluate the B-splines. A p-th degree basis function used in NURBS, denoted as $N_{i,p}$ where i corresponds to the i-th control point, is recursively defined as

$$N_{i,0}(u) = \begin{cases} 1 & \text{if } u_i \leq u < u_{i+1} \\ 0 & \text{otherwise.} \end{cases} \tag{3.15}$$

$$N_{i,p}(u) = \frac{u - u_i}{u_{i+p} - u_i} N_{i,p-1}(u) + \frac{u_{i+p+1} - u}{u_{i+p+1} - u_{i+1}} N_{i+1,p-1}(u) \tag{3.16}$$

Thanks to the property of *local support* it is not necessary to evaluate all the basis functions to evaluate the NURBS in a specific value u because in each knot span there are only p+1 nonzero functions. This characteristic strongly decreases the computational effort necessary to represent a NURBS structure with a large number of control points.

Matlab Toolbox

This ToolBox has been developed to solve a reverse engineering problem: given a measured curve or surface, which can not be described analytically, it is possible to find a NURBS structure that represents it in an accurate and compact way. Starting from the digitalized points from the original curve the user can choose different ways to create a NURBS which fits the measured data. As suggested by *Piegl*[2] it is possible to distinguish two kinds of fitting, *interpolation* or *approximation*. In interpolation the constructed curve or surface satisfies the given data precisely, i.e. the NURBS passes exactly through a set of points specified by the user. With this method it is generally possible to have a very compact and flexible representation of the curve or surface, but it is necessary to be able to sample the "right" points to be fit. This may be difficult when dealing with measured Reflectance as the noise might become quite large. In approximation the constructed curve or surface does not necessarily satisfy the given data precisely, but only approximately in a least square mean. This is generally a better approach when we want to represent a large number of points which can contain measurement or computational noise. In this case it is important for the curve or surface to capture the "shape" of the data, but not to wiggle its way through every point.

The functions of the ToolBox are gathered into folders according to their main aim. *BSPLINES* and *NRB* contain all the functions from D.M. Spink 's NURBS ToolBox . The first one is made by a set of routines used to build up the basis functions, while the second one contains functions used to construct NURBS curves or surfaces. The folder *NURBS Math* is comprised by a set of algorithm used to compute reasonable values for the parameter variable and for the knot vectors, by functions used to solve fitting problems in a matrix form, by methods that solve geometrical problems and by testing routines. The next chapters briefly describes the 'user functions' of the ToolBox which are collected into three different folders: *Interpolation*, *Approximation* and *Fitting*. Each of them has a subfolder with specific methods that the user should't directly call. Both *Approximation* and

Fitting perform a least square approximation for curves and surfaces. The distinction between them is based on the way the minimization problem is solved, the adopted naming conventton follows the "*The NURBS Book*" [2]. The functions in *Split&Link* have two main aims: split a curve or a surface into sections that can be singularly fitted and then link the multiple NURBS to give one single structure. This procedure can highly improve the quality of the approximation reducing the storage size for different reasons:

- splitting the curve or surface into sections where the trend does not show large deviations it is possible to capture the shape with a smaller number of control points;
- separating zones with a different noise level, it is possible to adapt the number of control points to this feature: using a larger number of control points where the data is more consistent and fewer control points when the oscillations are due to noise.

The *Knot Remove* routines are a MATLAB adaptation to the algorithm presented by *Tiller*[4], for both curves and surfaces. Knot removal is an important utility as it may be invoked to obtain the most compact representation of a piece of geometry. A knot is considered removable only if it leaves the NURBS unchanged within a meaningful tolerance, the removal of a knot involves the elimination of a control point, hence a reduction in the storage size. The methods which perform this process are *CrvRemoveKnots* for curves and *SrfRemoveKnots* for surfaces. This is very efficient when the resulting curve or surface is given by different NURBS linked to each other. To link them it is necessary to use internal knots with full multiplicity, which may often be removed. The *Visualization* functions are used to have a graphical way to see the accuracy of the fitting NURBS.

The following chapters give a brief description of how the interpolating, approximating and fitting algorithms work. Each function of the ToolBox is completely explained with comments in the MATLAB code.

NURBS curve

Interpolation

CrvInterp: this function performs a global curve interpolation to certain point data Q_k with a p-th degree NURBS. After having assigned a parameter value, $\bar{u}_k$ to each Q_k and select an appropriate knot vector U, it is possible to set up the $(n+1)$x$(n+1)$ system of linear equations

$$Q_k = C(\bar{u}_k) = \sum_{i=0}^{i=n} N_{i,p}(\bar{u}_k) P_i \tag{3.17}$$

The control points P_i are the n+1 unknowns, so for each interpolated point there will be one control point. The shape and parametrization of the resulting curve will be affected by the parameter values and by the knot vector. The problem to be solved is to find appropriate values for the $\bar{u}_k$ and for U. In the literature many options exist for obtaining these values, here the *chord length* approximation has been implemented to set proper values for the parameter,while an averaging technique is used to find knot values which reflect the distribution of the $\bar{u}_k$. Figure 1 shows a measured curve $R(t)$ at a spatial frequency of 0.2mm^{-1}. It is possible to reproduce quite precisely the shape of the data as long as the sampled points are not distorted by noise.

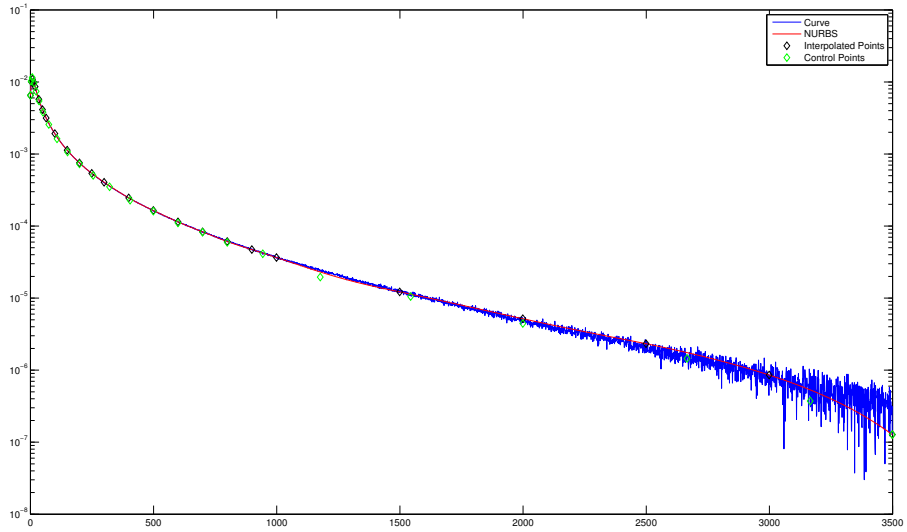

Figure 3.32: A NURBS curve interpolating twenty five points

Approximation

CrvApprox: This function returns a p-th degree NURBS with n+1 control points that approximates the measured data points in a least square sense. To allow additional control over the accuracy of the approximation to each data item, the function can receive as input a weight vector that represents for each point the "tightness" of the approximation to that point. Notice that this weighting has nothing to do with the weight intended in the NURBS sense.
If we need to approximate within a specific precision a error bound E can be input along with the data to be fit. As it is usually not known in advance how many control points are necessary to obtain a required accuracy, the *CrvApprox* methods is iterative if the error is input. It is possible to choose if the accuracy has to be reached in each individual point or just in an arithmetic mean sense. At each iteration the deviation between the data and the NURBS is measured, if it is accetable the function returns, else the number of control points is incremented. If the initial number of control points is too small to reach the required precision an error is thrown to avoid an extended processing time. It is possible to start with a higher number of control points or to reduce the accuracy. A better solution may be to try to split the curve into sub-sections, approximate them singularly and then join all of them in one global NURBS. This procedure is realized by the *MultiCrvApprox* method. The user has to define the positions where the curve will be split and then linked. The boundary points of each curve are precisely interpolated. If they are corrupted by noise strange shapes might occur in the resulting NURBS. It is possible to use the same initial number of control points for each section or to specify n for the different sub-curves. To be able to link the NURBS they all must be compatible ,i.e. of common degree and with the end parameter value of the i-th curve equal to the start parameter of the $(i+1)$-th curve. For each iteration the function which computes the mathematics needed to solve the lest square problem is *CrvLeastSquareApproximation*.

This function finds the n+1 control points for a p-th degree NURBS that best approximates the data in a least square sense. Setting all the weights to 1 and precomputing values for the parameter and for the knots it is possible to set up and solve the unique linear least square problem for the unknown control points. Starting from $Q_j (j = 1, \ldots, m)$ data points $(m > n \geq p)$ we seek

$$C(u) = \sum_{i=0}^{i=n} N_{i,p}(u) P_i \qquad u \in [0, 1] \tag{3.18}$$

satisfying that:

- $Q_0 = C(0)$ and $Q_m = C(1)$;
- the remaining Q_j are approximated in a least square sense, i.e.

$$\sum_{j=1}^{m-1} |Q_k - C(\bar{u}_k)|^2] \tag{3.19}$$

  is a minimum with respect to the n+1 variables, P_i.

Once again the parameter values are evaluated through the *chord length* approximation, while to define the internal knots a different approximation method suggested by De Boor [5] is implemented. This Method guarantees that every knot span contains at lest one $\bar{u}_k$.
In a distance sense, the approximation improves as the number of control points is increased, however if the number of control points approaches the number of measured points, undesirable shapes can occur if the data exhibits noise or unwanted wiggles.
Figure 2 shows a measured curve $R(t)$ at a spatial frequency of 0.2mm^{-1} approximated by a single NURBS with fifty control points and by four linked NURBS with the same amount of control points.

Fit

CrvFit: all the concepts explained for approximation apply in the same way when this function is used. Along with the weights and the maximum deviation an additional variable can be input, i.e. the index of a set of data points which will be exactly interpolated. The core function that solves the fit problem for a single iteration of a curve is *CrvLeastSquareFitting*.
With this function it is possible to interpolate some constrained (m_c) points and approximate the rest (m_u) in a weighted least square sense. It is a NURBS adaption of an algorithm by *Smith* et *al* [2-6]. To find the approximating NURBS it solves a constrained minimization problem. The implemented method uses Lagrange multipliers to find the unique solution, for a detailed description see reference [7]. To find a p-th degree NURBS with n+1 control points this algorithm requires that

$$m_c < n \quad m_c + n < m_u + 1 \tag{3.20}$$

The parameter values and the internal knots are computed using the same approaches of the previous method. This approach is efficient when the curve has a smooth trend, but when there are sharp

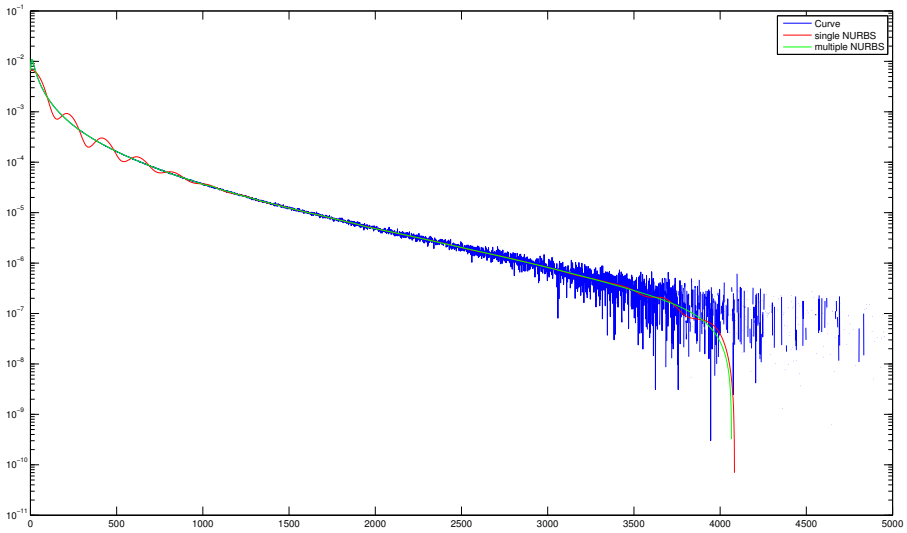

Figure 3.33: Multiple and single NURBS approximating the same curve with fifty control points

turns the constrained conditions might involve unexpected oscillations in the resulting NURBS if the number of control points is too small to capture the shape of the curve.

To apply the fit method on various sections resulting from the split of a curve the *MultiCrvFit* function must be used. Once again the user has to define the division and junction points. It is possible to decide if for each section the boundary points will be constrained. When a high accuracy is required it is better to leave all the points unconstrained. The continuity is later obtained averaging the linking points of the following NURBS.

NURBS surface

Interpolation

SrfInterp: given a set of $(n+1)$x$(m+1)$ data points $\{Q_{k,l}\}$, $k = 0, \ldots, n$ and $l = 0, \ldots, m$, sampled from a surface, this functions constructs a (p,q)-th degree NURBS surface interpolating these points, i.e.

$$Q_{k,l} = S(\bar{u}_k, \bar{v}_l) = \sum_{i=0}^{i=n} \sum_{j=0}^{j=m} N_{i,p}(\bar{u}_k) N_{j,q}(\bar{v}_l) P_{i,j} \tag{3.21}$$

Once again the first problem to be solved is to compute reasonable values for the $(\bar{u}_k, \bar{v}_l)$ and for the knot vectors U and V. The implemented method uses the *chord length* approximation to compute parameters $\bar{u}_0^l, \ldots, \bar{u}_k^l$ for each l, then by averaging across all $\bar{u}_k^l$, $l = 0, \ldots, m$ it obtains each $\bar{u}_k$.

The same process is applied along the other parametric dimension.
In both directions the knot vector is evaluated through an averaging technique. Since $S(u,v)$ is a tensor product surface, instead of solving a $(n+1)$x$(m+1)$ system of linear equations, it is possible to obtain the control points as a sequence of curve interpolations. For fixed l equation (3.21) might be written as

$$Q_{k,l} = \sum_{i=0}^{i=n} N_{i,p}(\bar{u}_k)\Big(\sum_{j=0}^{j=n} N_{j,q}(\bar{v}_l)P_{i,j}\Big) = \sum_{i=0}^{i=n} N_{i,p}(\bar{u}_k)R_{i,l} \tag{3.22}$$

where

$$R_{i,l} = \sum_{j=0}^{j=n} N_{j,q}(\bar{v}_l)P_{i,j} \tag{3.23}$$

Equation (3.22) is just a curve interpolation through the points $Q_{k,l}$, $k = 0, \ldots, n$. The $R_{i,l}$ are the control points of the isoparametric curve on $S(u, v)$ at fixed $v = \bar{v}_l$. Now fixing i and letting l vary it is possible to make a curve interpolation through $R_{i,0}, \ldots, R_{i,m}$ to obtain the $P_{i,j}$ control points which define the interpolating NURBS surface.

Approximation

SrfApprox: in approximation the constructed NURBS surface does not satisfy the measured data precisely, but only approximately. Let $\{Q_{k,l}\}$, $k = 0, \ldots, r$ and $l = 0, \ldots, s$, be the $(r+1)$x$(s+1)$ set of points to be approximated with a (p, q)-th degree surface with $(n+1)$x$(m+1)$ control points. Although it is possible to set up a least squares fit problem the implemented functions builds the NURBS surface upon the curve approximation previously presented. The scheme is the same of the one used for interpolation: after approximating all the curves in one direction the resulting control points are approximated across the other direction.
As with curves the surface approximating function can receive as an input an error bound variable along with the initial number of control points. As long ad the required accuracy is not reched the number of control points is increased. It is possible to fix the number of control points in one direction and increase it only along the other one.
The iteration is carried out using *SrfLeastSquareApprox* which is the core function used to evaluate the approximating surface implementing the curve approximation methods along both directions through *CrvLeastSquareApproximation*.
If the surface exhibits sharp variations it might be necessary to use an elevated number of control points to capture its shape. Once again the problem may be solved splitting the surface into patches which can be more easily approximated within the required accuracy. This process is carried on by the *MultiSrfApprox*.

Fitting

SrfFit: as for curves all the concepts presented within the *SrfApprox* method apply identically when the fitting approach is used. Each iteration that returns a fitting NURBS is carried out by *SrfLeastSquareFit*. This routine is based on the curve fitting method. For surfaces the possibility of setting some constrained points has not be implemented because a better accuracy is achieved if no constrictions are imposed. When different fitting NURBS are linked using *MultiSrfFit* the boundary control points are averaged to improve the continuity of the curve.

Bibliography

[1] Alwin Kienle and Michael S. Patterson. Determination of the optical properties of turbid media from a single Monte Carlo simulation. *Phys. Med. Biol.*, 41(10):2221–2227, 1996.

[2] Richard C. Haskell, Lars O. Svaasand, Tsong-Tseh Tsay, Ti-Chen Feng, Matthew S. McAdams, and Bruce J. Tromberg. Boundary conditions for the diffusion equation in radiative transfer. *Journal of the Optical Society of America A*, 11(10):2727–41, 1994.

[3] Alwin Kienle and Michael S. Patterson. Determination of the optical properties of semi-infinite turbid media from frequency-domain reflectance close to the source. *Physics in Medicine and Biology*, 42(9):1801–19, September 1997.

[4] Alwin Kienle and Michael S. Patterson. Improved solutions of the steady-state and the time-resolved diffusion equations for reflectance from a semi-infinite turbid medium. *Journal of the Optical Society of America A*, 14(1):246–254, 1997.

[5] Andreas H. Hielscher. The influence of boundary conditions on the accuracy of diffusion theory in time-resolved reflectance spectroscopy of biological tissues. *Physics in Medicine and Biology*, 40(11):1957–75, 1995.

[6] B.C. Wilson and G. Adam. A Monte Carlo model for the absorption and distributions of light in tissue. *Med. Phys*, pages 824–830, 1983.

[7] Alwin Kienle, Lothar Lilge, Michael S. Patterson, Raimund Hibst, Rudolf Steiner, and Brian C. Wilson. Spatially resolved absolute diffuse reflectance measurements for noninvasive determination of the optical scattering and absorption coefficients of biological tissue. *Applied Optics*, 35(13):2304, May 1996.

[8] T J Farrell, M S Patterson, and B.C. Wilson. A diffusion theory model of spatially resolved, steady-state diffuse reflectance for the non invasive determination of tissue optical properties in vivo. *Med. Phys.*, 19(4):879–888, 1992.

[9] R M P Doornbos, R Lang, M C Aalders, F W Cross, and H J C M SterenBorg. The determination of in vivo human tissue optical properties and absolute chromophore concentrations using spatially resolved steady-state diffuse reflectance spectroscopy. *Phys. Med. Biol.*, 44(44):967–881, 1999.

[10] R Cubeddu, M Musolino, A Pifferi, P Taroni, and G Valentini. Time-Resolved Reflectance : A Systematic Study for Application to the Optical Characterization of Tissues. *IEEE Journal of Quantum Electronics*, 30(10):2421–2430, 1994.

[11] J Tualle. Real time optical coefficients evaluation from time and space resolved reflectance measurements in biological tissues. *Optics Communications*, 124(3-4):216–221, March 1996.

[12] Steven L. Jacques and L. Wang. Monte Carlo modeling of light transport in multi-layered tissue. *Computer Methods and Programs in Biomedicine*, 47:131 146, 1995.

[13] Makoto Matsumoto and Takuji Nishimura. Mersenne twister: a 623-dimensionally equidistributed uniform pseudo-random number generator. *ACM Transactions on Modeling and Computer Simulation*, 8(1):3–30, January 1998.

[14] L.G. Henyey and J.L. Greenstein. Diffuse Radiation of the Galaxy. *Astrophysics Journal*, 93:70–83, 1941.

[15] Paula A. Whitlock Malvin H. Kalos. *Monte Carlo Methods Volume 1: Basics.* "Wiley-Interscience", 1995.

[16] R. Graaff, M. H. Koelink, F. F. M. De. Mul, W. G. Zijistra, A. C. M. Dassel, and J. G. Aarnoudse. Condensed Monte Carlo simulations for the description of light transport. *Applied Optics*, 32,(4):426–34, 1993.

[17] A. Pifferi, P. Taroni, G. Valentini, and S. Andersson-Engels. Real-time method for fitting time-resolved reflectance and transmittance measurements with a monte carlo model. *Applied Optics*, 37(13):2774–80, May 1998.

[18] Erik Alerstam, Stefan Andersson-Engels, and Tomas Svensson. White Monte Carlo for time-resolved photon migration. *Journal of Biomedical Optics*, 13(4):041304, 2008.

[19] C K. Hayakawa, J. Spanier, F. Bevilacqua, A. K. Dunn, J. S. You, B. J. Tromberg, and V. Venugopalan. Perturbation Monte Carlo methods to solve inverse photon migration problems in heterogeneous tissues. *Optical Letters*, 26:1335–1337, 2001.

[20] InSeok Seo, Joon S. You, Carole K. Hayakawa, and Vasan Venugopalan. Perturbation and differential Monte Carlo methods for measurement of optical properties in a layered epithelial tissue model. *Journal of Biomedical Optics*, 12(February):1–15, 2007.

[21] Alwin Kienle, Michael S. Patterson, Nora Dögnitz, Roland Bays, Georges Wagniνres, and Hubert van Den Bergh. Noninvasive Determination of the Optical Properties of Two-Layered Turbid Media. *Applied Optics*, 37(4):779–791, February 1998.

[22] Heping Xu, Thomas J. Farrell, and Michael S. Patterson. Investigation of light propagation models to determine the optical properties of tissue from interstitial frequency domain fluence measurements. *Journal of Biomedical Optics*, 11(August):1–18, 2006.

[23] David J. Cuccia, Frederic Bevilacqua, Anthony J. Durkin, Frederick R. Ayers, and Bruce J. Tromberg. Quantitation and mapping of tissue optical properties using modulated imaging. *Journal of Biomedical Optics*, 14(2):024012, 2009.

[24] Gregory M. Palmer and Nirmala Ramanujam. Monte Carlo-based inverse model for calculating tissue optical properties. Part I: Theory and validation on synthetic phantoms. *Applied optics*, 45(5):1062–71, February 2006.

[25] R. Aronson. Radiative transfer implies a modified reciprocity relation. *Journal of the Optical Society of America. A*, 14(2):486–90, February 1997.

[26] Spanier Jerome and M.Gelbard Ely. *Monte Carlo Principles and Neutron Transport Problems.* "Dover", 2008.

[27] W. Cheong and S.A. Prahl. A review of the optical properties of biological tissues. *IEEE J. Quantum Electron*, 26:2166–85, 1990.

[28] Simon Arridge and Martin Schweiger. A gradient-based optimisation scheme for optical tomography. *Optics Express*, 2(6):213, March 1998.

[29] W.Hines William, C.Montgomery Douglas, M.Goldsman David, and M.Borror Connie. *Probability and Statistics in Engineering.* "John Wiley & Sons Inc", 2003.

[30] J. Dougherty, R. Kohavi, and S. Mehran. Supervised and Unsupervised Discretization of Continuous Features. In *Proceedings 12th International Conference on Machine Learning*, pages 194–202. Morgan and Kaufmann, 1995.

[31] M. Boulle. Optimal Bin Number for Equal Frequency Discretizations in Supervized Learning. *Intelligent Data Analysis*, 9(2):175 – 188, 2005.

[32] Tiller Wayne and Piegl Les. *The NURBS Book*. "Springer", 1995.

[33] F.Rogers David. *An Introduction to NURBS: With Historical Perspective.* "Morgan Kaufmann; 1st edition", 2004.

[34] Troy O McBride, Brian W Pogue, Steven Poplack, Sandra Soho, Wendy a Wells, Shudong Jiang, Ulf L Osterberg, and Keith D Paulsen. Multispectral near-infrared tomography: a case study in compensating for water and lipid content in hemoglobin imaging of the breast. *Journal of biomedical optics*, 7(1):72–9, January 2002.

[35] R Graaff, M H Koelink, F F M De Mul, W G Zijistra, A C M Dassel, and J G Aarnoudse. Condensed MC. *Applied Optics*, 1993.

[36] Qianqian Fang and David A Boas. Monte Carlo simulation of photon migration in 3D turbid media accelerated by graphics processing units. *Optics express*, 17(22):20178–90, October 2009.

[37] Erik Alerstam, Tomas Svensson, and Stefan Andersson-Engels. Parallel computing with graphics processing units for high-speed Monte Carlo simulation of photon migration. *Journal of Biomedical Optics*, 13(6):060504, 2008.

[38] William H. Louisell. *Quantum Statistical Properties of Radiation .pdf*. Wiley-Interscience, 1990.

[39] Craig B Markwardt. Non-linear Least Squares Fitting in IDL with MPFIT. *Analysis*, 411:1–4, 2008.

[40] B&H. Single Photon The Becker & Hickl PC Based.

[41] PicoHarp. PicoHarp 300 Time Correlated Single Photon Counting system.

[42] R Cubeddu, A Pifferi, P Taroni, A TOrricelli, and G Valentini. Experimental test of theoretical models for time-resolved reflectance. *Med. Phys.*, 23(9):1625–1633, 1996.